

Proceedings of the 10th Meeting of Japan CF Research Society

Edited by Ken-ichi Tsuchiya

March 5-6, 2010

Hachioji-Tokyu-Building, Japan

Copyright © 2010 by Japan CF Research Society

All rights reserved. No part of this publication may be reproduced, stored in a retrieval system, or transmitted, in any form or by any means, electronic, mechanical, photocopying, recording or otherwise, without the prior permission of the copyright owner.

PREFACE

This is the Proceedings of the 10th Meeting of Japan CF-Research Society (JCF10), which was held at Hachioji-Tokyu-Building on March 5-6, 2010. In this meeting, 15 oral presentations were given and 15 papers were submitted to the editorial board. They were peer reviewed by the referees, and revised for the publication as the proceedings. As a result, 8 papers concerning the experiment and 7 papers concerning the theory were accepted. Editing them, we have successfully completed our work. Now, the abstracts of all the presentations are available at our web-site <http://jcfrs.org>. The electronic version of the proceedings is also available in the same web-site. Needless to say, any responses from the world scientists will be welcomed.

By the way, the history of JCF has started in 1999 at Osaka Univ. Therefore, this is the 10th anniversary meeting which is going through the new phase. From JCF1 to JCF9, Prof. Hiroshi Yamada of Iwate Univ. has devotedly worked as a chairperson of the JCF editorial board. After he had completed his term, this position was taken over by me, and this is the first experience for me to edit the proceedings. I think our daily steps in the CF research may be small, but I believe they will give a break-through for the fundamental understanding of the nature.

Finally, we would like to thank all the participants, and also the persons who have collaborated in organizing this meeting. In particular, we would like to express our heartfelt appreciation to the financial support by The Thermal & Electric Energy Technology Foundation.

Chairperson of JCF Editorial Board
Ken-ichi Tsuchiya (Tokyo National College of Technology)
September 2010

CONTENTS

Preface

K. Tsuchiya i

EXPERIMENTS

Hydrogen/Deuterium Absorption Capacity of Pd Nanomaterials and its Relation with Heat Generated upon Loading of Hydrogen Isotope Gases

T. Hioki, H. Azuma, T. Nishi, A. Itoh, S. Hibi, T. Motohiro and J. Kasagi..... 1

D + D Fusion Acceleration in High Temperature Acoustic Cavitations

Y. Toriyabe and J. Kasagi 9

Measurements of Heat and Radiation from Pd Nano-Powders during Absorption of Hydrogen Isotopes

*Y. Sasaki, Y. Miyoshi, A. Taniike, A. Kitamura,
A. Takahashi, R. Seto and Y. Fujita* 14

Absorption/Adsorption Processes of Hydrogen Isotopes Observed for Pd Nano-Powders

*Y. Miyoshi, Y. Sasaki, A. Taniike, A. Kitamura,
A. Takahashi, R. Seto and Y. Fujita* 20

Charged Particle Detection during Gas Loading/Permeation Experiment with $\Delta E - E$ Si Counter Telescope

Y. Toriyabe and J. Kasagi 26

Search for Nuclear Events in Deuterium Discharge Experiment Using Multi-layered Metal Cathode

H. Sasaki, T. Murakami, H. Ougida, S. Narita and H. Yamada 31

Anomalous Tracks Recorded on CR39 in Deuterium Desorption Experiment

*S. Narita, H. Yamada, H. Nagai, T. Takahashi, A. Taguchi, M. Sasaki,
M. Kawashima and R. Moriya* 36

Detection of Energetic Charged Particle from Thin Ni Cathode in Shortened $\text{Li}_2\text{SO}_4/\text{H}_2\text{O}$ Electrolysis Using Track Detector CR-39

H. Yamada, S. Narita, Y. Oshima, H. Yamagishi, H. Yokokawa and H. Nanao ---- 41

THEORIES

Role of PdO Surface-Coating of Pd Nano-Particle for D(H) Charging and Cluster Fusion <i>A. Takahashi, A. Kitamura, Y. Sasaki, Y. Miyoshi,</i> <i>A. Taniike, R. Seto and Y. Fujita</i> -----	46
A Power Spectrum Change by Irregular Periodicity of Superlattice at Tunnel Resonance of CF <i>M. Ban and H. Numata</i> -----	54
A Theoretical Study on the Possible Change of the Phonon Dispersion Relation due to the Nuclear Reaction in Solid II <i>K. Tsuchiya and S. Fujita</i> -----	59
Simulation of Palladium Transmutation Products Using a Nuclear Lattice Model <i>N. D. Cook</i> -----	64
Cellular Automata Numerical Simulation of Cascade Vortices <i>H. Numata and M. Ban</i> -----	68
Abraham-Lorentz-Dirac Equation in Quantum Mechanics: The Beginning of Weakened Coulomb Potential <i>S. Sasabe and M. Ozaki</i> -----	74
Computer Simulation of States of Hydrogen in Metals of Face Centered Cubic Lattice <i>H. Miura</i> -----	77

Hydrogen/deuterium absorption capacity of Pd nanomaterials and its relation with heat generated upon loading of hydrogen isotope gases

¹Tatsumi HIOKI[†], ¹Hirozumi AZUMA, ¹Tepei NISHI, ¹Akio ITOH, ¹Shogo HIBI,
¹Tomoyoshi MOTOHIRO, and ²Jirohta KASAGI

¹Toyota Central Research and Development Laboratories, Inc., Nagakute, Aichi, Japan

²Research Center for Electron Photon Science, Tohoku University, Mikamine, Sendai, Japan

[†]E-mail:hioki@mosk.tytlabs.co.jp

Abstract: Using Sievert's method, hydrogen/deuterium absorption capacity was measured for Pd nanopowder and nanocomposites of nanoPd/ γ Al₂O₃ and nanoPd/ZrO₂. For these materials, heat evolution upon loading of hydrogen isotope gases was also measured by a flow calorimeter. In order to identify the properties of metallic Pd nanoparticles, both measurements were conducted repeatedly three or four times without exposing the samples to air. It was found that both apparent absorption capacity and heat evolution depended strongly on the degree of oxidation of Pd. The amount of the oxidized Pd in each sample was estimated from the difference between the apparent and the true values of hydrogen/deuterium absorption capacity and used to evaluate the heat generated from chemical reactions. The hydrogen absorption capacity at 1MPa was found to be slightly smaller than that of Pd bulk for all the Pd nanomaterials studied. The heat evolution was composed of two stages, i.e., the first stage during pressurizing the samples from 0 to 1MPa and the second stage where the sample was kept under a fixed pressure of 1MPa. The heat generated in the first stage was largely explained by taking into account two chemical reactions, i.e., the water formation reaction and the hydride/deuteride formation reaction. It was noted that in the second stage, where the heat generated from chemical reactions was hardly expected to occur, a small heat power was observed intermittently when the samples were loaded with deuterium gas.

Keywords: condensed matter nuclear reaction, Pd nanoparticles, hydrogen isotope gases, absorption capacity, heat evolution, gas loading

1. Introduction

Arata and Zhang have recently reported that by simply loading nanocomposites of Pd/ZrO₂ or Pd/Ni/ZrO₂ with deuterium gas, they have observed a heat generated from a deutron-deutron (D-D) nuclear fusion reaction [1]. The D-D nuclear fusion reaction has been suggested from the observation of a remarkable increase of ⁴He in the gas sampled from the powder sample after the loading experiments [1]. It has been expected that nano-sized Pd particles absorb enough deuterium atoms to induce the nuclear fusion

reaction. Actually, for the nanoPd/ZrO₂ system, a very high value of hydrogen absorption capacity has been reported [2].

Kitamura et al. have constructed a twin type flow calorimeter to evaluate qualitatively the heat generated by loading of Pd/ZrO₂ nanocomposite with hydrogen isotope gases, and have observed anomalously large energies of hydrogen isotope gas absorption as well as large D/Pd and H/Pd ratios of about 1.1 [3]. They have also observed a significant difference in the heat power between deuterium and hydrogen after the finish of deuteride or hydride formation reaction at the early

stage of the gas loading.

In this study, the relationships between the size of Pd particles, the absorption capacity of hydrogen (/deuterium), and the heat generation upon loading of hydrogen isotope gases were investigated for nanomaterials of Pd ; nanopowder of Pd [4] and nanocomposites of Pd/ γ -Al₂O₃ [4] and Pd/ZrO₂ [5]. The hydrogen/deuterium absorption capacity was measured with the Sievert's method [6]. The heat power generated upon pressurizing the materials with hydrogen isotope gases was measured with a flow calorimeter. In order to examine the influence of oxidized Pd on absorption capacity and heat evolution, both of these properties were measured three to four times repeatedly, without exposing the samples to air. Prior to each measurement, the samples were heat treated in vacuum in order to remove the absorbed molecules or to eliminate completely the hydrogen or deuterium absorbed in the preceding measurement.

2. Experimental

2.1. Materials

The materials used in this study were: Pd nanopowder (TMAY4030) obtained from Tanaka Kikinzo Kogyo with average Pd particle size 10 ~ 20nm; Pd- γ -Al₂O₃ composites with Pd concentrations of 13 and 20wt% with average Pd particle size 2~5nm; 30wt%Pd/ZrO₂ composites obtained from Santoku Corporation with average Pd particle size ~10nm. Foils of Pd 0.1mm thick with purity 99.95% were used as a reference sample of Pd bulk.

2.2. Hydrogen storage capacity

A pressure-composition (PC) isotherm apparatus (Suzuki Shokan Co. Ltd) was used to measure hydrogen absorption capacity as a function of pressure up to about 1MPa at room temperature (300K). The purity of hydrogen and deuterium was 99.9999% and 99.995%, respectively.

2.3. Calorimetry

The heat evolution associated with loading of

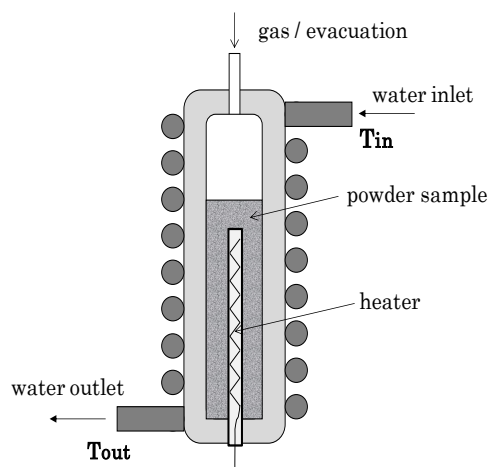


Figure 1. Schematics of the calorimeter [4].

hydrogen isotope gases was measured with a flow calorimeter [4]. Figure 1 shows the schematics. The difference in the temperature between the inlet (T_{in}) and outlet (T_{out}) of the cooling water was measured with thermocouples of alumel-chromel. The flow rate of water was measured using a Coriolis-force type flow meter. The temperature difference, $T_{out} - T_{in}$, and the flow rate of water were registered every 30 seconds and used to calculate the heat power. An electric heater was mounted at the center of the sample vessel and used to determine the recovery rate of heat, i.e. the ratio of the calculated heat power with the measured temperature difference and the flow rate of water to the heat power supplied by the electric heater. A value of 0.55 was used as the recovery rate [4], which was almost independent on the species of the used gas (H₂, D₂, He), the gas pressure in the range 0 ~1 MPa, and the electric heater power in the range of 1~5W. In order to suppress the fluctuation and the drift of the measured output power, the calorimeter system was thermally insulated from the ambient atmosphere using a thermal insulation material. The accuracy of the calorimeter was ± 50 mW. The gases were supplied into the sample vessel through a needle valve and a mass

flow controller. The flow rate of gas was about 20ml/min.

3. Results and discussion

3.1. Hydrogen absorption capacity

As a reference for Pd bulk, PC isotherms were measured for a Pd foil sample of about 3g. The measurements were made three times repeatedly. Prior to each measurement, the sample was heat treated in vacuum for more than 2 hours at 523K and was subjected to the PC isotherm measurement without exposing the sample to the air. The results are shown in Figure 2.

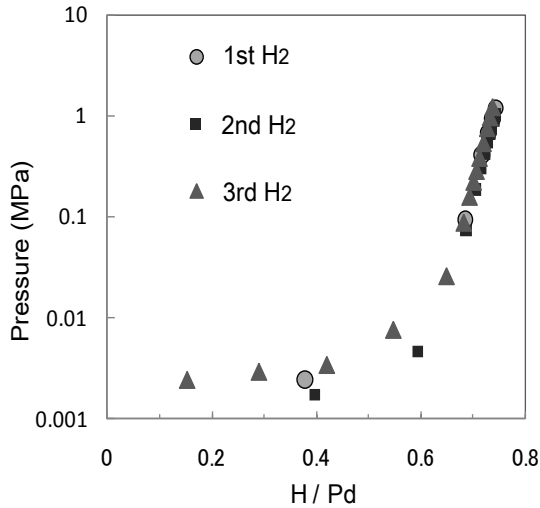


Figure 2. PC isotherms for the foil sample of Pd. The measurements were made 3 times repeatedly at 300K.

It is seen that the curves of the three times measurements are almost identical. The absorption capacity, H/Pd, at 1MPa is 0.74, which agrees well with the value for Pd bulk reported in the literature [7].

In Figure 3, the PC isotherms are shown for the nanocomposite sample of 20wt%Pd/ γ Al₂O₃. The measurements were made 3 times repeatedly with H₂. In this figure, it is remarkable that the H/Pd value at 1MPa for the measurement of the first time, i.e. 2.4,

is much larger than the values for the measurements of the second (0.68) or the third (0.70) times. This difference between the first and second measurements is definitely attributed to oxidized Pd, i.e. PdO, which is often contained in nano-sized Pd materials [4].

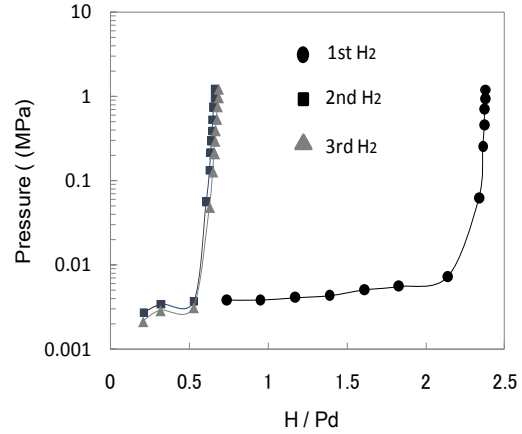
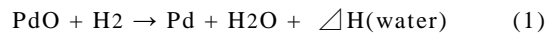


Figure 3. PC isotherms for 20wt%Pd- γ Al₂O₃. The measurements were made 3 times repeatedly at 300K.

If the Pd particles are initially oxidized and reduce to metallic Pd during the first time measurement, then both of the following chemical reactions occur in the first time measurement :



The water formation reaction (1) gives an apparent H/Pd ratio of 2.0, and the hydride formation reaction (2) gives a true value of hydrogen absorption capacity x . The value of x is obtained from the experiment in the second or third time measurement and x is 0.68 ~ 0.70 for the sample of 20wt%Pd/ γ Al₂O₃ as seen in Fig.2.

If the Pd particles are initially 100% oxidized, an apparent H/Pd ratio of ~2.7 should be obtained in the first time measurement. If the Pd particles are partially oxidized, the degree of oxidation is obtained from the difference between the apparent and the true H/Pd values. The observed value of 2.4 for the sample of

Table 1. Variation of H/Pd or D/Pd at 1MPa with the order of measurement cycle for foil and nanomaterials of Pd at 300K.

Material	1st	2nd	3rd	4th
Pd foil	0.74 ± 0.02 (H2)	0.74 ± 0.02 (H2)	0.74 ± 0.02 (H2)	
nanoPd (AY4030)	0.82 ± 0.02 (D2)	0.69 ± 0.02 (D2)	0.70 ± 0.02 (D2)	0.71 ± 0.02 (H2)
13wt%Pd/ γ Al ₂ O ₃	2.7 ± 0.2 (D2)	0.71 ± 0.02 (D2)	0.72 ± 0.02 (D2)	0.72 ± 0.02 (H2)
20wt%Pd/ γ Al ₂ O ₃	2.4 ± 0.2 (H2)	0.68 ± 0.02 (H2)	0.70 ± 0.02 (H2)	
30wt%Pd/ZrO ₂	2.6 ± 0.2 (H2)	0.68 ± 0.02 (H2)	0.70 ± 0.02 (H2)	

20wt%Pd/ γ Al₂O₃ indicates that 85 at% of Pd in the as synthesized sample is in the chemical state of PdO [4]. Similarly, from the PC isotherm measurements, the degree of oxidation of Pd particles in the as-received or as-synthesized samples was estimated to be 6 at%, 100 at% and 95at% for Pd powder AY4030, 13wt%Pd/ γ Al₂O₃ and 30wt%Pd/ZrO₂, respectively.

It should be mentioned that in Fig.2, no difference in the H/Pd ratio at 1MPa is seen between the three measurements, indicating that the foil sample is 100% metallic in the as-received state.

The results of the repetitive measurements of hydrogen/deuterium absorption capacity for nanoPd materials are summarized in Table 1, including the results for the foil sample of Pd. It is seen that the H/Pd or D/Pd ratios of the metallic nanoPd materials are slightly smaller than the value of Pd bulk or the foil sample of Pd.

3. 2. X-ray diffraction

From the repeated measurements of hydrogen absorption capacity, it has been suggested that PdO reduces to metallic Pd during loading of hydrogen up to 1MPa at 300K. Figure 4 shows the X-ray diffraction patterns for the sample of 13wt%Pd/ γ Al₂O₃ before and after the four cyclic PC isotherms measurements [4]. As shown in Fig. 4, the sample before the measurements consists of γ Al₂O₃ and PdO, while the sample after the measurements consists of γ Al₂O₃ and metallic Pd.

It is considered that PdO reduces to metallic Pd during the first time loading of hydrogen, because the H/Pd values at and after the second time measurements do not change as shown in Fig.3. Therefore, PdO easily reduces to metallic Pd once it is exposed to hydrogen at room temperature.

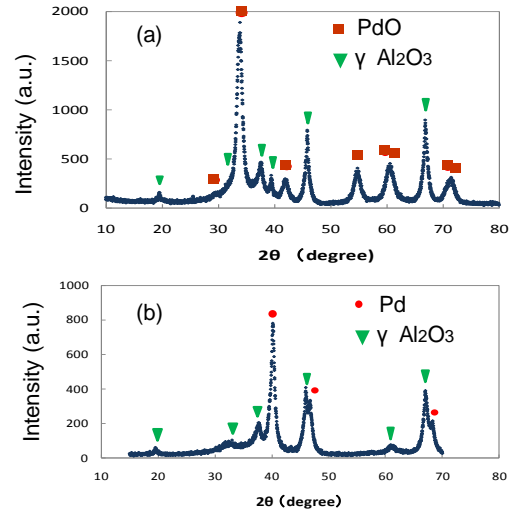


Figure 4. X-ray diffraction pattern for 13wt%Pd/ γ Al₂O₃: (a) before and (b) after repetitive PC isotherms measurements.

3.3. TEM observation

The repetitive measurements of PC isotherms also resulted in a morphological change of Pd particles, i.e., the size of the Pd nanoparticles became larger after the measurements. The change was most remarkable for Pd nanopowder AY4030. Figure 5 compares TEM images

before and after the measurements or the four cycles of loading and deloading with deuterium or hydrogen (first three cycles with D2 and the fourth with H2 [4]).

As seen from the TEM images in Fig.5, the average size of Pd particles is initially 10 ~ 20nm, but it is about 50nm after the four repetitive measurements.

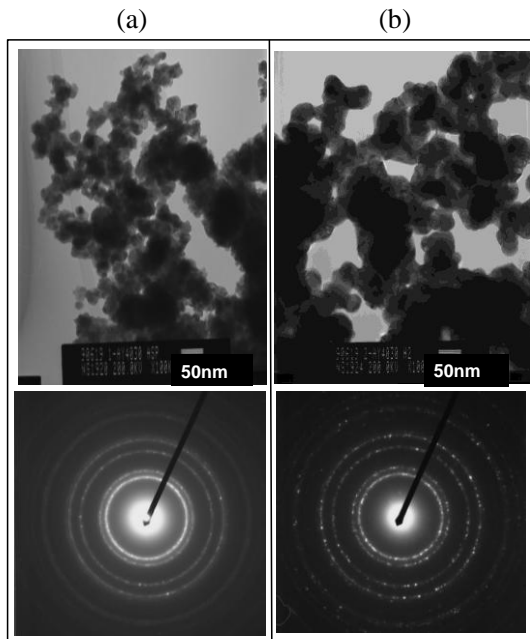


Figure 5. TEM image and electron diffraction rings for (a) before and (b) after four cycles of loading and deloading of deuterium/hydrogen.

The electron diffraction rings are spotted for the sample after the measurements as seen in Fig.5. This fact also indicates that the size of the crystalline grains becomes larger as a result of cycles of loading and deloading of hydrogen or deuterium. Similar increases in the size of Pd particles have also been observed for nanocomposite samples [4, 5]. The observed grain growth is considered to arise from the local temperature rise at the contact point of contacting Pd particles owing to the heat generated by the chemical reactions (1) and (2). However, the melting point of Pd, 1827K, seems to be too high to explain the grain growth by the rise of the local temperature. The degree of oxidation of AY4030 is only 6at% and the heat mainly comes from the hydride formation reaction

(2) with much smaller heat of formation compared to the reaction (1). The reason for the grain growth is not yet fully clear.

It should be mentioned that the measured values of the hydrogen absorption capacity may be for Pd particles with sizes larger than their initial sizes.

3.4. Heat evolution with loading of hydrogen isotope gases

3.4.1. First stage

The composite sample 20wt%Pd/ γ Al₂O₃ of 42.5g (Pd : 8.5g) was mounted in the sample vessel of the calorimeter. The sample was first evacuated, heated up to 523K under vacuum and maintained at the temperature for about 2 hours, followed by cooling to room temperature. Then, deuterium gas was supplied to the sample at a flow rate of about 20ml/min. When the pressure reached a value of 1MPa, the gas supply was stopped and the sample was maintained under a fixed pressure of 1MPa. Figure 6(a) shows the thermal output power and gas pressure as a function of time for the first loading with D₂.

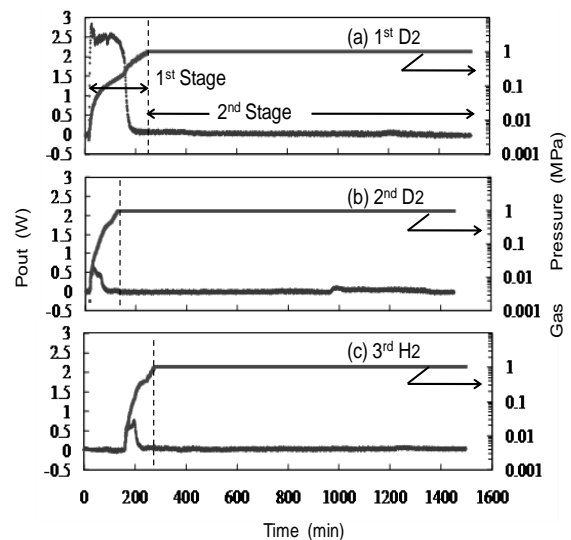


Figure 6. Heat power and gas pressure as a function of time for 20wt%Pd- γ Al₂O₃; (a) the first cycle loading with D₂, (b) the second cycle loading with D₂, (c) the third cycle loading with H₂ [4].

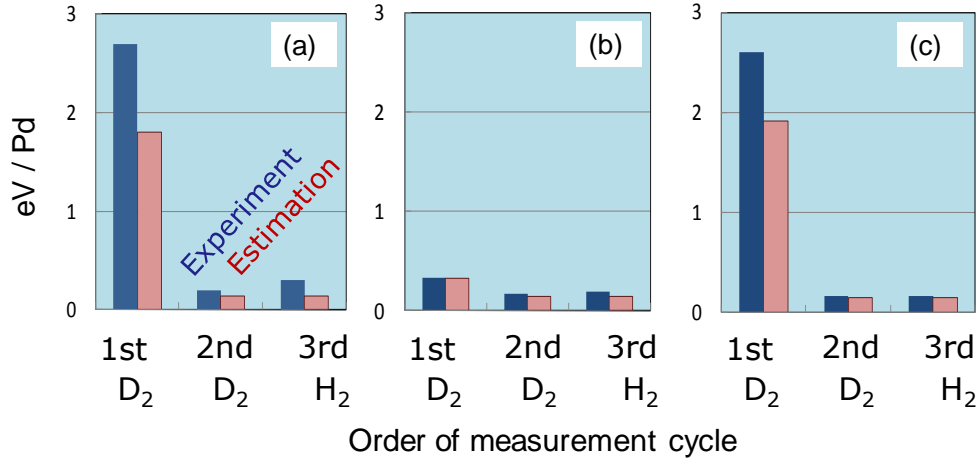


Figure 7. The variation of the heat generated in the first stage with the order of measurement cycle for (a) 20wt%Pd/ γ Al₂O₃, (b) Pd nanopowder AY4030, and (c) 30wt%Pd/ZrO₂. The experimental values are compared to the estimated ones.

After the first measurement of heat evolution, the sample was again evacuated, heated up to 523K, maintained at this temperature for 2h in order to eliminate the absorbed deuterium completely. Then, the sample was subjected to the second loading with D₂ at room temperature (Fig.6 (b)). Similarly, the third loading was conducted with H₂ (Fig.6 (c)). Here we define the first stage as the period where the pressure was raised from 0 to 1MPa, the second stage as the period where the sample was maintained under the fixed pressure of 1MPa. It is clearly seen in Fig.6 that the heat evolution in the first stage is remarkable in the first time measurement while it decreases greatly in the second or third time measurement. This behavior is quite similar to that of hydrogen absorption capacity, suggesting that the heat evolution in the first stage is related with the chemical reactions (1) and (2). In Figure 7, the variation of the heat generated in the first stage with the order of measurement cycle is shown. The experimental values are compared to the estimated ones. The estimation was made assuming that in the first time measurement, both of the reactions (1) and (2) contributed to the heat evolution while only the reaction (2) in the second and third time measurements. The values of $\Delta H(\text{water}) = -178\text{kJ/molPd}$ [8] and ΔH

(hydride) = $\Delta H(\text{deuteride}) = -40\text{kJ/molH}_2$ [9] were used. The ratio of the oxidized Pd to the total Pd before the first time measurement was taken to be 85at% as determined above.

Similar results for Pd nanopowder AY4030 and nanocomposite of Pd/ZrO₂ are also shown in the figure for comparison. It is seen in Fig.7 that the heat generated in the first stage is largely explained by the chemical reactions (1) and (2). Therefore, in the first stage, it seems difficult to identify the heat evolution from nuclear origin, even if a small portion of the generated heat is nuclear.

3.4.2. Second stage

The chemical reactions associated with loading the Pd nanomaterials with hydrogen isotope gases up to 1MPa are considered to cease until the pressure reaches 1MPa. Therefore, in the second stage, where the gas pressure is fixed at 1MPa, no chemical reactions are expected to occur. In Figure 8, the same data as in Fig.6 are shown with the vertical axis magnified by ten times.

It is noted in Fig.8 that in the first and second loadings with D₂, an output power as small as 0.05~0.1W is observed for a period of about three and six hours, respectively. On the other hand, as seen in Fig.8 (c), no such anomalous heat evolution is observed

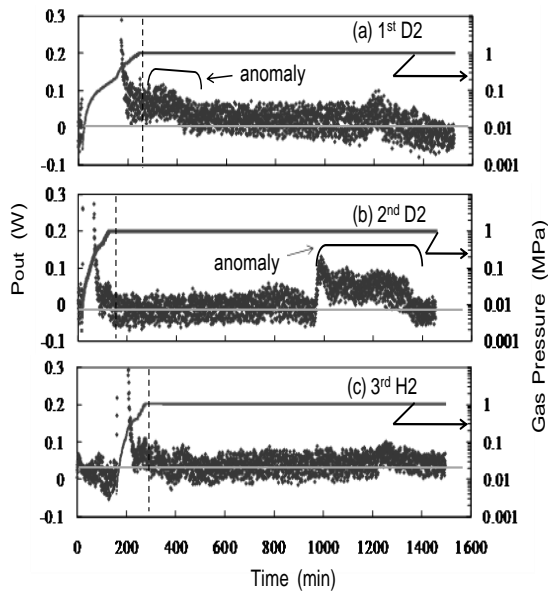


Figure 8. The same data as Fig.6 are shown with the vertical axis enlarged by 10-fold. The vertical dotted line indicates the boundary of the first stage and the second stage, and the horizontal gray lines the zero level of Pout [4].

in the third loading with H2.

Similarly, the results for the Pd nanopowder sample of 26g and the Pd/ZrO₂ sample of 51.4g (Pd: 15.6g) are shown in Figure 9 and Figure 10, respectively. As indicated in the figures, similar evolutions of anomalous heat are also observed for these materials. All of these intermittent, anomalous heat evolutions are observed when the materials are loaded with deuterium. Therefore, it cannot be ruled out that these heat evolutions in the second stage are nuclear origin, as reported by Arata and Zhang and by Kitamura et al. However, in the present study the observed anomalous heat power is as small as 0.05~0.1W which is close to the detection limit of the calorimeter used here. In order to clarify the origin of the anomalous heat evolution in the second stage, it is required to enhance the anomalous heat power and/or to improve the accuracy of the calorimeter.

4. Conclusions

(1) Nanomaterials of Pd often contain PdO, which

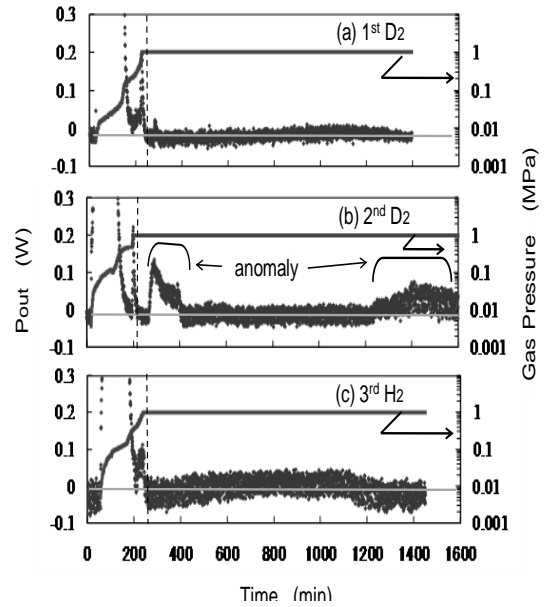


Figure 9. Heat power and gas pressure as a function of time for Pd nanopowder AY4030; (a) the first cycle loading with D2, (b) the second cycle loading with D2, and (c) the third cycle loading with H2. The vertical dotted line indicates the boundary of the first stage and the second stage, and the horizontal gray lines the zero level of Pout [4].

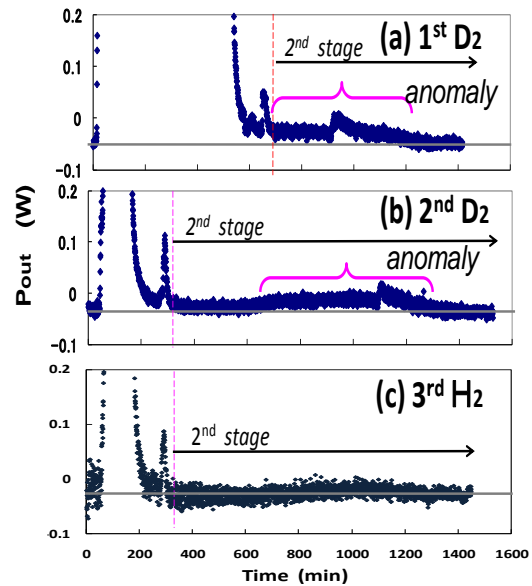


Figure 10. Heat power and gas pressure as a function of time for 30wt%Pd/ZrO₂ nanocomposite; (a) the first cycle loading with D2, (b) the second cycle loading with D2, and (c) the third cycle loading with H2. The vertical dotted line indicates the boundary of the first stage and the second stage, and the horizontal gray lines the zero level of Pout [5].

strongly affects apparent absorption capacity and heat evolution upon loading of hydrogen isotope gases. The extent of oxidation can be estimated from the difference between the apparent and true values of absorption capacity for hydrogen/deuterium.

(2) PdO is reduced to metallic Pd when it is exposed to hydrogen. Therefore, hydrogen absorption capacity of metallic Pd particles is obtained by cyclic measurements of PC isotherms.

(3) The hydrogen absorption capacity H/Pd at 1MPa was 0.70 ± 0.02 for all the nanoPd materials studied here, which was slightly smaller than the value 0.74 of Pd bulk.

(4) The size of the Pd particles was found to be increased significantly after cyclic measurements of PC isotherms.

(5) Similar to the absorption capacity, the heat generated in the first stage was also affected strongly by the degree of oxidation of Pd particles. The experimental value of heat generated in the first stage was largely explained by the water formation reaction and the hydride formation reaction.

(6) When the Pd nanomaterials were loaded with deuterium, a heat power as small as 0.05 ~ 0.1W was observed intermittently in the second stage where chemical reactions were hardly expected to occur.

Acknowledgements

We thank N. Suzuki for TEM observations. We also thank A. Kitamura of Kobe University and A. Takahashi of Technova Inc. for discussions.

References

1. Y. Arata and Y. Zhang, *Journal of High Temperature Society* **34**, 85-93 (2008).
2. A. Kitamura, T. Nohmi, Y. Sasaki, A. Taniike, A. Takahashi, R. Seto, and Y. Fujita, *Physics Letters A* **373**, 3109-3112 (2009).
3. S. Yamaura, K. Sasamori, H. Kimura, A. Inoue, *J. Mater. Res.* **17**, 1329-1334 (2002).
4. T. Hioki, H. Azuma, T. Nishi, A. Itoh, J. Gao, T. Motohiro, and J. Kasagi, *AIP Source Book*, edited by J. Marwan, to be published.
5. T. Hioki, H. Azuma, T. Nishi, A. Itoh, J. Gao, T. Motohiro, and J. Kasagi, submitted to *Proceedings of ICCF15, Rome, Italy, 2009*.
6. Y. Osumi, *Suiso Kyuzo Gokin*, AGNE Gijutsu Center Co. Ltd, Tokyo, 1993, p111 (Jpn).
7. E. Wicke and H. Brodowsky, in *Hydrogen in Metals II*, edited by G. Alefeld and J. Volkl, Springer, Berlin, 1978, p.81.
8. HSC Chemistry 6.1, "Chemical Simulation and Reaction Software with Extensive Thermo-chemical Database", Outokumpu Research, Oy, Finland, (2007).
9. Y. Fukai, K. Tanaka, Y. Uchida, *Suiso to Kinzoku*, Uchida Rokakuho Publishing Co. Ltd., Tokyo, 1998, p.38 (Jpn).

D + D Fusion Acceleration in High Temperature Acoustic Cavitations

Yu TORIYABE and Jirohta KASAGI

Research Center for Electron Photon Science, Tohoku University
Mikamine 1, Taihaku-ku, Sendai 982-0826, Japan
E-mail: toriyabe@lms.tohoku.ac.jp

Li+D and D+D fusion reaction rates in liquid lithium were measured during low energy deuteron beam bombardment. An ultrasonic target system was developed to form acoustic cavitations in the liquid lithium, in order to investigate an effect of material phase and dynamic motion of the target. It was found that the ultrasonic effect strongly depends on a target condition and the D+D reaction could be enhanced several times due to the liquid Li cavitation. This enhancement is caused by not electron screening but high temperature deuterium in the cavity. We fitted the energy dependence of the ultrasonic on/off yield ratio and obtained the temperature in the cavity as $kT_D = 590$ eV (6.8×10^6 K), where the experimental value is consistent with that from numerical simulation. No meaningful bubble fusion event has been observed in this study. However, almost experimental results agreed with the original reports and the theoretical predictions. Hence the bubble fusion is achievable if we can specify the best experimental condition.

1. Introduction

Recently, Taleyarkhan et al. have reported D+D fusion reaction induced in the acoustic cavitations of deuterated acetone (C_3D_6O); so-called bubble fusion[1]. It is widely accepted that temperature in an acoustic cavity is, at least, higher than 10^4 K. Some hydrodynamic calculations predict $10^6 - 10^7$ K[2]. Such high temperature (keV range) deuterium gas can induce nuclear fusion. However, the existence of bubble fusion is still in dispute[3].

We have developed a new ultrasonic (US) system to achieve the acoustic cavitation in metal liquid lithium [4]. Li+D and D+D fusion reactions in liquid phase and cavitation (gas phase) were measured with low energy deuteron beam bombardment. The nuclear reaction rates were compared to investigate an effect of material phase and dynamic motion of the target for the nuclear reaction rate. Furthermore, we tried to detect bubble fusion events in the liquid metal.

2. Experiment

2.1. Ultrasonic System and Li Cavitation

Figure 1 shows a schematic view of the ultrasonic system with situations of vibration amplitudes depending on the position. It should be noted that the sonic wave is not transverse but longitudinal wave to form alternate dense and sparse conditions. A bolt-clamped Langevin-type transducer (BLT) placed outside of the chamber

generates a high amplitude sonic wave. A piezoelectric element is lead zirconate titanate (PZT). When the BLT is driven with an appropriate frequency, it outputs high amplitude waves because of vibration resonance with four piezoelectric elements. Since the resonance condition is determined by the wavelength of the sonic wave, the total length of the system is an important factor. We designed the total length in such a way as the Li target is placed at an anti-node and the resonance frequency is near 19 kHz. An aluminum horn connected to the BLT amplifies the vibration amplitude. The horn has a flange at the node position of the sonic wave and is fixed with the vacuum chamber.

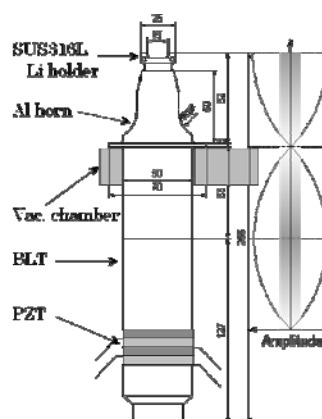


Figure 1. A schematic view of an US system. A Li target is placed at the tip of the system where amplitude becomes anti-node. A horn has a flange at the node position and is fixed with a vacuum chamber wall.

Situations of bubble growth and collapse through US cycles are shown in Fig. 2. At the sparse timing, a nucleus is born, the bubble shrinks and expands through a several cycles and it finally collapses at the dense timing. Then the high pressure, density and temperature state can be achieved and light emission, so called sonoluminescence, occurs.

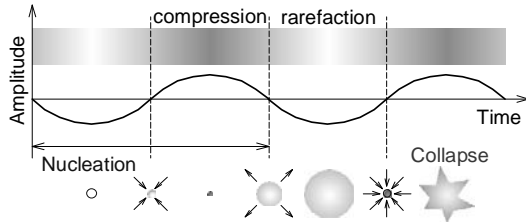


Figure 2. Bubble growth and collapse through US cycles.

2.2. Li+D and D+D Measurement

We used enriched ${}^6\text{Li}$ metal, which consists of 95% ${}^6\text{Li}$ and 5% ${}^7\text{Li}$. The Li metal is very active material, and the surface is easily oxidized and/or contaminated even in the vacuum condition. Therefore we designed and constructed a new vacuum chamber which has a glove box. In order to keep the surface clean, we handled the Li metal in Ar atmosphere in the glove box. The contamination, however, is unavoidable because of the residual gas which is mainly vapor. Thus, we removed the surface contamination every 1 or 2 hours by using a scraper attached to the chamber. We kept the Li temperature considerably higher than the melting point (180 °C). Below 300 °C, the vapor pressure of Li (10⁻⁶ Pa) is much lower than the pressure in the chamber (typically 2 x 10⁻⁵ Pa). Thus Li evaporation can be avoided even under the cavitation condition.

The liquid Li was irradiated by deuteron beams with energy ranging from 30 to 70 keV. The beam was injected to the chamber at an angle of 60° with respect to the vertical direction. A Si detector placed at 125° was used to detect charged particles emitted by the nuclear reactions.

In order to elucidate the ultra sonic effect, we compared the yields of the Li+D and D+D reactions for the US-on and -off states. However, it was found that the target condition was very

sensitive and was easily changed within a several minutes due to high activity of lithium. Therefore a data acquisition system, in which the measurements with and without the US were performed alternately, was developed to reduce systematic errors. As shown in Fig. 3, the beam was turned off and on in every 3 or 10 seconds while the US wave was turned off and on in every 13 seconds so as to accumulate the 4 data sets in one cycle.

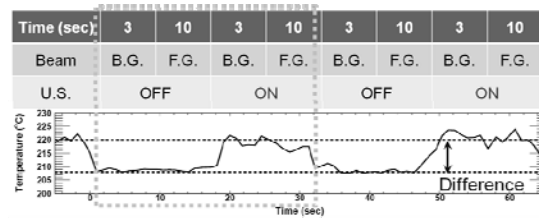


Figure 3. An alternate data acquisition cycle and infrared thermometer output.

In Fig. 3, the reading of the infrared thermometer, which is considered to show the temperature of the Li surface, is also shown. It periodically increases and decreases synchronized with the US on/off cycle. It is not plausible that the change of the reading corresponds to real temperature change because of its instant response. At present, we conjecture that near-infrared lights are emitted in the Li cavitation as the sonoluminescence.

3. Results

A typical energy spectrum is shown in Fig. 4. The blue peak is the 11 MeV α particle from the ${}^6\text{Li}(d,\alpha){}^4\text{He}$ reaction. During the deuteron bombardment, deuterons are being accumulated in the Li target and an incident deuteron collides with them to induce the D+D reaction. The red peak is 3 MeV proton from the D(d,p)T reaction. Estimated deuteron density is about 0.1% of that of the lithium. In this study, we analyzed 11 MeV α and 3 MeV proton only.

We measured reaction rates for many experimental conditions and investigate the US effect. For all experimental conditions, ${}^6\text{Li}(d,\alpha){}^4\text{He}$ reaction has not been enhanced by the US effect. Screening potential of the ${}^6\text{Li}(d,\alpha){}^4\text{He}$ reaction in the liquid/cavitation Li

was determined to be $543 \pm [38(\text{sta.}) + 83(\text{sys.}) - 153(\text{sys.})]$ eV by fitting an excitation function. The additional electron screening could not be generated by the liquid/gas phase transition. Although the screening potential is higher than the value in the LiF insulator target [4], it is reasonable because the liquid Li is ionized as Li^+ and e^- and therefore the ionic Debye screening becomes effective.

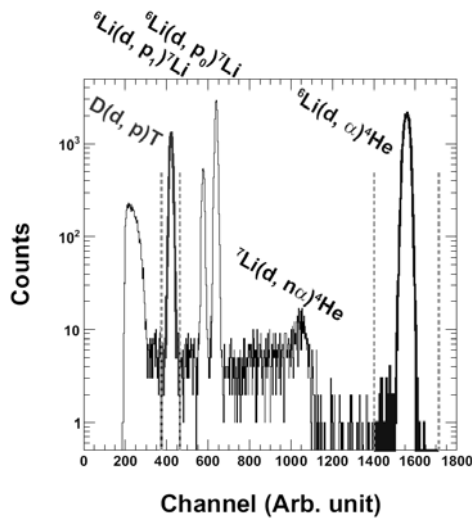


Figure 4. A typical energy spectrum obtained with liquid Li target. A $5 \mu\text{m}$ aluminum absorber covers the detector. A component below 300 channel is summation of some reactions, $\text{D}(d, t)\text{H}$, $\text{D}(d, {}^3\text{He})\text{n}$, and so on.

On the contrary, several times enhancement of the $\text{D}(d, p)\text{T}$ reaction yield has been observed by the US effect. However, the effect strongly depended on the Li surface condition and was unstable. Figure 5 shows the highest enhancement case in the all experiments. The yields of the $\text{Li}+\text{D}$ and $\text{D}+\text{D}$ reactions are plotted as a function of elapsed time with open markers for the US-off and closed markers for the US-on state. The $\text{Li}+\text{D}$ reaction yield is constant and the difference between the US-on and -off states is within the error bar. In Fig. 5 one can see that the $\text{D}+\text{D}$ reaction with the US wave is really enhanced several times. In this run, we obtained the averaged on/off yield ratios to be 1.03 and 5.14 for $\text{Li}+\text{D}$ and $\text{D}+\text{D}$ reactions, respectively. Here the reaction occurs randomly through the US cycle and a time correlation with the US has not been observed up to now.

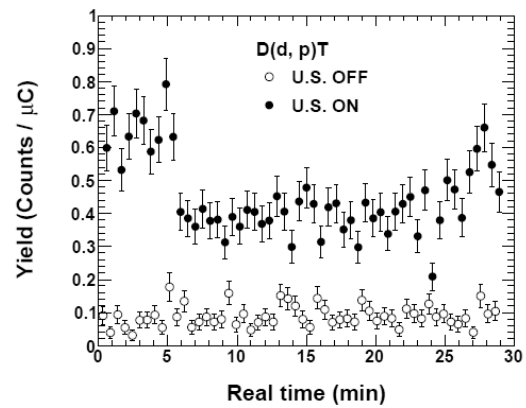
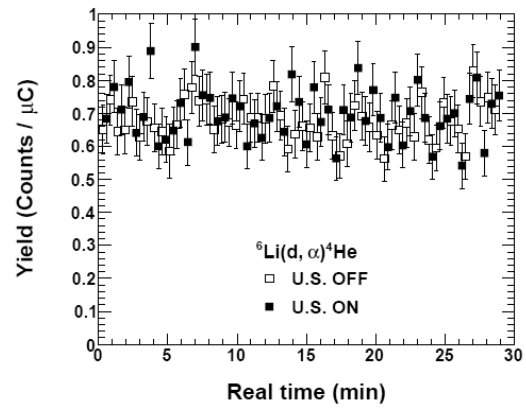


Figure 5. Reaction yield of ${}^6\text{Li}(d, \alpha){}^4\text{He}$ (top) and $\text{D}(d, p)\text{T}$ (bottom) with open markers for U.S. off state and closed markers for U.S. on state where the vibration amplitude is $1.9 \mu\text{m}$. Beam energy is 50 keV, current is $13 \mu\text{A}$. Lithium temperature is about 210°C .

Such strong enhancement has been seldom replicated because the experimental condition is quite sensitive due to the high Li activity. It is hard to keep constant surface condition of the Li target for a long time. We therefore selected a relatively stable condition to measure the energy dependence of the yield ratio. The conditions are fixed at vibration amplitude of $1.9 \mu\text{m}$, surface temperature of 220°C , and beam input of 500 mW.

The energy dependence of the US on/off ratio is shown in Fig. 6. The $\text{D}+\text{D}$ reaction yield ratio has obvious energy dependence. As the incident energy becomes lower, the yield ratio increases. If the reaction is enhanced by the change of the deuteron density only, the energy dependence cannot be observed. Thus, the observed dependence on the incident energy clearly

indicates that not only density effect but another mechanism enhancing the reaction should be effective in the liquid Li cavitation.

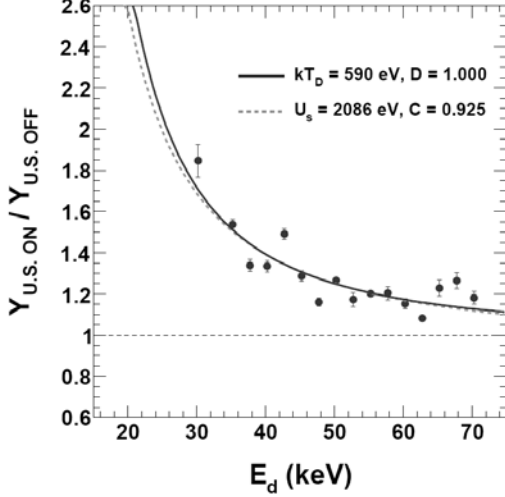


Figure 6. Energy dependence of the D+D reaction yield ratio. A dashed line shows fitting result for an electron screening model with screening potential of 2086 eV. If we suppose high temperature in the cavity, a solid line is obtained as a best result with the temperature of $kT_D = 590$ eV under the gas composition of 65%.

Nuclear reaction enhancement in solid matter is generally expressed as the electron screening effect[5]. When we suppose the screening effect in the Li cavitation, a dashed line in Fig. 6 is obtained as a fitting result. It looks like reasonable to explain the enhancement in this energy region. However, the screening effect predicts much higher reaction rate at background (US-on and beam-off condition) than that observed. This consideration suggests that not the screening but another mechanism should be effective in the Li cavitation.

Some numerical simulations predict that temperature in acoustic cavity reaches to the 10^6 K[6]. Then the deuterium in the cavity has high kinetic energy (in the order of keV) and cross section increases in the case of head on collision. We suppose a Maxwell energy distribution for deuterons in the cavity and fitted the experimental values to determine the average temperature. Here, we estimated the concentration of the gas phase at the liquid Li surface at the same time. A solid line in Fig. 6 shows the fitting result with the average

temperature of $kT_D = 590 \pm [54(\text{sta.}) + 676(\text{sys.}) - 457(\text{sys.})]$ eV (6.8×10^6 K) under the gas composition of 65%. The line agrees with the experimental values as well as that in the screening effect case in this energy region. At lower energy region, the cross section drastically decreases in the case of the high temperature model and it agrees with the observed background rate.

The obtained value 10^6 K is extremely high temperature because the Li temperature keeps 220 °C. However, some numerical simulations predict shock wave formation in a shrinking cavity and temperature reaches up to 10^6 K[6]. If a cavity includes light and heavy elements, the lighter gas is segregated and compressed toward the center of the cavity[2]. Then the temperature of the lighter gas selectively increases while the heavier gas keeps relatively low temperature. This result agrees the experimental results that D+D fusion (lighter target, D) was accelerated while the Li+D (heavier target, Li) fusion was not enhanced. The temperature of the heavier gas, Li, did not increase meaningfully and no enhancement was observed in this study.

4. Conclusions

We have developed the US target system to form the Li acoustic cavitation bubbles in the vacuum chamber. The Li+D and D+D fusion reactions were measured during the low energy deuteron bombardment to the Li target. Although the US effect strongly depends on the target condition, the D+D reaction could be quite enhanced by the cavitation. On the contrary, Li+D reaction has never been enhanced for all experimental conditions.

We measured the energy dependence of the reaction yield under the relatively stable condition. The screening energy in liquid Li for ${}^6\text{Li}(d,\alpha){}^4\text{He}$ is calculated to be 543 eV. The enhancement of the D+D reaction is not caused by the screening but the high temperature in the cavity. We fitted the experimental values as all factors become self-consistent and obtained the deuterium-gas temperature as $kT_D = 590$ eV. This temperature corresponds to 6×10^6 K and its order is almost equivalent to the numerical simulation.

No meaningful bubble fusion event has been observed in this study. However, the experimental results are all consistent with the original reports and the numerical simulations. Hence, we expect the bubble fusion if we can specify the best experimental conditions.

Acknowledgements

The authors thank Mr. Kazue Matsuda, LNS Technical Workshop, for construction of the vacuum chamber with the ultra sonic system.

This study is partially supported by Grants-in-Aid for Scientific Research from the Japan Society for the Promotion of Science.

References

1. R. P. Taleyarkhan, *et al.*, *Science*, **295**, 1868 (2002).
R. P. Taleyarkhan, *et al.*, *Phys. Rev. E*, **69**, 36109 (2004).
R. P. Taleyarkhan, *et al.*, *Phys. Rev. Lett.*, **96**, 179903 (2006).
2. A. Bass, *et al.*, *Phys. Rev. Lett.*, **101**, 234301 (2008).
3. New Energy Times and scientific references therein. (<http://www.newenergytimes.com/>)
4. S. Engstler *et al.*, *Z. Phys.*, **342**, 471 (1992).
5. C. Rolfs and W. Rodney, *Cauldrons in the Cosmos*
6. C. Wu and P. Roberts, *Phys. Rev. Lett.*, **70**, 3424 (1993).
W. Moss, *et al.*, *Phys. Fluids*, **6**, 2979 (1994)

Measurements of heat and radiation from Pd nano-powders during absorption of hydrogen isotopes

Yu Sasaki^a, Yuki Miyoshi^a, Akira Taniike^a, Akira Kitamura^{a*},
Akito Takahashi^b, Reiko Seto^b and Yushi Fujita^b

^aDivision of Marine Engineering, Graduate School of Maritime Sciences, Kobe University, Kobe 658-0022, Japan

^bTechnova Inc., Uchisaiwaicho 1-1-1, Chiyodaku, Tokyo, Japan

*kitamura@maritime.kobe-u.ac.jp

Abstract. Using a twin system for hydrogen absorption, experiments on heat evolution and charged particle generation by D₂ (H₂) gas absorption in nano-sized Pd powders were done for the 0.1- $\mu\text{m}\phi$ Pd powder, the Pd-black, and the mixed oxides of Pd-Zr, Pd-Ni-Zr and Ni-Zr. It has been found that the D(H)/Pd loading ratio and the absorption energy per D (H) are increasing functions of fineness of the sample surface. In a framework of an assumption that the D₂ (H₂) gas flow rate is determined from the rate of increase of the D₂ (H₂) pressure in the reaction chamber, we conclude a very large energy of hydrogen absorption by Pd-Zr oxide compounds exceeding 1.0 eV/D(H) together with a very large D(H)/Pd loading ratio exceeding 1.0. Although the samples were deteriorated by the repeated baking-hydrogenation cycles, an artificial oxidation of the PZ and the PNZ samples almost recovered the excellent original performances.

In addition, nuclear reaction products including energetic charged-particles for a possible cause of the phenomena were examined using a variety of nuclear diagnostics. We have observed a tendency that the charged particle counting increases when the D₂ pressure changes, although it is not well confirmed that these signals originate in nuclear events, and the counting rate is far lower than that expected from an assumed nuclear reaction producing α particles.

Keywords: Pd-Zr nano-powder, Deuterium absorption, D/Pd, Anomaly, Forced oxidation, Charged particles

1. Introduction

The experiment on D₂ gas charging of Pd nano-powders in the form of Pd/ZrO₂ nano-composite made by Arata and Zhang [1] is a sophisticated, yet simplified, version of the previous-generation DS reactor [2]. Although successful replications using systems similar to the DS reactor with Pd-black have been reported [3, 4], few reports on the replication experiments producing heat and ⁴He with the new configuration have been published yet in spite of extreme importance of the phenomenon. It is crucial to confirm the phenomenon of heat and ⁴He generation with fully quantitative reliability.

We have constructed an experimental system to replicate the phenomenon and to investigate the underlying physics [5,6]. The system is composed of two identical reaction chambers, an A₁-A₂ twin system, equipped with calorimetry setups, and a B system for nuclear diagnostics. We report here the results of heat measurements as well as charged particle measurements under deuterium/hydrogen absorption

by a variety of Pd nano-powders, covering our former results [5-11] and newer results.

2. Experimental Apparatus for Calorimetry

The D₂/H₂ absorption system is composed of two identical chambers (an A₁-A₂ twin system): one for a D₂ gas foreground run, and the other for H₂ gas background run. As shown in Fig. 1, each part has an inner reaction chamber containing Pd powder and an outer chamber that is evacuated to provide thermal insulation for calorimetry. A sheath heater and a cooling water pipe made of copper are wound on the outer surface of the reaction chamber for baking the sample powder and for flow calorimetry to measure the heat production rate, respectively. A pair of thermocouples is provided for the flow calorimetry by measuring the temperature difference between the inlet and the outlet of the cooling water. With the coolant flow rate of 6 ml/min, the heat recovery rate was (63.1 \pm 5.8) %. Temperature response to a stepwise variation

of the input power, the indicial response, has an exponential delay with a time constant of 5.2 min.

The D₂ gas is nominally 99.5 % pure and the H₂ is 99.998 % pure. The flow rate of the D₂/H₂ gas purified further through a liquid-nitrogen cold trap was controlled between 1 and 100 sccm with a mechanical needle valve, ‘Super Needle’, which has replaced a Pd membrane filter used in the early stage of the research [5–10], because the precision of adjustment of the membrane temperature was found to be rather poor.

In expectation of occurrence of some nuclear phenomena, a neutron dose rate meter and a scintillation probe for γ -ray detection are located just outside the outer chambers. All parameters measured are stored in a PC with an acquisition period of 1 min. The error or the uncertainty for the output power and the integrated output energy is evaluated to be 0.014 W and 4.0 kJ for 1000-min run.

In the following, the run number is designated by “G-PN#M”, with G, P, N and M being the gas species, the powder species, powder ID, and the number of repeated use, respectively. The powder species include PP (Pd powder with particle diameter of 0.1 μm and a purity of 99.5 %), PB (Pd-black with a particle size of “300 mesh” and purity of 99.9 %), PZ (mixed oxides of Pd-Zr), PNZ (mixed oxides of Pd-Ni-Zr) and NZ

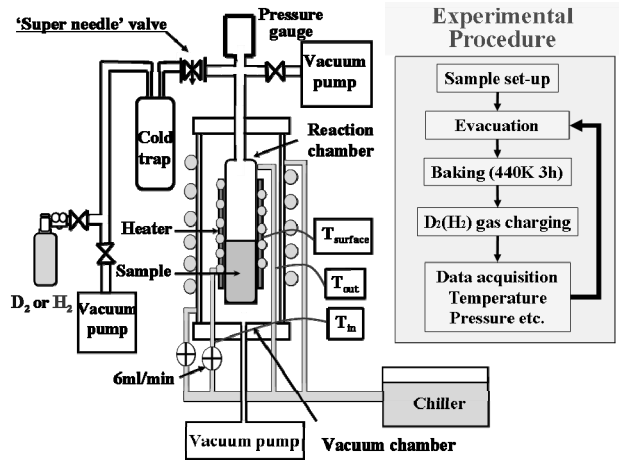


Fig. 1. Schematic of one-half of the twin system. A mechanical needle valve, ‘Super Needle’, has replaced the Pd membrane filter [5-10] for flow rate control.

(mixed oxides of Ni-Zr). Physical properties of the three kinds of mixed oxide samples, PZ, PNZ and NZ, fabricated by Santoku Corporation, Kobe, Japan, are tabulated in Table 1.

In the analysis of the data for the PZ samples, we use an average value of 0.314 for the weight fraction of Pd, which introduces a systematic error of about 5 % to the values of the loading ratio D(H)/Pd and the first phase absorption energy E_{1st} which is considered to be equal to the heat of solution or the hydride formation energy Q_D (Q_H) in the absence of oxide reduction and nuclear process. In the present paper the word “hydride” stands for the deuteride and the hydride in the customary sense.

Table 1. Physical properties of Pd-Ni-Zr oxide samples prepared by Santoku Corp. The fraction depends on the degree of oxidation of Pd, *i.e.*, the ratio of PdO to Pd.

Sample name		PZ		PNZ	NZ
Lot number		081030	090529-1	090609-1	090609-2
molar fraction	Pd	0.346	0.356	0.105	
	Ni			0.253	0.358
	Zr	0.654	0.644	0.642	0.642
	O	1.31~1.65	1.29~1.64	1.54~1.64	1.64
weight fraction	Pd	0.314~0.299	0.328~0.308	0.103~0.101	
	Ni			0.135~0.133	0.197
	Zr	0.508~0.485	0.501~0.478	0.537~0.529	0.555
	O	0.178~0.215	0.176~0.214	0.537~0.237	0.249
Average particle size (μm)		7.7	20.3	23.7	15.5
Specific surface area (m^2/g)		37.1	41.3	35.2	27.6
Average grain size (nm)		10.7	8.3	7.4	(Ni) 23.2

3. Results of Calorimetry

In the early stage of our research, we compared performances of PP, PB and PZ samples [9], and we re-summarize the “revised” results as follows;

(1) The loading ratio D(H)/Pd and the absorption energy E_{1st} are increasing functions of fineness of the sample surface, which increases in the order of the 0.1- $\mu\text{m}\phi$ Pd powder (PP), the 300-mesh Pd-black (PB) and the oxide composites of Pd-Zr (PZ).

(2) For the virgin PB samples, the loading ratios D(H)/Pd = 1.3(1.3) \pm 0.04 and the output energies in the first phase, E_{1st} = 0.42(0.39) \pm 0.07 eV/atom-D(H), are both 3 - 2 times larger than those for the 0.1- $\mu\text{m}\phi$ Pd powder and those found in the literatures [12-17].

(3) The virgin PZ samples has the outstanding performances of the very high loading ratios D(H)/Pd = 1.8(1.7) \pm 0.3 together with the high absorption energies E_{1st} , or the deuteride (hydride) formation energy $Q_{D(H)}$ ranging from 0.92(0.92) to 1.4(1.2) eV/D(H) depending on how much fraction of PdO_x reduction is involved in the measured values of D(H)/Pd and E_{1st} .

(4) The used PB and PZ samples have substantially smaller D(H)/Pd ratios and E_{1st} values which are even smaller than or nearly equal to those for the PP samples. It is inferred that these are due to a clumping-together

effect.

(5) As for the 2nd phase, we observed a few runs with a positive output energy, $E_2 \sim 2.5$ kJ/g-Pd, slightly exceeding the experimental error of about 2 kJ/g-Pd due to a baseline drift. An example is shown in Fig. 2.

Here we have reevaluated (“revised”) the values of D(H)/Pd and E_{1st} based on a newly evaluated value (1.2×10^2 cc) of the reaction chamber. The averaged values of the measured parameters are summarized in the last two lines of Table 2 for eight virgin PZ samples (D(H)-PZ*#1).

We have rather large values of D/Pd (H/Pd). To deduce these values, we have assumed that the pressure change is caused solely by consumption of D₂ (H₂) gas

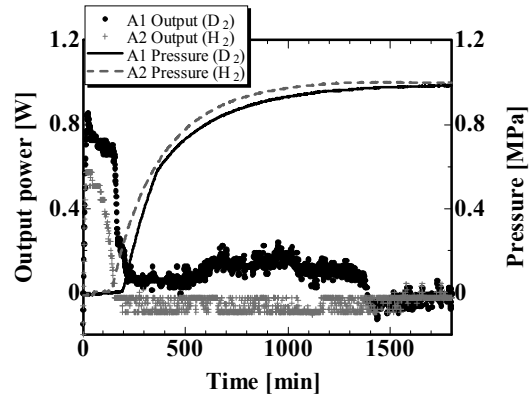


Fig. 2. Evolution of heat and pressure in the reaction chamber after introduction of D₂ gas (blue/light blue) or to H₂ gas (red/pink) for the Pd-ZrO₂ sample (D-PZ1#1 and H-PZ2#1).

Table 2. Artificial oxidation to find the D (H) absorption energy for the Pd-Zr nano-composite (PZ). It is assumed that the reaction proceeds via oxygen pickup from PdO_x followed by hydridation to PdD_y (PdH_y), *i.e.* PdO_x+(x+y/2)D₂ → xD₂O+PdD_y, the absorption energy Q_D (Q_H) is calculated from the relationship; $E_1 = E_{1st} \cdot y = Q_{red} \cdot x + Q_{D(H)} \cdot y$ [eV/atom-Pd], where the reduction energy $Q_{red} = 1.85$ (1.68) eV for D (H) is assumed: (m), (c) and (a) mean “measured”, “calculated” and “assumed”, respectively.

Run	1st phase						2nd phase	Remarks
	Flow rate [sccm]	Specific output energy E_1 [kJ/g-Pd]	D/Pd or H/Pd (= y)	E_{1st} per D/H atom [eV]	O/Pd (= x)	Q_D or Q_H [eV/D(H)]	Specific output energy E_2 [kJ/g-Pd]	
D-PZ1#3	12.0	1.45 \pm 0.01	1.58 (m)	1.06 (m)	0.081 (m)	0.97 (c)	1.37 \pm 1.28	artificially oxidized
H-PZ2#3	19.8	0.89 \pm 0.01	1.06 (m)	0.96 (m)	0.048 (m)	0.89 (c)	0.29 \pm 1.28	
D-PZ*#1 avg	---	2.25 \pm 0.10	1.79 (m)	1.41 (m)	0.46 (c)	0.97 (a)	1.08 \pm 0.67	Q_D and Q_H assumed.
H-PZ*#1 avg	---	1.83 \pm 0.53	1.67 (m)	1.22 (m)	0.33 (c)	0.89 (a)	-0.63 \pm 1.34	

due to formation of PdD (PdH). As was mentioned earlier, some fraction of Pd atoms in the Pd-Zr oxide samples is in the form of PdO. X-ray diffraction measurements after D (H) absorption experiments have revealed almost perfect reduction to Pd to replace D₂ (H₂) by D₂O (H₂O) molecules. If the D₂O (H₂O) molecules happen to condense into the liquid phase to give almost no contribution to the pressure in the reaction chamber, possible reduction of PdO could lead to overestimation of the amount of the D₂ (H₂) gas absorbed by Pd, and therefore of the loading ratio D/Pd (H/Pd). However, the sample is in vacuum, and therefore the water molecules will remain in the gas phase at least until the time when we evaluate the rate of pressure increase, which, multiplied by the duration of the first phase, is used to calculate the amount of D₂ (H₂) gas absorbed into the sample. Therefore, there is little chance to overestimate the amount of the gas absorbed for the formation of PdD(H), since the same volume of D₂O (H₂O) is liberated in the gas phase in exchange for consumption of D₂ (H₂) for the PdO reduction.

To examine the contribution of PdO reduction to E_{1st} , the used PZ1 and PZ2 samples were artificially oxidized by keeping them in O₂ atmosphere. The reaction chamber was initially filled with O₂ gas at a pressure of 0.1 MPa, and kept at a temperature of 470K for 33 hrs without supplying additional O₂ gas into the closed chamber. Assuming that the samples had no oxygen before this process, the extent of the sample oxidation, *i.e.*, x for PdO _{x} , was calculated from the pressure drop in the reaction chamber. The values of x were rather modest, being below 10 %, which are given in the sixth column in Table 2.

The D₂ (H₂) absorption runs after the oxidation, D-PZ1#3 and H-PZ2#3, showed substantial recovery of

D(H)/Pd and E_{1st} , as is shown in the upper two lines in Table 2. Since we know the values of x for these samples, we can eliminate the reduction energy from E_{1st} to obtain the hydride formation energy, Q_D (Q_H). It is assumed here that the reaction proceeds via oxygen pickup from PdO _{x} followed by hydridation to PdD _{y} , or PdH _{y} ; PdO _{x} +($x+y/2$)D₂ → x D₂O+PdD _{y} , or PdO _{x} +($x+y/2$)H₂ → x H₂O+PdH _{y} . The hydride formation energy Q_D (Q_H) is calculated from a relationship; $E_1 = E_{1st} \times y = Q_{red} \times x + Q_{D(H)} \times y$ [eV/atom-Pd], where the reduction energy $Q_{red} = 1.85$ (1.68) eV for D (H) is assumed. In the table, (m), (c) and (a) stand for “measured”, “calculated” and “assumed”, respectively. It is found that the hydride formation energies, $Q_D = 0.97$ eV and $Q_H = 0.89$ eV, are about twice as large as those for the PB samples, and about 2 ~ 5 times larger than the PP samples or the published values for the bulk Pd ranging from 0.2 eV to 0.45 eV [12 - 17].

Once we have known Q_D (Q_H), we can estimate x for the virgin PZ samples using the same relationship, under an assumption that the hydride formation energies Q_D and Q_H remain unchanged after the oxidation process. These are shown in the 6th cells of the lower two lines in Table 2. We see that rather reasonable values of $x = 0.46 \sim 0.33$ are obtained.

Next, the performances of the mixed oxide samples PNZ and NZ are described. The former type of the mixture was used in ref. [1], and was found, they say, to give the best performance for the “excess” heat generation. The results of eight runs using the PNZ samples are summarized in the upper eight lines in Table 3. Similarly to the runs with the PZ samples, the runs H-PNZ2# m were performed simultaneously with D-PNZ1# m , where $m = 1, 2, 3$ and 4. The samples PNZ1 and PNZ2 stayed in each reaction chamber during these runs. Table 3 also includes the results of

Table 3. Results of runs using samples containing Ni, PNZ and NZ. The same procedure was applied to obtain Q_D and Q_H for #3 and #4 runs, and estimate x for #1 and #2 runs.

Run	1st phase						2nd phase	Remarks
	Flow rate [sccm]	Specific output energy E_1 [kJ/g-Pd]	D/Pd or H/Pd (= y)	E_{1st} per D/H atom [eV]	O/Pd (= x)	Q_D or Q_H [eV/D(H)]	Specific output energy E_2 [kJ/g-Pd]	
D-PNZ1#1	9.1	1.74±0.03	1.53 (m)	1.26 (m)	0.16 (c)	1.08 (a)	1.01±0.45	Q_D (Q_H) assumed to calculate x
H-PNZ2#1	18.1	1.86±0.03	1.53 (m)	1.34 (m)	0.26 (c)	1.06 (a)	0.10±0.45	
D-PNZ1#2	8.8	0.12±0.03	0.16 (m)	0.78 (m)	-0.029 (c)	1.08 (a)	5.78±3.18	
H-PNZ2#2	18.5	0.14±0.03	0.17 (m)	0.89 (m)	-0.019 (c)	1.06 (a)	2.18±3.18	
D-PNZ1#3	8.5	0.73±0.02	0.63 (m)	1.28 (m)	0.044 (m)	1.16 (c)	0.91±0.72	artificially oxidized
H-PNZ2#3	18.2	0.75±0.02	0.67 (m)	1.23 (m)	0.032 (m)	1.16 (c)	-0.66±0.72	
D-PNZ1#4	8.8	0.84±0.03	0.82 (m)	1.14 (m)	0.063 (m)	1.01 (c)	-0.31±1.83	
H-PNZ2#4	19.6	0.87±0.02	0.91 (m)	1.05 (m)	0.047 (m)	0.97 (c)	-0.03±1.85	
D-NZ1#2	11.4	0.0 (Ni)	0.0 (/Ni)	---	---	---	0.0 (/Ni)	
H-NZ2#2	21.3	0.0 (Ni)	0.0 (/Ni)	---	---	---	0.0 (/Ni)	

two runs using the NZ samples in the last two lines. The PNZ or NZ samples used was 10 g or 20 g, each containing 1.02 g or 0 g of Pd, respectively. The processing conditions for baking and oxidation were similar to those for the PZ samples.

We see that the loading ratio, D(H)/Pd, and the output energy in the first phase, E_{1st} , evaluated for one D(H) atom are essentially the same as those for the PZ sample. Also results similar to the PZ sample are much smaller D(H)/Pd ratios in the #2 runs. At the first glance these facts mean that Ni has no contribution to the heat evolution. However, there seems to be some characteristic features of the PNZ sample. One is that E_{1st} does not decrease so pronouncedly in the #2 runs. The other is the effect of artificial oxidation of the sample. The oxidation provides a distinguished recovery of the high values of E_{1st} and a modest recovery of the D(H)/Pd ratios, as can be seen in the #3 and the #4 runs with artificial oxidation of the used samples. Similarly to the PZ sample, the modest oxidation of 3 – 6 % has induced a modest recovery of D(H)/Pd and a pronounced recovery of E_{1st} to the initial values.

As has been done for the PZ sample, Q_D (Q_H) is calculated from the known values of x to find even

higher values than the PZ sample. And again we apply the mean values of Q_D (Q_H) for estimation of x for the virgin samples to confirm reasonable values of x . The same procedure is applied to the #2 runs just after the #1 runs followed only by baking. The values of x are negative but very close to zero, which implies that the above procedure is quite reasonable.

For the NZ sample, we have observed definitely no interval with $p = 0$ nor any positive outlet-inlet temperature difference; the NZ sample gives negligibly small D(H) absorption rate and heat evolution. This fact makes us confirm not only that Ni in the present samples has only a second-order effect on the hydrogen absorption and the heat evolution but also that the ZrO₂ matrix has no effect on the hydrogen absorption nor heat evolution. We confirm also that the sample NZ has negligible amount of impurity elements except oxygen. The same must be true also for the PZ and the PNZ samples, since these samples were fabricated by the same recipe. These points assure validity of the quantitative discussion made above for the PZ and the PNZ samples.

For the PNZ sample we have observed a positive output signal in the second phase exceeding the error range recorded for more than two days. We have to

look into a possible zero-level drift of the thermocouple signal, before definitely concluding a positive output power in the second phase.

We claim in the present work that;

- (6) The outstanding performances of the PZ sample, which deteriorate by the repeated use and/or the baking treatment, are restored significantly by oxidizing a small amount (only less than 10 %) of the sample.
- (7) The PNZ sample has the performances similar to those for the PZ sample, when evaluated by the values per one Pd atom. It shows even more pronounced recovery by oxidizing process.
- (8) The NZ sample absorbs essentially no hydrogen isotopes under the present experimental condition.
- (9) As for the second phase, we have positive output exceeding the error range for the deuterium runs employing both the virgin PZ and the used PZ samples and the PNZ sample, which should be confirmed by further investigation.

4. Search for Reaction Products

Little space is left to fully describe the details of nuclear diagnostics using the B-system. Since the details are found in ref. [10,11], only a brief summary is given here.

We have observed several to several tens of counts in the 1 - 10 MeV range of a charged particle kinetic energy, which appeared to be emitted coincidentally with pressure change. However, we cannot rule out the possibility that they are due to electronic noise or contamination of ^{241}Am . Up to now, we have got no firm evidence of charged particle emission, nor burst of high energy particles corresponding quantitatively to any heat observed in the A_1 - A_2 twin system. There remains a possibility that the conditions including the gas introduction procedure for the B-system were not

suitable for the possible excess heat evolution. We are planning detection of X-rays as another candidate for the reaction products.

REFERENCES

- [1] Y. Arata and Y. Zhang: The special report on research project for creation of new energy, J. High Temperature Society, 2008, No. 1.
- [2] Y. Arata, and Y. Zhang: *Condensed Matter Nuclear Science, Proc. 12th Int. Conf. on Cold Fusion* (ed. A. Takahashi, Y. Iwamura, and K. Ota, World Scientific, 2006) pp.44-54.
- [3] V. A. Kirkinskii, A. I. Kumelnikov: *Proc. ICCF13, Sochi, 2007* (Publisher Center MATI, Moscow, ISBN 978-5-93271-428-7) pp.43-46.
- [4] J. P. Biberian and N. Armanet: *ibid.* pp.170-180.
- [5] T. Nohmi, Y. Sasaki, T. Yamaguchi, A. Taniike, A. Kitamura, A. Takahashi, R. Seto, and Y. Fujita: <http://www.ler-canr.org>; to be published in *Proc. 14th Int. Conf. Condensed Matter Nuclear Science* (ICCF14), Washington DC, 2008.
- [6] Y. Sasaki, A. Kitamura, T. Nohmi, Y. Miyoshi, A. Taniike, A. Takahashi, R. Seto, and Y. Fujita: *Proc. 9th Meeting of Japan CF-Research Society* (2009) 29-34; <http://www.lenr-canr.org/acrobat/SasakiYdeuteriumg.pdf>.
- [7] A. Takahashi, A. Kitamura, T. Nohmi, Y. Sasaki, Y. Miyoshi, A. Taniike, R. Seto, and Y. Fujita: *ibid.* pp.35-41; <http://www.lenr-canr.org/acrobat/TakahashiAdeuteriumg.pdf>.
- [8] A. Kitamura, T. Nohmi, Y. Sasaki, A. Taniike, A. Takahashi, R. Seto, and Y. Fujita: *Physics Letters A*, **373** (2009) 3109–3112.
- [9] Y. Sasaki, A. Kitamura, Y. Miyoshi, T. Nohmi, A. Taniike, A. Takahashi, R. Seto and Y. Fujita: to be published in *Proc. 15th Int. Conf. Condensed Matter Nuclear Science* (ICCF15), Rome, 2009; http://iccf15.frascati.enea.it/ICCF15-PRESENTATIONS/S7_O5_Sasaki.pdf
- [10] A. Takahashi, A. Kitamura, Y. Sasaki, Y. Miyoshi, T. Nohmi, A. Taniike, Y. Furuyama, R. Seto and Y. Fujita: *ibid.*; /S2_O4_Takahashi.pdf
- [11] A. Kitamura, Y. Sasaki, Y. Miyoshi, T. Nohmi, T. Yamaguchi, A. Taniike, Y. Furuyama, A. Takahashi, R. Seto and Y. Fujita: *ibid.*; /S3_O2_Kitamura.pdf
- [12] *Hydrogen in Metals II -Topics in Applied Physics*, **29**, ed. G. Alefeld and J. Voelkl (Springer, 1978).
- [13] A. Koiwai, A. Itoh, and T. Hioki: Japan Patent 2005-21860 (P2005-21860A).
- [14] C. P. Chang, *et al.*: *Int. J. Hydrogen Energy*, **16**, 491 (1991).
- [15] M. M. Antonova: *Sboistva Gidriedov Metallov (Properties of Metal-hydrides)* (Naukova Dumka, Kiev, 1975; translated by NissoTsushinsha, Wakayama, 1976) [in Japanese].
- [16] Y. Fukai, K. Tanaka, and H. Uchida: *Hydrogen and Metals* (Uchida Rokakuho, Tokyo, 1998) [in Japanese].
- [17] P. Chou and M. A. Vannice: *J. Catalysis*, **104** (1987) 1-16.

Absorption/adsorption processes of hydrogen isotopes observed for Pd nano-powders

Y. Miyoshi^{1*}, Y. Sasaki¹, A. Taniike¹, A. Kitamura¹

A. Takahashi², R. Seto², and Y. Fujita²

¹Division of Marine Engineering, Graduate School of Maritime Sciences, Kobe University;

Higashinada-ku, Kobe 6580022, Japan; *101w527w@stu.kobe-u.ac.jp

²Technova Inc., Chiyoda-ku, Tokyo 1000011, Japan

Abstract: The absorption/adsorption system has been improved to enable measurements of time-dependent $D_2(H_2)$ gas flow rate and loading ratio $D(H)/Pd$ simultaneously with the output energy. It has been revealed that there exists the new second phase, where $D(H)/Pd$ once decreases, following the first phase where the most of abnormally large output energy is produced by very high loading. The run using the sample after forced oxidation enabled evaluation of the “hydridation” energy that is about 1.5 times and 4 times larger than the adsorption energy and the absorption energy, respectively.

Keywords: Pd-Zr nano-powder, Deuterium absorption, Time-resolved, D/Pd , Forced oxidation, Heat evolution

1. Introduction

The present paper describes the latter half (stage II) of the comprehensive work recently done by the Kobe group, Kobe University and Technova Inc., following the paper JCF10-3 for the first half (stage I) written by Y. Sasaki [1]. In the stage I experiments, we obtained the amount of hydrogen isotopes absorbed by the samples of Pd as a product of $D_2(H_2)$ gas flow rate and the first phase duration, with the former being calculated from a rate of the pressure increase in the reaction chamber at the beginning of the second phase. This procedure is reasonable, if absorption ends completely when the second phase begins. Otherwise, the D_2 or H_2 loading ratio, $D(H)/Pd$, will be underestimated. Moreover, when an unidentified absorber exists besides Pd, the ratio $D(H)/Pd$ will be overestimated.

In the present work, we have made an improvement to equip the system with sub-tanks with pressure gauges to directly measure flow rate and loading ratio, as shown in Fig. 1. Deuterium (or protium) gas is stored in this sub-tank beforehand, and then absorption runs are initiated

after closing the gas supply valve on the head of the gas cylinder to make the system a closed system. With this improvement, we can expect accurate time-resolved measurements of absorbed amount of gas as well as the flow rate, during a $D(H)$ gas-loading run.

2. Experimental procedure

To start an absorption run, the sub-tanks are filled with $D_2(H_2)$ gas at a pressure of 1.0 MPa, and just before the gas is introduced into the reaction chamber through the “Super Needle” valve, the gas cylinder is separated by closing the head valve to make the reservoir-reaction chamber system a closed system.

To analyze the heat evolution, we assume that the chemical reaction that proceeds in the sample is expressed as the following equation (1D or 1H), which is a combination of an oxygen pickup reaction forming D_2O (or H_2O) with a reduction energy of Q_{red} [eV/atom-Pd] and “hydridation” reaction forming hydride atoms $PdD(H)$ and surface adatoms with a reaction energy of $Q_{D(H)}$ [eV/atom-D(H)].

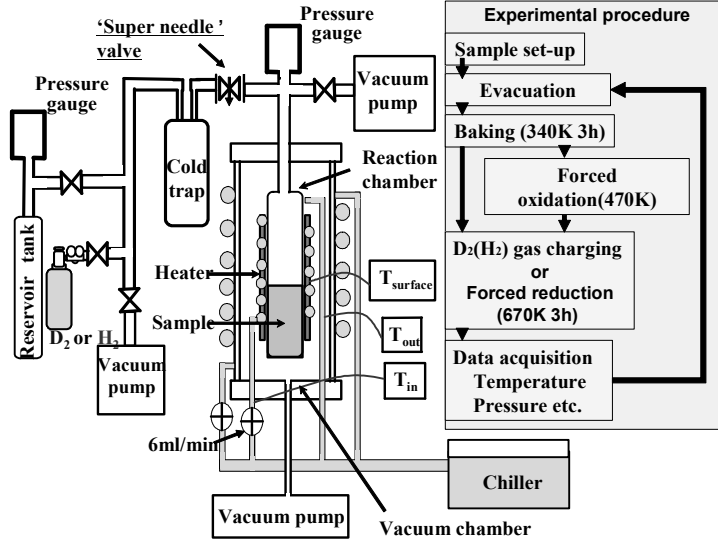
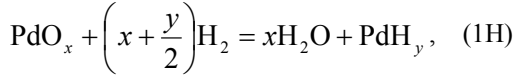
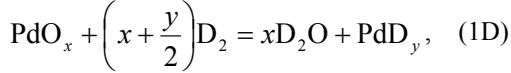


Fig. 1. Schematic of the experimental apparatus.



Here a fraction x of Pd is assumed to have been oxidized and a fraction y of Pd is deuterized (or hydridized) after introduction of D_2 (H_2).

The specific output energy, E_1 either in unit of [kJ/g-Pd] or [eV/atom-Pd] is expressed as

$$E_1 = yE_{1st} = xQ_{red} + yQ_{D(H)}. \quad (2)$$

The fraction y and the energy $Q_{D(H)}$ may include the those of bulk hydride formation and adsorption to the Pd particle surface as well as other possible reactions. We take the value of Q_{red} (= 1.85 (1.68) eV/atom-Pd) from literatures.

The mass conservation law during the gas introduction through the Super Needle requires the following equation (3);

$$\frac{P_1 V_1}{N_A k T_1} = \frac{P_1 V_1}{N_A k T_1} + \frac{P_2 V_2}{N_A k T_2} + \left(\ell x + \frac{y}{2}\right), \quad (3)$$

where (V_1, P_1) and (V_2, P_2) are the (volume, pressure) of the upstream chamber (suffix 1) and the downstream chamber (suffix 2) subdivided by the Super Needle, respectively, both including the

connecting pipes. And ℓ means the fraction of liquid D_2O (H_2O) generated as a result of the reaction. The third term in the right hand side of eq. (3) represents the amount (in mol) of D_2 (H_2) molecules that lose volume as a result of liquefaction or absorption.

The runs D(H)-PZ2(1)#4 and #5 listed in Table 1 and 2 were done by using this system. These are the runs after forced reduction (#4), and after forced oxidation

(#5). The forced reduction of PdO was done by leaving it in atmospheric deuterium/protium (0.2 or 0.1 MPa) gas at a temperature of 673 K for 10 or 30 hours. It is assumed that the sample was completely reduced to become pure Pd-ZrO₂. On the other hand, the forced oxidation of Pd was done in atmospheric oxygen gas (0.1MPa) at a temperature of 473 K for 5 hours. It is assumed that (100· x) % of the Pd atoms was converted to PdO, namely forming PdO _{x} -ZrO₂, through this procedure.

3. Forced reduction of the sample

Forced reduction of the sample was first applied to the used samples of PZ1 and PZ2 just after finishing the runs D(H)-PZ2(1)#3. Figure 2 shows time-dependent heat output and pressure (a) in the reaction chamber and the loading ratio D(H)/Pd (b) in the runs D(H)-PZ2(1)#4. Data analysis was made with $x = 0$ in eq's (1) and (2), because it is thought that no PdO molecules are left in the sample immediately after forced reduction.

Table 1. Results of PZ1.2#4, for forced oxygen reduction

Run #	1 st phase			2 nd phase		3 rd phase	
	Specific output energy $E_1 = xQ_r + yQ_a$ [eV/atom-Pd]	D/Pd (H/Pd) ($=y$)	Reduction energy, xQ_r [eV/atom-Pd]	Hydridation energy, $Q_{D(H)}$ [eV/atom-D(H)]	Minimum value of D/Pd (H/Pd)	Specific output energy E_2 [eV/atom-Pd]	Specific output energy E_3 [eV/atom-Pd]
D-PZ2#4	0.19 ± 0.01	0.69 ± 0.08	0.00	0.28 ± 0.03	0.62 ± 0.08	0.10 ± 0.05	1.52 ± 1.42
H-PZ1#4	0.19 ± 0.01	0.66 ± 0.08	0.00	0.29 ± 0.03	0.52 ± 0.08	0.06 ± 0.04	0.28 ± 1.21

The loading ratio D(H)/Pd increases until it takes the local maximum value of 0.69(0.66) ± 0.08 at about 12 min after initiation of the gas introduction, when heat generation also reaches the local maximum value. It decreases by about 10% till $t \sim 100$ min, and rises again almost at a constant rate. When we take into account the thermal time constant of 5.2 min, the heat generation in the first phase is thought to cease before 12 minutes. We notice that the absorption

and the adsorption process have ended at the time when D(H)/Pd becomes the local maximum.

Then we see that D(H)/Pd ($=y$) = 0.69 ± 0.08 (0.66 ± 0.08), and that the specific output energy $E_1 = 0.19$ (0.19) eV/atom-Pd in the first phase. In this run, because no Pd atoms are assumed to remain oxidized, *i.e.*, $x = 0$, we have the value of $Q_{D(H)} = 0.28 \pm 0.03$ (0.29 ± 0.03) eV/atom-D(H).

The ‘‘hydridation’’ energy $Q_{D(H)}$ is considered to be an average of the bulk hydride formation energy ($\cong 0.2$ eV) and the surface adsorption energy ($\cong 0.5$ eV) weighted respectively by the number of the total atoms in the octahedral sites and the adsorbed atoms on the surface of the Pd nano-particles. Since the numbers of octahedral sites and surface dangling bonds are 2.4×10^4 and 5.1×10^3 , respectively, for the 10-nm-diam. Pd particle, the averaged value $Q_{D(H)}^{\text{full}}$ is 0.25 eV, when both sites are fully occupied. The measured value of $Q_{D(H)} = 0.28 \pm 0.03$ (0.29 ± 0.03) eV/atom-D(H) is larger than this value by about 20 %. Usually it is very difficult to attain full loading, D(H)/Pd > 1 , to the octahedral sites, as is the present case. When D(H)/Pd < 1 , the surface sites are preferentially occupied. The result is that $Q_{D(H)} > 0.25$ eV/atom-D(H), which is consistent with the experimental result.

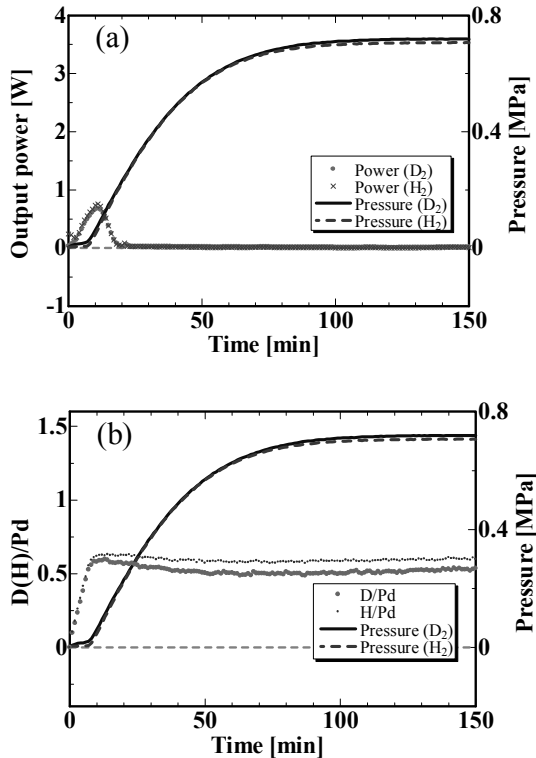


Fig. 2. (a) Evolution of heat and pressure in the reaction chamber after introduction of D₂ gas (solid) or to H₂ gas (dotted) for the Pd-ZrO₂ sample (D-PZ1#4 and H-PZ2#4), and (b) Evolution of D(H)/Pd and pressure in the same runs as above.

The second point to be noted is a decrease and an increase of D(H)/Pd in the second phase. The increase was observed to continue steadily

for more than 4000 min. This is thought to be a reflection of continuous leakage of the gas from the system, since any decrease in the pressure in the closed system is regarded as absorption by the sample, which means increase of $D(H)/Pd$ in the calculation. It is therefore inferred that the loading ratio in the second phase actually saturates at the local minimum value. The interesting point is the existence of the local maximum value or a decrease of $D(H)/Pd$, that is, the $D(H)$ atoms once absorbed appears to have been discharged partially. Here, we redefine a new second phase as the period of decreasing loading, and a third phase after reaching the saturated loading.

If there are some D_2O (H_2O) atoms in the system, and if they happen to condense into the liquid phase with negligible volume, as the pressure rises in the second and the third phase, the result would be an overestimation of $D(H)/Pd$ ($= y$) due to a positive ℓ (cf. eq. (3)). But this is not possible, because D_2O is assumed not to exist in this run.

It is difficult at present to find any reasonable explanation to the change in $D(H)/Pd$ in the second phase. The measurement deviation due to uncertainty in the reservoir capacity, on the basis of which the volume of each part of the system was measured, and a possible zero-point shift of the pressure gauge, etc., is found to be 2 % at most, and therefore it cannot explain the observed range (5 ~ 10 %) of the decrease. Moreover, the temperature rise by absorption and adsorption is about 1K at most, which is rather difficult to affect the value of $D(H)/Pd$.

4. Forced oxidation of the sample

After finishing the $D(H)$ -PZ2(1)#4 run, the forced oxidation of Pd the PZ sample was done by leaving it in atmospheric oxygen gas (0.1MPa) at

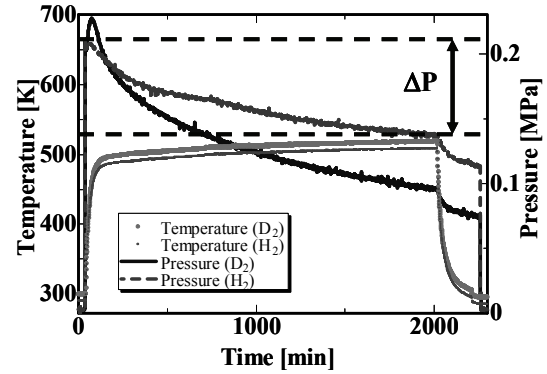


Fig. 3. Change in Oxygen pressure during forced oxidation of used PZ samples.

a temperature of 473 K for 5 hours. The oxidation fraction, x of PdO_x , is calculated from the pressure change in the reaction chamber during the oxidation process (see Fig. 3), and is 0.039 (0.041) for $D(H)$ -PZ2(1). Figure 4 shows time-dependent heat output and pressure in the reaction chamber as well as the loading ratio $D(H)/Pd$ in the run $D(H)$ -PZ2(1)#4.

We notice that the characteristics has been recovered greatly by oxidizing only several % of the sample, similarly to the run $D(H)$ -PZ2(1)#3 described in our preceding presentation [1]. Also similarly to the reduced sample run $D(H)$ -PZ1#4 described in the preceding section, the absorption history has the new second phase when the ratio $D(H)/Pd$ decreases between 25 and 100 minutes, which is followed by the third phase when the ratio keeps increasing due to the leakage of $D_2(H_2)$. It can be assumed that the first phase ends at 18 ± 1 (14 ± 1) minutes from consideration similar to preceding section. Though $x = 0.039$

Table 2. Results of PZ1.2#5, for forced oxidation (about 4% PdO) samples

Run #	1 st phase			2 nd phase		3 rd phase	
	Specific output energy $E_1 = xQ_r + yQ_a$ [eV/atom-Pd]	D/Pd (H/Pd) ($=y$)	Reduction energy, xQ_r [eV/atom-Pd]	Hydridation energy, $Q_{D(H)}$ [eV/atom-D(H)]	Minimum value of D/Pd (H/Pd)	Specific output energy E_2 [eV/atom-Pd]	Specific output energy E_3 [eV/atom-Pd]
D-PZ2#5	0.95 ± 0.10	1.09 ± 0.09	0.065	0.81 ± 0.05	0.94 ± 0.08	0.26 ± 0.04	2.53 ± 1.79
H-PZ1#5	0.84 ± 0.08	1.00 ± 0.09	0.075	0.77 ± 0.05	0.82 ± 0.08	0.29 ± 0.04	5.53 ± 2.10

(0.041) in this run, ℓ is assumed to be 0, because the product D_2O (H_2O) is in the gas phase in vacuum, and the third term in expression (3) obtained from the pressure difference is simply equal to $D(H)/Pd$ ($=y/2$). That is, $D(H)/Pd$ is 1.09 ± 0.09 (1.00 ± 0.09).

Although these values of $D(H)/Pd$ exceeding 1.0 appear to be unreasonable on first glance, we notice that contribution of surface adatoms

increases largely the total number of atoms adsorbed and absorbed in a nanoparticle. For example, the number of octahedral sites effective for absorption and that of surface dangling bonds effective for adsorption are 2.4×10^4 and 5.1×10^3 , respectively, in a 10-nm-diam. particle. A full charge of these sites with hydrogen would result in a loading ratio of 1.21, which accounts for the observed value of $D(H)/Pd$ mentioned above.

We have the value of the specific output energy $E_1 = 0.95 \pm 1.0$ (0.84 ± 1.0) eV/atom-Pd, and $x = 0.039$ (0.041) giving $xQ_r = 0.065$ (0.076) eV/atom-Pd. The ‘‘hydridation’’ energy $Q_{D(H)}$ is then calculated with eq.(3) to be 0.81 ± 0.05 (0.77 ± 0.05) eV/atom-D(H). These values are 2.7 (2.4) times larger than those obtained for the forced reduction sample mentioned above. Therefore, the absorption run for the oxidized sample causes not only oxygen pickup from PdO producing D_2O but also a more complex phenomenon of $D(H)$ adsorption/absorption.

In the $D(H)$ absorption runs for these oxidized samples, there also exists the new second phase when $D(H)/Pd$ decreases. The amount of reemission is similar to that for the reduction sample, and $\Delta(D(H)/Pd) \sim 0.1$. We can hardly imagine that D_2O (H_2O) molecules produced by the reductive reaction of PdO condense into liquid phase with the specific energy of 0.42 eV/atom-Pd in the first phase with

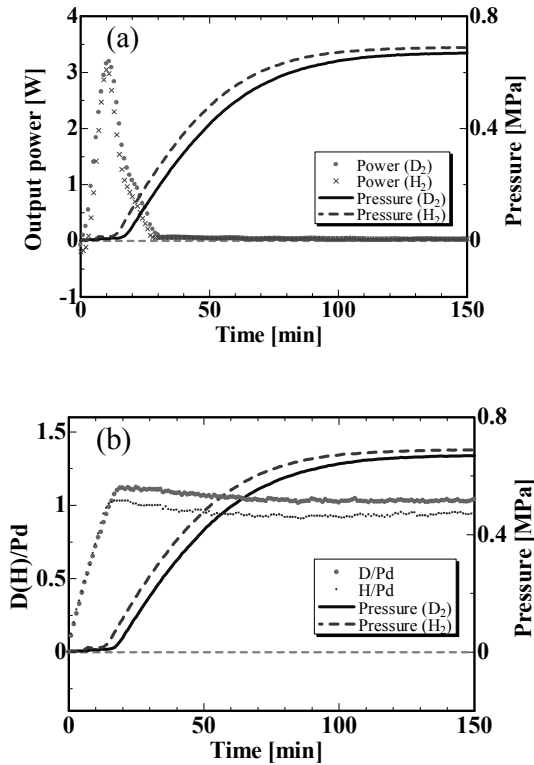


Fig. 4. (a) Evolution of heat and pressure in the reaction chamber after introduction of D_2 gas (solid) or to H_2 gas (dotted) for the Pd-ZrO₂ sample (D-PZ1#5 and H-PZ2#5), and (b) evolution of $D(H)/Pd$ and pressure in the same runs.

a low pressure. Even if we assume that the condensation is happening in the second phase, the condensation energy would amount to 0.016 (0.017) eV/atom-Pd, which is about 6 % of the observed heat value in the second phase.

Specific output energy in the third phase happens to be larger for the H-PZ1#5 run in the A₁ chamber than for the D-PZ2#5 run in the A₂ chamber, although error bars are large. The values thus obtained are summarized in Table 1 and Table 2.

5. Concluding remarks

The absorption/adsorption system has been improved to enable measurements of the time-dependent D₂(H₂) gas flow rate and the D(H) loading ratio simultaneously with the output energy. The first application to the runs with the samples after forced reduction and forced oxidation has yielded interesting results; *i.e.*, there exists the new second phase, where D(H)/Pd once

decreases, following the first phase where the most of the abnormally large output energy is produced by the very high loading. The result is the most outstanding consequence of the time-resolved measurement. There is, however, no question as to the importance of further experimental evidence required to confirm the existence of the new second phase.

Moreover, the run using the sample after forced oxidation enabled evaluation of the “hydridation” energy per a hydrogen atom when the reduction energy is known. The “hydridation” energy obtained in the present study is about 1.5 times and 4 times larger than the adsorption energy and the absorption energy, as known for bulk Pd sample, respectively.

References

- [1] Y. Sasaki, *et al.*; paper JCF10-3 in this meeting.

Charged Particle Detection during Gas Loading/Permeation Experiment with $\Delta E - E$ Si Counter Telescope

Yu TORIYABE and Jirohta KASAGI

*Research Center for Electron Photon Science, Tohoku University
Mikamine 1, Taihaku-ku, Sendai 982-0826, Japan
E-mail: toriyabe@lms.tohoku.ac.jp*

We had detected a few but high energy charged particles during D_2 gas permeation through Pd complexes samples using a YAP(Ce)/BC444 phoswich detector system. However, the number of counts is so few and energy resolution was not enough. In order to identify the high energy event we developed $\Delta E - E$ Si counter telescope system. Charged particle emissions from not only Pd complexes but also Pd/ZrO₂ nano particle samples were measured during D_2 absorption. High energy (~ 40 MeV) events were observed at the early phase of D_2 absorption. All the energy was deposited to the ΔE detector and no meaningful signal was observed for the E detector. This result means the particle was heavier than α or multi particles incident to the detector simultaneously. At present number of counts is so few that the reaction cannot be identified. Further efforts to reduce background events are required.

1. Introduction

As we have reported at recent ICCF and JCF series, a few counts but high energy charged particle signals had been observed when D_2 gas permeate through Pd samples.[1,2] In these studies, toward high reliability, we have developed the extremely low background detection system to identify such a rare event. The YAP(Ce)/BC444 phoswich detector system indicated the possibility of 30 MeV over charged particle emissions. However, the energy resolution of that system is so worse (over 20% for 5.5 MeV α particle) that the identification of the particle energy is quite hard due to the lack of statistics. Moreover, the YAP(Ce)/BC444 phoswich detector cannot separate proton and α events. Up to now, 23.8 MeV monoenergetic α particle emission which corresponds to $D + D \rightarrow {}^4\text{He}$ reaction, has not been concluded.

In this study, we therefore changed the main detector to a Si semiconductor detector (SSD) in order to identify the particle energy with high energy resolution. The SSD commercially supplied with the thickness of ~ 1 mm, is much thinner than the scintillator detector so that cosmic ray background can be reduced because the cosmic ray cannot deposit enough energy to the SSD. The most salient feature in this study is that two SSDs consist of a $\Delta E - E$ counter telescope to identify not only charged particle

energy but also particle species at the same time. This is the first time to apply $\Delta E - E$ counter telescope system to gas loading or permeation experiments. Another feature of this study is characterizing Pd nano particle sample which is recently one of the main topics in the CMNS study.

2. Detection system

Since the SSD is placed in the reducible D_2 atmosphere, a surface barrier type SSD suddenly become unstable because of the deterioration of the surface SiO₂ (p-type) layer. Although an ion implantation type SSD can avoid the reduction problem, a thin (less than 150 μm) detector for ΔE use is seldom supplied commercially. In this study, we used two different systems. The first one is single SSD system, and the second is $\Delta E - E$ system.

In the first system, the ion implanted SSD (450 mm² active area and 300 μm depletion thickness) is placed just close to the sample. The maximum detection energy is 24 MeV for α particle. In the second system, two ion implanted type SSDs (ΔE : Canberra PIPS 300 mm², 150 μm / E: ORTEC Ultra 450 mm², 300 μm) consist of a $\Delta E - E$ counter telescope. Here, the thickness of ΔE detector is so thick that α particle less than 16 MeV is stopped within the ΔE detector and particle identification cannot be performed.

Target event is, therefore, 16 MeV over α particle.

A permeation chamber equipped with the SSD is surrounded by large plastic detectors: VETO detector. If cosmic rays enter the SSD, the VETO detector would make a signal at the same time. We can reduce background events (B.G.) more by rejecting these coincidence events between the SSD and the VETO detector.

All pulse shapes were recorded by a digital storage oscilloscope and we carefully analyzed off-line data after the experiment to reject electric noises.

3. Experiment

The chamber is same as that previously reported.[1,2] The permeation experiment was carried out according to the original procedure reported in Ref. 3. Samples are Pd/ZrO₂ nano particles[4] and Pd complexes[3].

Nano particle sample was prepared at Institute for Materials Research, Tohoku University. Nano size crystalline Pd are dispersed in the ZrO₂ matrix. These particles were electrically deposited on a Cu foil at KEK with the thickness of 100 – 600 $\mu\text{g}/\text{cm}^2$. [5,6] Since D₂ gas cannot permeate through the Cu substrate, in this case, the D₂ gas do not permeate through Pd but is just absorbed into Pd.

Pd complexes which have Pd/CaO thin multi layers on the D₂ gas side, were provided from Mitsubishi Heavy Industries.[3] The opposite side is evacuated by a turbo molecular pump and thus D₂ gas permeates through the sample ($\sim 10^{-3}$ Pa under the permeation). In the previous reports, permeation rate was so low (maximum 1 ccm) that we could not replicate the original report (over 1 ccm). To increase the flow rate, we heated up the sample over 300 °C in the air just before the experiment. Organic contaminations and sulfur on the surface could be removed and, in fact, the permeation rate was improved to about 1 ccm typically.

In the chamber, the nano particle or multi-layer side was exposed to D₂ gas for about one week with the pressure of 1 atm. Temperature of the sample was kept at room temperature about 22 °C. Although higher temperature (~ 70 °C) is preferred

for high permeation rate, the electric noise (leak current) of SSD is non-linearly increased with temperature rise and it loses energy resolution.

In this study, we mainly measured in D₂ gas (1 atm) and vacuum ($\sim 10^{-6}$ Pa) conditions. The other apparatus was same as the previous reports[1,2].

4. Results

4.1. Single Detector

First, we tested nano particle samples with the single SSD system. At the first day of the D₂ runs, only two counts but high energy charged particle events whose energies were 22 and 32 MeV, were detected. Such a high energy event was also observed from the second sample. 32 MeV event was also detected at the first days of the D₂ runs. Reproducibility of the high energy charged particle detection is 2 out of 4 runs in the case of the nano particle experiments.

It should be noted that the detected energy is almost equivalent to that detected in the YAP(Ce)/BC444 phoswich detector system.[2] Furthermore, such kind of events were detected at the early phase of the D₂ absorption. This result also agrees the result of phoswich detector system.

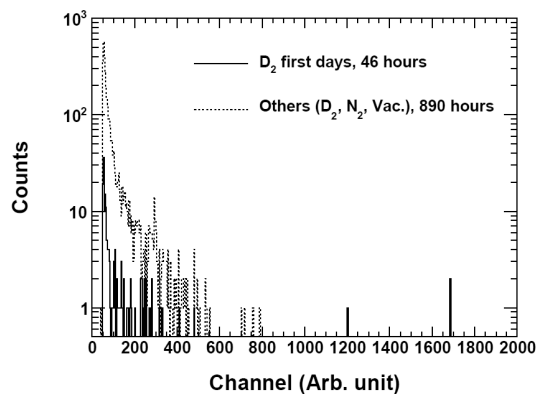


Figure 1. Number of charged particle counts for Pd/ZrO₂ nano particle experiments. Cosmic rays are rejected and anti-coincident events with VETO detectors are shown. A solid line spectrum shows total counts of the first days of D₂ runs for 2 samples from which high energy particle emitted. A dotted line spectrum shows the total of the other conditions. Duration times are 46 and 890 hours, respectively.

Figure 1 shows the total number of charged particle counts. A solid line shows a total spectrum of the first days of D₂ runs for 2 samples

from which high energy particles emitted. A dotted line shows the total of the other conditions, namely D₂ runs without first days, N₂ runs, and vacuum runs. In both cases, cosmic rays are rejected and anti-coincident events with VETO detectors are shown. The solid line spectrum has a high energy component obviously, while the dotted one does not have such event.

The count at around 1700 ch corresponds to 32 MeV. This is too high energy to be detected by the 300 μm thick SSD because 24 MeV over α particle passes through the detector and deposits less than 24 MeV energy. This result implies two possibilities; (1) the detected particle was heavier than the α particle and stopped within the depletion layer, (2) multi α particles were emitted simultaneously. To identify the reaction mechanism, we applied the $\Delta E - E$ counter telescope technique.

4.2. Counter Telescope

We tested 4 nano particle samples and 5 Pd complexes samples with $\Delta E - E$ counter telescope system. From some of them, high energy charged particles were detected. One was 20 MeV α particle from the Pd complexes. Furthermore, two unknown events were observed with both the nano particle and Pd complexes samples.

The only event identified as an α particle whose energy corresponds to 20.6 MeV was detected from the Pd complexes. It was detected 47 hours after the sample was exposed to D₂ gas. Figure 2 shows a $\Delta E - E$ two dimensional plot. Dashed lines show theoretical curves for α particles with incident angles of 0° and 30°. The ΔE and E energies were 12.1 MeV and 8.1 MeV, respectively. The event is equivalent to an α particle which incidents to the ΔE detector with the zenith angle of 25°. On the other hand, no cosmic ray or background event was plotted on the α locus until now.

The one of the unknown events is shown in Figs. 3 and 4. The event was observed with the Pd complexes 50 hours after the sample was exposed to D₂ gas. The particle deposited approximately 40 MeV to ΔE detector, and no meaningful energy to the E detector. The $\Delta E - E$ plot and pulse shapes of both detectors are shown in Figs. 3 and

4, respectively.

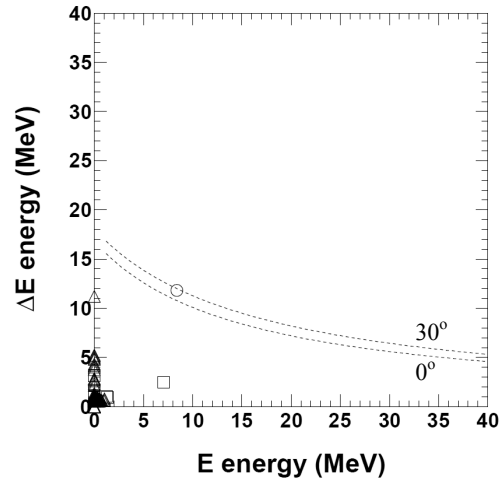


Figure 2. $\Delta E - E$ two dimensional plot. The events observed within the first 50 hours of D₂ run are plotted. Circle points show coincident events between ΔE and E detectors. Square points show the coincident events between ΔE and VETO detectors. Those correspond to cosmic ray events. The other events are plotted as triangle points. Dashed lines show theoretical curves on which α particles with incident angles of 0° and 30° should be plotted.

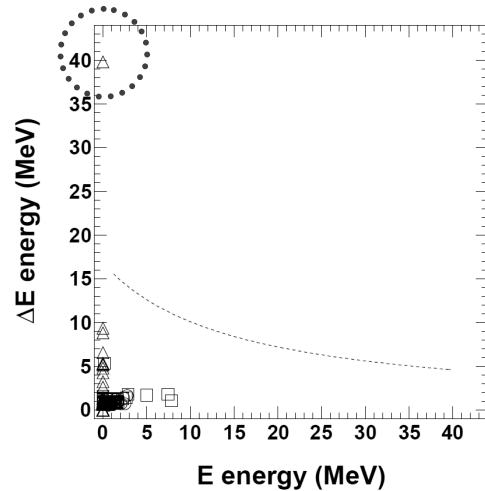


Figure 3. $\Delta E - E$ two dimensional plot of events observed during 72 hours of D₂ run. The meanings of square and triangle points are same as those in Fig. 2. A dashed line shows a theoretical curve on which α particles with incident angle of 0° should be plotted.

The pulse shape of the ΔE detector is so clear as shown in Fig. 4 that the pulse is caused by not electric noise but a charged particle. However, the pulse of the E detector is just same level of the pedestal. This result means the particle stops within the thickness of the ΔE detector and does

not path through it.

This 40 MeV level unknown event was also observed again with nano particle sample. It was detected 2.7 hours after the sample was exposed to D₂ gas and the all energy was deposited to the ΔE detector. No cosmic ray or background event was, of course, observed at such a high energy region until now as well as α particle case.

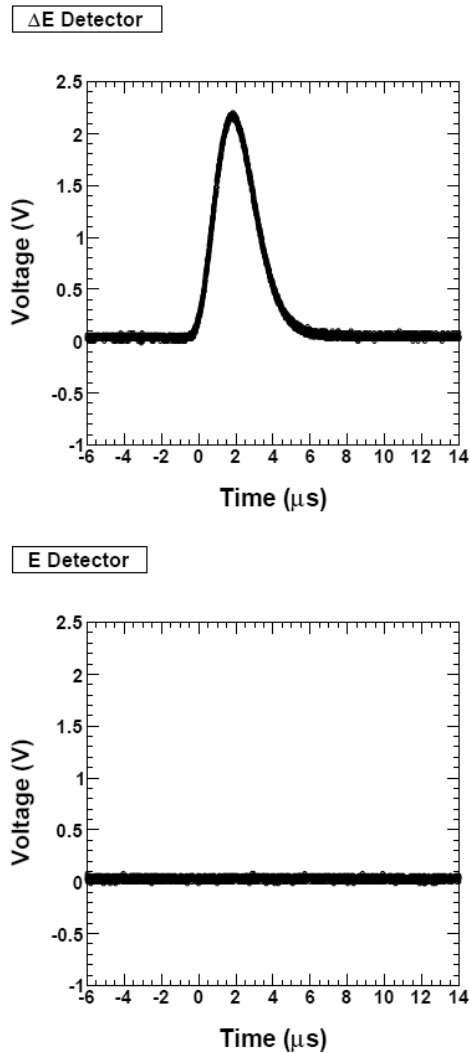


Figure 4. Pulse shapes of the ΔE and E detectors of an unknown event. The ΔE pulse corresponds to about 40 MeV. Shaping time of both detectors is 1 μs . Then time resolution of the pile up rejecter is 2.2 μs .

5. Discussions

The 40 MeV level unknown event is still questionable. The particle should be heavier than α , for example C, to deposit all energy to the ΔE detector. In general, a high energy compound nucleus should split into 2 (or 3) particles as final

state interaction. Then lighter particle has higher energy due to the kinematics. Therefore it is hard to explain high energy heavy particle emission.

If some low energy particles incident to the detector within very short time duration (2.2 μs), the output should be a pileup pulse and observed as Fig. 4. In this case, more than 3 particles should be required if the particle were α .

It should be noted that the effect of electric noise is ignorable. We all checked the pulse shapes recorded by the digital storage oscilloscope as Fig. 4. The detectors are connected to the same electronics and electric ground. Therefore not one but both detectors should make signals when the noise affects the detectors. Furthermore, all high energy events were observed at the early phase of the D₂ absorption (typically within 20 hours for nano particle, after 50 hours for Pd complexes). Here, high energy charged particle emission has never been observed during D₂ desorption process. Although H₂ runs were not carried out in this study, the high energy event has never been detected in vacuum and N₂ runs. In consequence, the high energy events are very likely to be charged particle emission from the Pd samples.

6. Conclusions

We have developed the highly reliable charged particle detection system for gas loading and permeation experiments. In this study we applied the $\Delta E - E$ technique to identify the high energy charged particle events observed in the YAP(Ce)/BC444 phoswich detector system. Then background events mainly caused by cosmic rays were reduced. The samples were Pd/ZrO₂ nano particle and Pd complexes.

High energy unknown particles have been detected from some of the samples at the early phase of the D₂ absorption. We found that 40 MeV particle was emitted and stopped within the ΔE detector with depositing no meaningful energy to the E detector. If this event were single particle event, that should be heavier than α particle. If this event were pileup event, more than 3 α particles should incident to the detector within 2.2 μs . Although the number of counts is few, we cannot conclude the particle species and reaction

mechanism.

However, the unknown events were only observed at the early phase of the D₂ absorption. High energy background has not been detected through any kind of background conditions up to now. In this view point, high energy charged particle emission would be induced by the D₂ gas absorption into the Pd samples.

At present the number of counts is so few we cannot conclude the phenomenon and conjecture a reaction mechanism. Also no meaningful correlation with the experimental condition (pressure, temperature, flow rate and so on) has been observed. Further efforts are required to reduce the background and increase foreground events.

Acknowledgements

Pd/ZrO₂ nano particle was prepared at Institute for Materials Research, Tohoku University and deposited onto the Cu foil at KEK. Pd complexes were provided from Mitsubishi Heavy Industries. Authors would like to thank Prof. Fukuhara, Prof. Yamaura, Prof. Sugai and Dr. Iwamura for their sample preparations.

This study is partially supported by Grants-in-Aid for Scientific Research from the Japan Society for the Promotion of Science.

References

1. Y. Toriyabe and J. Kasagi, *Proc. ICCF14*, (2008).
2. Y. Toriyabe and J. Kasagi, *Proc. JCF9*, 36 (2009).
3. Y. Iwamura *et al.*, *Jpn. J. Appl. Phys.*, **41**, 4642 (2002).
4. S. Yamaura *et al.*, *J. Mater. Res.*, **17**, 1329 (2002).
5. I. Sugai, *Nucl. Instr. and Meth. A*, **397**, 81 (1997)
6. I. Sugai, *Nucl. Instr. and Meth. A*, **438**, 58 (1999).

Search for Nuclear Events in Deuterium Discharge Experiment Using Multi-layered Metal Cathode

H. Sasaki*, T. Murakami, H. Ougida, S. Narita, H. Yamada

Department of Electrical Engineering and Computer Science, Iwate University

Morioka, Iwate, 020-8551, JAPAN

*t2309023@iwate-u.ac.jp

ABSTRACT

It has been shown by several researchers that loading nano-structured Pd powder or thin Pd film with deuterium results in inducing LENR in condensed matter effectively. Considering such experimental results, we have performed discharge experiment in deuterium atmosphere using multi-layered cathode which contains thin Pd membrane, and searched for nuclear phenomenon. As the results, we observed possible particle emission registered on CR-39 track detector. In addition, several sets of elements, which were considered to be newly produced during the experiment, were observed on the cathode by elemental analysis with ICP-MS and TOF-SIMS.

Keywords : Glow discharge, Multi-layered sample, Pd/Pd/Au, Selective Transmutation CR-39

1. Introduction

We have continuously performed discharge experiments in deuterium atmosphere using Pd and multi-layered Pd to investigate low energy nuclear reaction (LENR) in condensed matter. In the experiments, we have observed some symptoms which suggested the occurrence of nuclear reactions. We detected anomalous gamma radiation with energy around ~100 keV. It was supposed to be generated some short-lived radio isotopes [1,2]. Also, we found some candidates of isotopes supposed to be produced during the discharge experiment by elemental analysis of cathode surface [3,4]. Now, it is surely considered that the discharge experiment is one of the useful methods for the study of LENR.

Besides of the experimental method, sample property itself is important to induce the reaction effectively. It has been shown by several researchers that loading nano-structures sample, such as Pd powder or thin Pd film, with deuterium results in inducing LENR with high reproducibility.

Based on these research reports, in this study, we have performed discharge experiment using the multi-layered metal cathode with a structure of Pd foil coated with fine-structured Pd membrane, such as Pd/Pd/Au. Since the deuterium permeability of the Au is considered to be much smaller than that of Pd, we expect that the deuterium density can get higher

locally in the diffusion process in the sample and it may help the reaction efficiency enhance. Then we investigated the nuclear phenomenon induced. In addition, there were considerable reports that nuclear phenomenon such as generating excess heat was effectively induced by the laser irradiation to the deuterated metal sample [5,6]. So, we also attempted laser irradiation to the cathode sample and the validity for improving the efficiency for inducing nuclear reaction was evaluated.

2. Experiment

The sample was fabricated by the following method. The Pd foil with the size of 10 mm x 10 mm x 0.1 mm and the purity of 99.95% was washed by acetone for 20 minutes, and the ultrasonic cleansing was done with ultra pure water for 20 minutes. Afterwards, to make the crystallographic structure uniform, the sample was set into the evacuated cell ($\sim 10^{-3}$ Pa) and annealed for 10 hours at 900°C.

Then, it was washed by aqua regia to remove metallic impurities and the ultrasonic cleansing was done with ultra pure water for 20 minutes. Pd film was deposited to one of the surfaces of the Pd foil with the Ar beam sputtering. For Pd/Pd/Au sample, Au membrane was deposited to the other surface of the sample. The thickness of the Pd and Au membrane were ~300 nm and ~600 nm, respectively.

In this experiment, we also examined plain Pd foil to specify the properties of multi-layered sample with Pd membrane. Figure 1 shows the sample structure of Pd foil and Pd/Pd/Au sample. The charged particle emission was evaluated by comparison between the experiments.

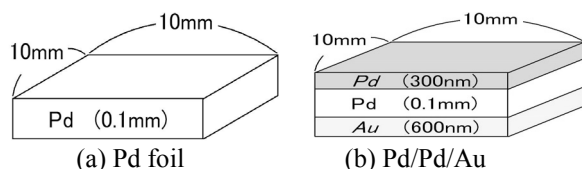


Figure 1. Sample structure.

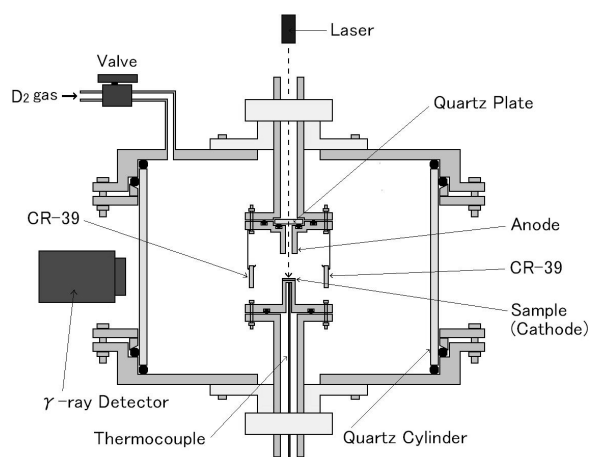


Figure 2. Discharge cell.

Table 1. Experimental conditions.

D ₂ pressure	1Torr
Volume	1300cm ³
Cathode	sample
Anode	SUS304
Gap length	10mm
Time (minute)	~180
Voltage	~500V
Current	~2mA
Laser	690nm 30mW

Table 2. Sample profile

Sample No.	Sample structure	Gas	Laser	Elemental analysis	
				TOF-SIMS	ICP-MS
09gd01	Pd	D ₂	-	-	○
09gd02	Pd	D ₂	-	○	○
09gd03	Pd	D ₂	○	-	○
09gd04	Pd	D ₂	○	○	○
09gd05N	Pd	N ₂	-	-	○
09gd06N	Pd	N ₂	-	○	-
09gd07N	Pd	N ₂	○	-	-
09gd08N	Pd	N ₂	○	○	-
09gd09	Pd/Pd/Au	D ₂	-	-	○
09gd10	Pd/Pd/Au	D ₂	-	○	○
09gd11	Pd/Pd/Au	D ₂	○	-	○
09gd12	Pd/Pd/Au	D ₂	○	○	○
09gd13N	Pd/Pd/Au	N ₂	-	○	-
09gd14N	Pd/Pd/Au	N ₂	-	-	-
09gd15N	Pd/Pd/Au	N ₂	○	-	○
09gd16N	Pd/Pd/Au	N ₂	○	○	-
09gd17N	Pd/Pd/Au	N ₂	-	-	○
09gd18B	Pd	-	-	-	-
09gd19B	Pd/Pd/Au	-	-	-	-
09gd20	Pd	N ₂	○	-	○
09gd21	Pd/Pd/Au	N ₂	○	○	○
09gd22	Pd/Pd/Au	D ₂	-	-	○
09gd23	Pd/Pd/Au	D ₂	○	-	○

Figure 2 shows the discharge cell used in this experiment. The major components of the cell are the stainless steel (SUS304) covers and quartz cylinder. The sample was placed on the cathode. The anode has quartz window so that laser irradiation to the sample is enabled. Four pieces of CR-39 (solid-state track detector) were placed surrounding the cathode in the experiment aiming at the charged particle detection. The detection area for each piece was 1 x 1 cm². In addition, the CR-39 turned inside out was placed in the cell for the reference (background). After placing the cathode sample, the cell was evacuated to 10⁻³, and deuterium gas was supplied until the pressure inside became ~1 Torr. Then, DC voltage was applied and the sample was exposed to the discharge. For multi-layered sample, Pd membrane faced on the discharge.

For investigating the effect of laser irradiation, we utilized a semiconductor laser (690 nm in wave length and ~30 mW in output power) placed outside of the discharge cell. The whole area of cathode was irradiated during the discharge. Taking account of the reflection and absorption of photons by the quartz window, the power at the cathode surface was supposed to be a few mW. Table 1 shows the summary of experimental conditions. The discharge experiment in N₂ gas atmosphere was also done to confirm the anomalous phenomena in the deuterium discharge. Moreover, for the reference in the

elemental analysis, the sample which was not exposed to the discharge was prepared as a blank sample. The sample profiles are summarized in Table 2. For the sample analyzed by both TOF-SIMS and ICP-MS, the TOF-SIMS analysis was done at first, then, the samples was immersed the acid for preparing the reagent for ICP-MS analysis.

CR-39 is a kind of plastic detector and the track pit made along the trajectory of a charged particle appears by chemical etching. The integrated signals are recorded over the experimental period. In this study, the etching process was made by 5 mol/l NaOH at 70 °C for 8 hours. After the etching, we surveyed the surface of the CR-39 with digital microscope to observe the pit tracks. The presence of the charged particles generation can be specified according to the number of tracks, and the energy of charged particles can be estimated according to the diameter with assumption of particle type.

NaI(Tl) scintillation counter was placed by the discharge cell and used to detect γ -rays emitted during the discharge as the result of a nuclear reaction. The gamma rays with the energy below 1 MeV can be detected with the counter.

If short-lived radio isotopes are produced in the experiment, they may emit γ -rays. So, the γ -ray detection was employed after stopping the discharge for 2 hours to identify such isotopes.

The elemental analysis was done by using ICP-MS and TOF-SIMS to examine the nuclear products on the surface of the cathode sample after discharge.

In ICP-MS analysis, the sample was immersed in ultra pure nitric acid and the solution was analyzed surveying the elements with mass range of 1-210. In this study, if obtained signal satisfies the following criteria, the corresponding element is considered to be possibly produced in the experiment.

- The signal intensity is larger than the lower limit of corresponding elements in the device.
- The signal intensity is larger than that of corresponding elements for the ultra pure water.
- The signal intensity is larger than that of corresponding elements for the blank sample.
- The signal intensity is larger than that of corresponding elements for the sample exposed to N_2 discharge.

While in TOF-SIMS analysis, Ga^+ was irradiated as primary ion and analyzed $40\mu m \times 40\mu m$ area on the sample surface. Comparing with the results of the reference sample (*i.e.* sample exposed to N_2 discharge), possibly newly produced elements were identified.

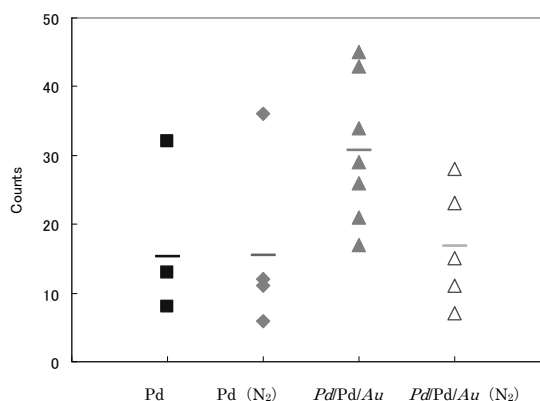
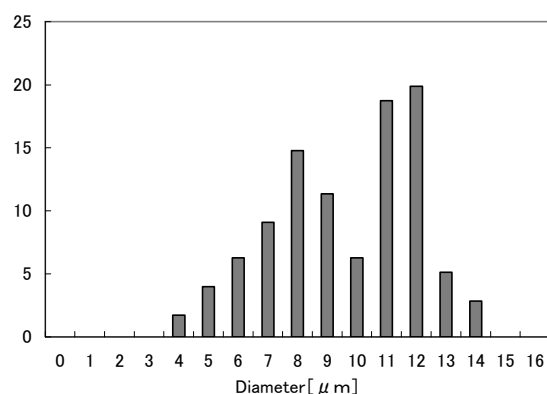
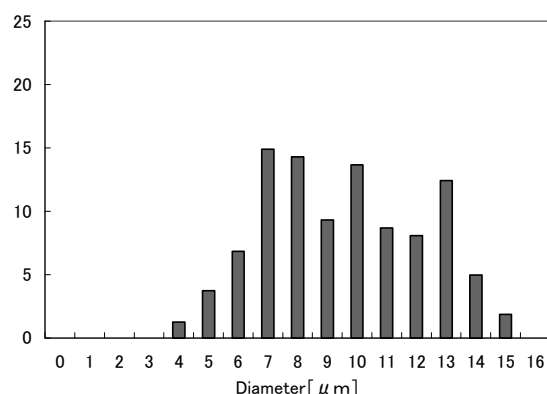


Figure 3. Number of tracks recorded on CR-39. The horizontal bars indicate the mean number for each sample set.



(a) D_2 discharge



(b) N_2 discharge

Figure 4. Track diameter of the tracks recorded on CR-39 for D_2 discharge (a) and N_2 discharge (b).

3. Results and Discussion

3.1 Charged particles measurement

Figure 3 shows the number of tracks recorded on CR-39 for each sample condition. Note that the number of tracks here is totals in four pieces CR-39 set in the cell. As mentioned above, the detection area is 1cm^2 for each CR-39. The mean numbers for each condition are 15.3 for Pd in D_2 discharge, 15.4 for Pd sample in N_2 discharge, 30.7 for Pd/Pd/Au in D_2 discharge, and 16.8 for Pd/Pd/Au in N_2 discharge. Significant number of tracks was observed for Pd/Pd/Au sample in D_2 discharge.

The averaged track density for all background CR-39 (21 pieces in total) was $4.0 \pm 3.6 /\text{cm}^2$. Then, we considered the events with the track above $8.0 /\text{cm}^2$ to have possibly charged particle origins. Figure 4 shows the diameter distribution of tracks in such events. For comparison, the total number of tracks is normalized to 100 in this figure. The peak around $11\text{-}12\ \mu\text{m}$ stands out in the distribution for D_2 discharge comparing with that for N_2 discharge. This suggests the possibility of the charged particle emission with specific energy. If charged particle emitted is assumed to be an α particle, the energy is $2\text{-}3\ \text{MeV}$ considering the diameter [7,8].

3.2 Elemental analysis

In the qualitative analysis by ICP-MS, the elements identified as possible nuclear products are summarized in Table. 2. More various kinds of elements have been detected in the Pd/Pd/Au sample rather than in plain Pd sample. These elements might be contaminated in the sample preparation process. However, these elements did not exist in the blank sample. Therefore, these might be produced by

discharge. And the multi-layered structure might induce the reaction more effectively. Moreover, ^{104}Ru , ^{106}Cd , ^{108}Cd , ^{110}Cd , and ^{114}Sn are detected with good reproducibility (2 out of 3 samples) in the run without laser irradiation. The difference in detected elements for the laser condition was not clearly seen in TOF-SIMS results.

In the γ -ray detection during the discharge, we have not observed significant signal in any experimental conditions. If the elements detected in ICP-MS or TOF-SIMS analysis were produced by a nuclear reaction, such as fission of Pd isotopes [9], it may be possible that some radioisotopes were produced as well. However, no symptom of production of such isotopes was recognized in the γ -ray measurement. It is necessary to specify the origin of elements identified with radiation measurements in further study.

4. Conclusion

We have performed the deuterium discharge experiment using Pd and multi-layered Pd/Pd/Au cathode, and investigated the nuclear phenomena. We have observed anomalous tracks in CR-39 measurement which suggested energetic charged particle emission. Especially, it was often observed in the run with Pd/Pd/Au cathode. In elemental analysis, we identified various elements for Pd/Pd/Au cathode, which were supposed to be generated during deuterium discharge. These results suggested that the multi-layered sample, especially the sample containing thin Pd membrane, can induce some nuclear reaction effectively. Irradiating the laser to the cathode is interesting idea to enhancing the efficiency for the LENR in condensed matter.

Table 3. Elements identified by ICP-MS and TOF-SIMS for each experimental condition.

Sample structure	Laser	Corresponding element	
		TOF-SIMS	ICP-MS
Pd	On	^{23}Na , ^{75}As , ^{126}Te , ^{128}Te	^{86}Sr , ^{123}Te , ^{138}La , ^{235}U
	Off	^{55}Mn , ^{112}Cd , ^{113}Cd , ^{113}In	^{55}Mn , ^{120}Te , ^{130}Te , ^{130}Ba , ^{138}La , ^{180}Ta , ^{180}W , ^{235}U
Pd/Pd/Au	On	^{115}In , ^{115}Sn , ^{142}Ce , ^{114}Nd	^{49}Ti , ^{104}Ru , ^{58}Ni , ^{60}Ni , ^{61}Ni , ^{106}Cd , ^{108}Cd , ^{110}Cd , ^{112}Sn , ^{114}Sn , ^{120}Sn , ^{120}Te , ^{130}Ba , ^{196}Hg , ^{208}Pb
	Off	–	^6Li , ^{47}Ti , ^{59}Co , ^{58}Ni , ^{60}Ni , ^{61}Ni , ^{64}Zn , ^{66}Zn , ^{67}Zn , ^{68}Zn , ^{87}Sr , ^{120}Sn , ^{120}Te , ^{124}Sn , ^{130}Te , ^{135}Ba , ^{138}Ba , ^{190}Pt , ^{208}Pb

Although the effect was not clear in the current results, we will keep investigating systematically in the future study.

References

1. A. Arapi et al., Jpn. J. Appl. Phys. (2002) L1181.
2. S. Narita et al., Proc. of JCF5 (2004) 14.
3. S. Narita et al., Proc. of ICCF12 (2006) 188.
4. S. Narita et al., Proc. of JCF6 (2005) 43.
5. D. Letts, Proc. of ICCF10 (2006) 159.
6. V. Violante et al., Proc. of ICCF12 (2006) 55.
7. A. Roussetski et al., Proc. of ICCF11 (2006) 274.
8. S. Narita et al., Proc. of JCF8 (2008) 5.
9. A. Takahashi et al., Jpn. J. Appl. Phys., 40 (2001) 7031.

Anomalous tracks recorded on CR39 in deuterium desorption experiment

S. Narita*, H. Yamada, H. Nagai, T. Takahashi, A. Taguchi, M. Sasaki, M. Kawashima, R. Moriya

Department of Electrical Engineering and Computer Science, Iwate University

Morioka, Iwate, 020-8551, JAPAN

* narita@iwate-u.ac.jp

ABSTRACT

The unique properties of the multi-layered sample in deuterium diffusion process are supposed to be concerned with a trigger condition for low energy nuclear reaction in condensed matter. We have examined multi-layered samples with the structure of the Pd foil coated with the Pd membrane and investigated their behavior for deuterium diffusion process followed by a nuclear reaction. In several experiments, numerous tracks were recorded on the CR39 detectors and the track diameter distributions were apparently different from background ones. This might suggest that the low energy nuclear reaction in condensed matter has been induced in the deuterium desorption process.

Keywords: multi-layered sample, Pd, Pd membrane, deuterium, CR39

1. Introduction

It has been considered that unique properties of the multi-layered sample in deuterium diffusion process are concerned with the trigger condition for low energy nuclear reaction (LENR) in condensed matter [1-3], and the systematic study for understanding the deuterium dynamics in such samples can provide us useful information on the mechanism of the reaction.

We have examined various types of multi-layered samples in relation to the behavior in deuterium desorption process followed by nuclear phenomena. We found that multi-layered structure may improve deuterium loading ratio, D/Pd. In deuterium desorption process, we observed explosive deuterium desorption simultaneously with anomalous heat evolution which was hardly explained by a chemical reaction [4], for some types of multi-layered samples. Then, it has been inferred that the instantaneous deuterium diffusion is caused by some nuclear effects which might be concerned with the heat evolution. Moreover, significant number of tracks was sometimes recorded on the CR39, which can be an evidence of charged particle emission from the sample.

It is known that the multi-layered structure of the crystalline bulk Pd and the non-crystalline Pd membrane has a unique property in hydrogen absorption and desorption [5]. Then, we prepared the sample with the Pd foil coated with the Pd membrane

and tested. We found that such samples promotes the deuterium desorption and anomalous tracks have been observed on the CR39 detector [6]. Now it is expected to induce LENR in condensed matter effectively with such samples.

In this study, we have performed the deuterium absorption/desorption test with various types of the Pd coated multi-layered sample, and characterized the sample properties systematically, searching for occurrence of nuclear phenomena such as particle emission and heat evolution.

2. Experiment

We prepared multi-layered samples which contain the Pd membrane such as *Pd/Pd*, *Pd/Pd/Au*, and *Pd/CaO/Pd/Au*. (Note that the material expressed with the *italic* font indicates the membrane layer). These samples were fabricated by depositing Au, CaO, and Pd layers by Ar ion beam sputtering onto the surface of the Pd foil substrate. The substrate Pd has the size of 10 mm x 10 mm x 0.3 mm. It was washed by acetone and aqua regia, before depositing the membrane. The typical thickness of Pd, CaO, and Au membranes was ~1000 nm, ~10 nm, and ~500 nm, respectively. For loading deuterium to the sample, the fabricated multi-layered sample was exposed to 5 atm deuterium gases for 23 hours. The weight of the sample was measured before and after loading, and the loading ratio (D/Pd) was calculated from the weight difference.

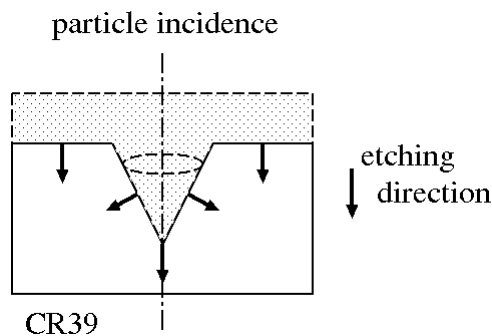


Fig. 1. Etch pit formation in CR39 by chemical etching.

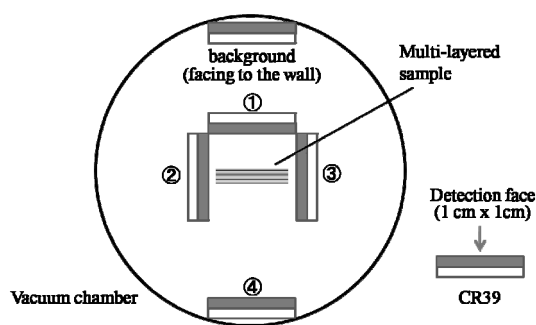


Fig. 2. CR39 layouts in the vacuum chamber in desorption experiment.

The desorbing test was performed as follows; the D loaded sample was put into the chamber which can be highly evacuated by a TMP ($\sim 10^{-4}$ Pa). The pressure in the chamber and the sample temperature were monitored continuously for ~ 24 hours. The ionization gauge and a thermo-couple was used for their measurements, respectively. In our previous experiment, the sample was heated by supplying electric current to stimulate the deuterium diffusion in the sample, while in this study, we did not make temperature control for the sample since the Pd membrane itself is expected to enhance the gas out-diffusion from the sample.

The CR39 track detector (Fukuvi Chemical Industry) was used for detecting charged particles which can be emitted during the desorption test. The detector is made of diethyleneglycol bis allylcarbonate with thickness of ~ 0.9 mm. When a charged particle crosses the CR39, a part of the energy of the particle is deposited. As the result, chemical composition of the materials is changed along the particle trajectory. If we make etching process for the detector in the chemical reagent, a track pit appears because the etching rate for the region which contains the track is larger than other

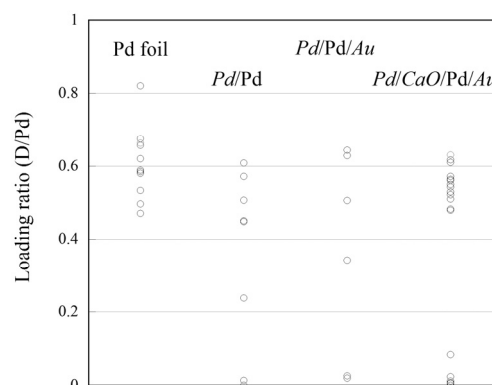


Fig. 3. D/Pd for various multi-layered samples.

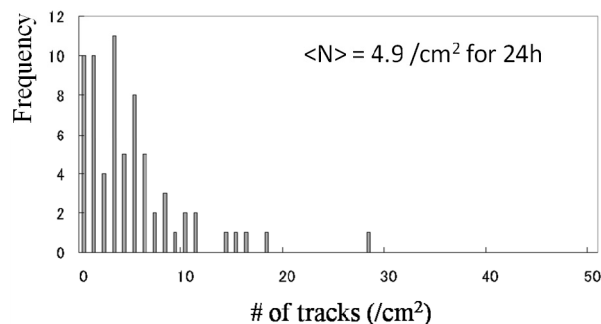


Fig. 4. Number of tracks on CR39 for background samples.

Sample	Number of runs with anomalously abundant tracks (total runs)
<i>Pd/Pd</i>	0 (4)
<i>Pd/Pd/Au</i>	1 (4)
<i>Pd/CaO/Pd/Au</i>	18 (21)

Table. 1. Number of runs with tracks more abundant than $30/\text{cm}^2$ on CR39.

regions. A schematic view of the track formation process on the CR39 is shown in Fig. 1. The etching conditions for this study were 5 N NaOH solutions at 70°C for 8 hours. The 4 pieces of CR39 were placed surrounding the multi-layered sample to detect foreground events. A piece of the CR39 was also set in the chamber facing the chamber wall for background evaluation. The layout of the CR39 in the chamber is shown in Fig. 2.

3. Results and Discussion

The D/Pd for each sample type is shown in Fig.3. No clear dependency on the sample structure and the material is found. Note that the D/Pd for the sample with the Pd membrane is sometimes quite low. Similar result was observed in our previous study [6]. It was supposed that loaded gas was desorbed before weighing the sample due to high activity in diffusion in the Pd membrane and recombination on the surface of the Pd membrane.

In the temperature measurement, we have not seen any anomalous heat evolution during the desorption experiment for any sample type in this study. The anomalous heat evolution observed in our previous study usually occurred simultaneously with explosive gas out-diffusion, while in the present study no such behavior in the pressure measurement was seen either. As mentioned above, the Pd membrane can enhance the gas diffusion, and it was possible that the most of the loaded gas was desorbed at the initial stage of the experiment before registering the sample temperature and the chamber pressure.

Figure 4 shows number of tracks recorded on the CR39 for the background samples. The averaged number of tracks and the standard deviation of this distribution were found to be 4.9 /cm² and 5.0 /cm² respectively. Considering these numbers, we took the events with tracks more abundant than 30 /cm² as anomalous ones. The number of such runs for each sample type is shown in Table. 1. The anomalous events were frequently observed for the Pd/CaO/Pd/Au sample. Figure 5 shows the number of tracks recorded on a CR39 and the mean diameter of the tracks for the foreground and the background events in the runs with Pd/CaO/Pd/Au. The distribution of mean diameters of the tracks for foreground events appears to have a peak around 6-8 mm, while the background ones are randomly distributed. This result may be an indication of detection of charged particles with specific energy.

Then, in order to verify existence of the anomalous tracks only in foreground events, we performed additional experiments with the same condition as that in the desorption test but without setting the multi-layered sample. (This is called "blank runs"). In this case, tracks recorded on 4 foreground pieces and 1 background piece are all regarded as ones due to meaningless events, and only for reference. Figure 6 shows the number of tracks recorded on the CR39 for blank runs. Although the number of blank runs is still small, large number of tracks were sometimes observed. The relationship between the number of tracks on and the mean diameter of the tracks for the foreground

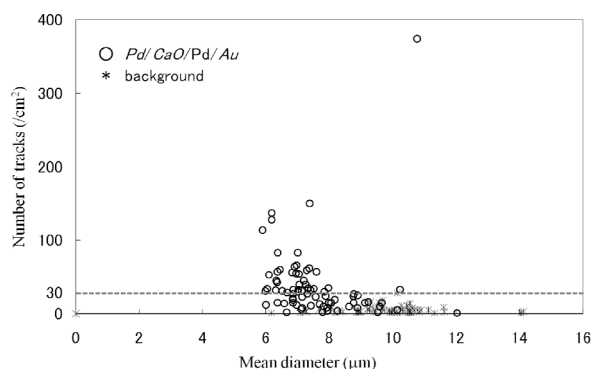


Fig. 5. Number of tracks vs. mean diameter in comparison with foreground events (Pd/CaO/Pd/Au) with background ones.

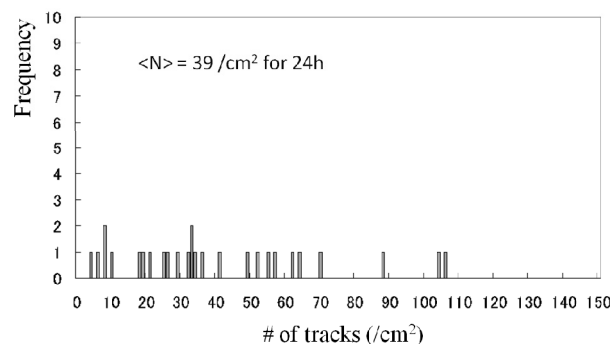


Fig. 6. Number of tracks for the samples in blank experiment.

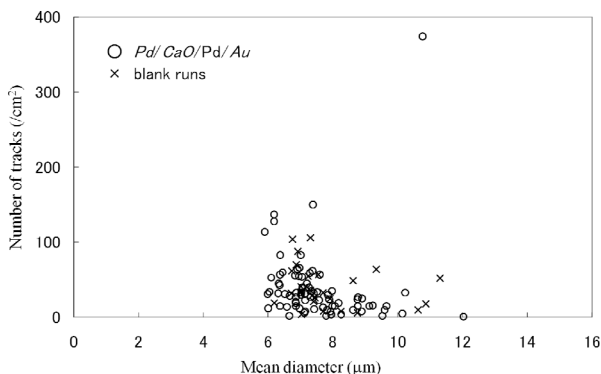


Fig. 7. Number of tracks vs. mean diameter comparing foreground events (Pd/CaO/Pd/Au) with blank ones.

(Pd/CaO/Pd/Au) CR39 are shown in Fig. 7 in comparison with ones for blank runs. It is hard to distinguish the foreground events from blank ones for now. Further study for background events is still needed to verify the charged particle detection in the foreground samples.

Now we discuss what are the tracks recorded in the background or the blank runs. There are several

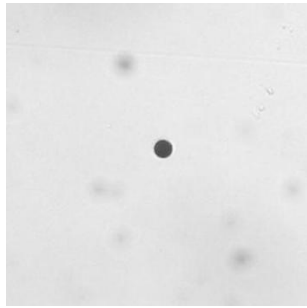


Fig. 8. Typical images of track recorded in the blank run.

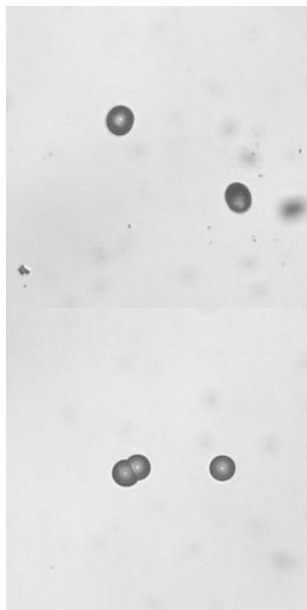


Fig. 9. Track images of the foreground sample (*Pd/CaO/Pd/Au*).

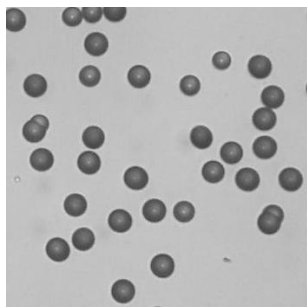


Fig. 10. Track images recorded by alpha particles using ^{241}Am source.

possible sources to form traces. In principle, incidence of environmental radiation can make tracks on the CR39. Alpha particles from Rn ($E \sim 2$ MeV) in the air are one of the most possible sources.

Assuming the radioactivity of the environmental Rn is ~ 100 Bq/m³ and considering the stopping length of a 2 MeV alpha particle to be about 10 mm, the number of tracks formed by such particles on the CR39 is estimated to be less than 10 /cm² in the case of exposure to air for 24 hours. The CR39 has a protective film on the surface and we remove it just before the experiment. After the experiment, the CR39 is etched immediately. In addition, most part of our experiment is performed in the highly evacuated chamber. Therefore the effect by such radiation should be very little under our experimental condition.

Other possible sources for background tracks are bulk and surface defect [7]. The defect in constituent molecules of CR39 can appear as a track pit as a result of etching. This defect should exist in the original lot. Although we do not know how much it affects the track forming quantitatively, the effect is thought to be definitely small. Surface defect created mechanically during the experiment may cause the background track. This effect depends on the treatment of CR39 in our experiment and appears systematically. So, it cannot explain that the number of tracks is larger for the foreground sample. It is not still understood that the distribution of the number of tracks for the background and the blank runs are absolutely different. As shown in Fig. 6, the numbers for the blank samples are apparently larger. The effects mentioned above cannot explain this result. We still need further study to understand the origins of marked number of tracks recorded on the blank and background batches.

Besides the statistical analysis, precise observation of the track shape may give us the information to identify charged track species. Figure 8 shows one of the typical images of the tracks recorded on blank batch. While, Fig. 9 shows track images recorded in the experiment with the *Pd/CaO/Pd/Au* sample. Note that 374 /cm² tracks were found in this batch. The shape of the foreground tracks is obviously different from background ones. Also, we often observed the overlaying tracks (“double track”) in foreground runs as seen in the bottom of Fig. 9. Figure 10 shows track images for alpha particles by a sealed ^{241}Am source. The shape of the images is similar to that in Fig. 9. The gray-colored portion in each etch pit represents a rounded top of the etch cone, and its existence almost at the center in each pit indicates that the energetic particle was incident on the CR39 plate almost perpendicularly, as shown in Fig. 1. We should keep surveying all of tracks to verify the characteristic of the shape.

4. Summary

We have investigated the behavior of deuterium absorption and desorption followed by possible nuclear phenomena for the multi-layered sample coated with the Pd membrane on the surface. In the desorption test, the CR39 was utilized for detecting charged particle emission as the evidence of occurrence of the nuclear events. We observed numerous tracks on the CR39, especially in the runs using the *Pd/CaO/Pd/Au* sample, and the image of the tracks is similar to ones created by alpha particles from the ^{241}Am source. Although the background evaluation should be done more carefully, this result may indicate that some kind of nuclear reactions has been induced in deuterium desorption process. We will keep studying the track formation process including the background behavior to find out the origin of anomalous tracks on the CR39. In parallel, we now think about using additional device such as Si-SSD which can provide time-dependent measurement of emitted particle number and energy. These information are indeed necessary to clarify the reaction process in the further study.

References

1. E. Yamaguchi *et al.*, Jpn. J. Appl. Phys. 29 (1990) L666.
2. Y. Iwamura *et al.*, Jpn. J. Appl. Phys. 41 (2002) 4642.
3. A.G. Lipson *et al.*, Proc. of ICCF12 (2006) 293.
4. S. Narita *et al.*, Proc. of JCF8 (2008) 5.
5. H. Tamura (ed), "Suiso-kyuzou-goukin" (1998) (in Japanese)
6. S. Narita *et al.*, Proc. of JCF9 (2009) 11.
7. R. Mishra *et al.*, Radiation Meas. 40 (2005) 325.

Detection of Energetic Charged Particle from Thin Ni Cathode in Shortened $\text{Li}_2\text{SO}_4/\text{H}_2\text{O}$ Electrolysis Using Track Detector CR-39

H. Yamada, S. Narita, Y. Oshima, H. Yamagishi, H. Yokokawa and H. Nanao*

Department of Electrical and Electronic Engineering, Iwate University, Ueda 4-3-5, Morioka, 020-8551 Japan yamadahi@iwate-u.ac.jp

* Department of Chemical Engineering, Iwate University, Ueda 4-3-5, Morioka, 020-8551 Japan

Abstract: Light water electrolysis of Li_2SO_4 solution for 20 min was performed using CR-39 track detector and the $5\mu\text{m}$ thickness Ni cathode, which forms the inner bottom of the test cell. The CR-39 track detector was positioned just under the Ni cathode as being closely contacted with the Ni film. This construction can minimize the energy loss of charged particle penetrating through the thin Ni cathode and maximize the detecting efficiency of emitting particle. Nine series of electrolysis experiments and nine series of blank experiments were carried out. Comparing with the results for blank experiments, a marked increasing number of etch pit has been observed on the CR-39 chips after the electrolysis. The emitting particles seem to have a constant energy of ~ 3 MeV. The result strongly indicates the low energy nuclear reaction for this hydrogen system.

Keywords: Light water electrolysis, CR-39, Thin Ni cathode, Low energy nuclear reaction

1. Introduction

We have been studied low energy nuclear reaction (LENR) for hydrogen system using TOF-SIMS, where the gas permeation and electrolysis methods were employed¹⁻³⁾. The results obtained suggested that newly elements have been produced for the hydrogen systems as well as the case for deuterium system. However, each experiment time required in these studies was as long as \sim two weeks on average. Besides, the masses of newly produced elements Fe, Cr, Cu, Ag, Ba and Pb are relatively large so that many plausible reaction processes can be presented. To the contrary, the number of the reaction producing low mass particles such as proton, neutron and α particle is limited to be few. Thus, the experiments providing such particles for hydrogen system are important to construct the LENR model.

On the other side, the plastic track detector has become a popular method to measure charged particle emissions in LENR studies especially in electrolysis experiments⁴⁻¹⁴⁾. In these studies, the evidence of the reaction is in the form of nuclear damage trails made visible by the etching of the plastic chips. The sophisticated experimental techniques⁴⁻¹⁴⁾ have been developed by

Lipson et al., Roussetski et al. and Oriani et al. to have shown the generation of nuclear particles during electrolysis. However, there still exist technical complexities in using plastic track detector chip in electrolysis experiment, which will lead presentation of unreliable data.

The primary purpose of this study is to establish a simple technique repeatedly producing new convincing evidence that a nuclear reaction as LENR could accompany light water electrolysis.

The present technique is simple but capable of detecting energetic charged particles produced on the cathode during electrolysis with high efficiency. In the present investigation, the CR-39 chip of the plastic track detector is positioned just under the thin Ni film cathode as that a thin Ni film is interpreted between the electrolyte and the CR-39 chip. This construction avoids chemical attack on the chip by ions generated by the electrochemical reactions on the Ni cathode. The simplicity of this construction has led us to take experimental time short to the order of ten min and to minimize the noise particles from environment during the electrolysis.

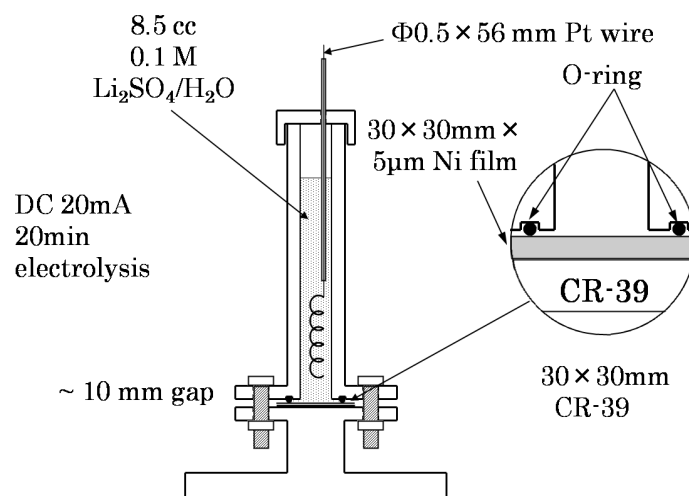


Fig. 1 The vertical cross section of the test cell.

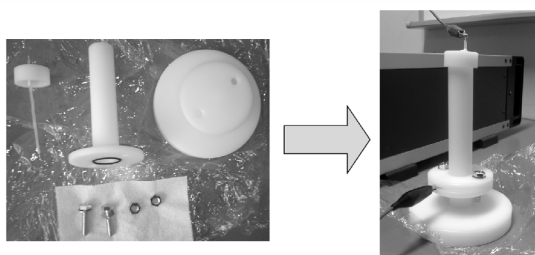


Fig. 2 The view of the test cell, (left) its components and (right) assembled

2. Experimental

Electrolysis was carried out in a small plastic cell shown schematically in Fig. 1. It consists of a vertical plastic cylinder with 105 mm long and 10 mm inside diameter, a plastic cap, a lower portion of plastic base and electrodes. The left side and right side of Fig. 2 display the components of the cell and the cell assembled, respectively. The top end of cylindrical portion of the cell assembled is covered by a plastic cap with roughly contact, which permits the escape of the gas produced by electrolysis. The 5 μ m thickness Ni film forms the inner bottom of the test cell and serves as cathode: the diameter of the cathode is 10 mm. The anode was ϕ 0.5 mm Pt wire and the upper portion of it is sheathed by heat-shrinkable PTFE tube. The anode is the lower end 56mm length of the Pt

wire and forms a crude spiral of $\phi \sim 5$ mm and 27 mm long. The anode spiral plane is parallel to the plane Ni film cathode with gap distance of ~ 10 mm.

The track detector CR-39 chip 30 \times 30 mm in size is cut from a sheet, produced by Fukuvi Chemical Industry Co., just before the electrolysis experiments. The chips are carefully manipulated with tweezers. The center of the front surface of which contacts to the Ni film is scratched to form a 10 \times 10 mm square lines, followed by removing the manufacture-supplied blue protective film. The CR-39 chip is mounted in the electrolysis cell immediately after removing the protective film. The scratched surface is referred to as the front surface upon which Ni film is overlaid. The rear surface of Ni film cathode area is closely contacted with the surface of the inside area bounded by scratched 10 \times 10 mm square line on the front of CR-39 chip. Both the Ni film and CR-39 chip are clamped together on the lower base portion and sealed by an O-ring. This construction of the cell can minimize the energy loss of charged particle, which is produced on the surface of the thin Ni film and penetrate through it in the electrolysis process, and can maximize the efficiency of the detecting particle.

The electrolyte solution for the light water

electrolysis is 0.1 M $\text{Li}_2\text{SO}_4/\text{H}_2\text{O}$ with an initial composition of 1.345 g Li_2SO_4 per 122 ml H_2O . The volume of electrolyte solution in the test cell is 8.5 ml.

After the lower portion of the cell is assembled to form a small vessel, the 8.5 ml electrolyte solution is poured into the cell. Then, it is followed by putting the cap, which has the anode, on the upper portion. The electrolysis was conducted for ~20 min by constant DC ~20 mA and ~6 V application. The current for the electrolysis was supplied by a constant-current power supply and no water was added during the electrolysis. The short detecting time of 20 min have an advantage of minimizing the number of tracks produced by particles from the environment. After those tests the cell assembly was immediately disassembled to remove the CR-39 and Ni film used.

The electrolysis experiments were always immediately followed by the blank experiments, where CR-39 chips were mounted in the newly assembled cell fitted with unused Ni electrode and electrolyte in the absence of electrolysis. Furthermore, two kinds of control experiment were conducted. The CR-39 chips used in blank and control experiments were carefully handled in exactly the same way as those used in the electrolysis experiments. For instance, the exposure time of CR-39 for the blank and control experiments was same length of 20 min as that for the electrolysis experiment as well as detector chips and Ni films remained in the cell without ongoing electrolysis.

All the CR-39 chips used in this study were cut from the same CR-39 sheet. The CR-39 were etched in 5 M NaOH for 8h at 70 °C immediately after each experiment. The measurements of etch pits are carried out using a digital microscope system (KEYENCE VHX-200), consisting of an optical microscope with a camera and a PC. The small area 0.79 cm² of Ni film cathode and corresponding 10×10 mm measurement area of CR-39 chip enable us to count the exact number of etch pits.

3. Result

It is necessary to distinguish nuclear pits produced during electrolysis from artifacts caused by manufacturing defects in the detector plastic. Therefore, an energetic α beam with the order of MeV was used to identify the nuclear pits. The appearance of the nuclear pits was found to have much darker wide rim in the microscope because of relatively deeper bottom compared with its diameter. Fig.3 shows the typical photomicrograph of pits obtained after the electrolysis experiment. Two pits seen in the photomicrograph are thought to have the origin of tracks produced by some nuclear particles.

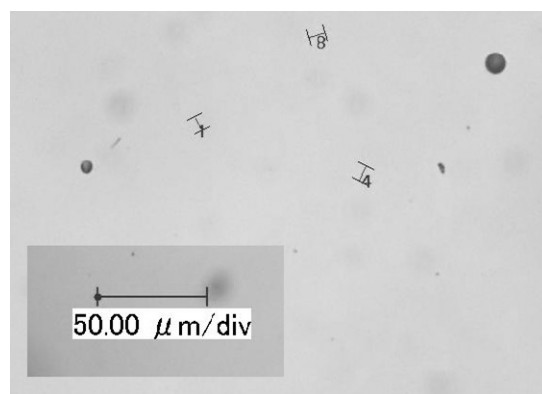


Fig. 3 Photomicrograph of a surface of the CR-39 chip employed as a detector during electrolysis.

To the contrary, the other artifacts pits usually give narrow darker rim because of its shallow form. Since there still exist pits hard to be discriminated between nuclear and artifacts pits, features whose identity remains ambiguous were avoided from counting.

The pits were counted only within the inside area bounded by scratched 10×10 mm square line on the front surface of CR-39 chip. The number of pits in the inside area was compared with that found for blank experiments. The number of etch pits for chips exposed during electrolysis was observed to be on average greater than for those in blank experiments. The number of etch pit for blank experiment was relatively

constant, ranging 1-4. In 7 of the 8 electrolysis experiment the numbers of nuclear tracks formed during electrolysis was larger than that in the blanks. This result is compiled into Fig. 4.

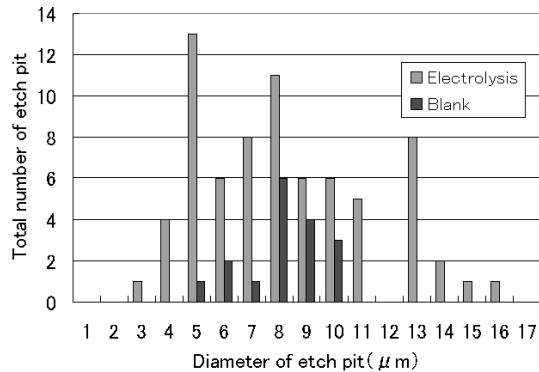


Fig. 4 Compiled distribution of diameter of etch pit for total 8 of electrolysis experiments and the corresponding 8 blank experiments.

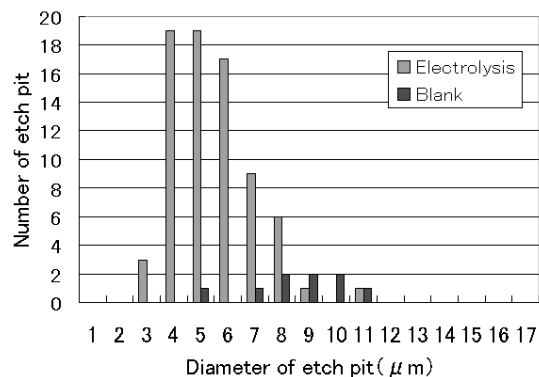


Fig. 5 Distribution of diameter of etch pit for an electrolysis experiment and the corresponding blank experiment.

It should be noticed that the distribution future of diameter of etch pit for electrolysis experiment is clearly different from that for blank experiment. The former has a semi-Boltzmann distribution with a peak at $5\mu\text{m}$ and the latter a semi-Gaussian with a peak at $8\mu\text{m}$. Fig. 5 provides considerable large number of tracks on single CR-39 chip produced during the electrolysis and again represents clearly the aforementioned two types of distribution future. However, the temperature of NaOH solution was not

constant during the etching time of the chips employed for Fig. 5.

The blank experiments are considered to give some nuclear tracks already be present in the CR-39 sheet as received from supplier, as well as those produced during the entire experimental process by nuclear source such as radon in the environment including air, the electrolyte, etching solution. In addition, the pits counted for blank experiments in Fig. 4 and 5 could originate from manufacturing defects, as mentioned above. Some part of these pits will unavoidably have similar form to that of nuclear pits.

By carefully reviewing all the experimental results, the distribution future for electrolysis experiment shown in Fig. 4 and 5 cannot due to ordinary radioactive particles from the environment and artifacts. In other words, it is demonstrated that the increasing number of track on the CR-39 chips can be attributed to a nuclear process occurring at the Ni film electrode in the operating electrolysis cell.

The electrolyte temperature was constant $\sim 21^\circ\text{C}$ during the electrolysis. This means that the input power of 0.12 W did not increase the electrolyte temperature and that the increase in number of pits in this study has no relation to temperature of the electrolyte.

Control experiments that looked for the defects produced on CR-39 chips during electrolysis were two kinds. The first one was performed by flowing dc current of 20mA through only the Ni film to look for the effect of dc current on the number of etch pits. The current is found to have no effect on the producing tracks. The second one was carried out by mechanical stirring of the electrolyte to check the possibility that the stirring will cause a vibration of the Ni film and the Ni vibration might make defects on the CR-39 chips. It was found that such mechanical stirring of electrolyte does not increase the number of etch pit at all.

Hence it can be concluded that the present simple technique has yielded evidence that a low energy nuclear reaction has been generated in the course of electrolysis.

4. Discussion

The number of etch pit decreasing with diameter of it is seen in Fig. 4 and 5. This semi-Boltzmann distribution with a peak at $5\mu\text{m}$ would one to argue producing protons with $\sim 3\text{ MeV}$ ⁹⁾. The decreasing characteristic looks like that all the particles have a constant energy of $\sim 3\text{ MeV}$ at emission site and that some part of the particles decrease their energy by collision with Ni atoms with passing through the Ni film before reaching the surface of CR-39. This energy decay process seems to be appeared as the semi-Boltzmann distribution in Fig. 4 and 5. Lipson et al.⁴⁻⁶⁾ and Roussetski et al.⁹⁾ have reported similar characteristic for hydrogen systems. They attributed the etch pits seen in their studies to some particle with energy of the order of MeV. Furthermore, Lipson et al.^{4, 6, 7)} and Roussetski et al.⁹⁾ have reported the similar characteristic for deuteride systems, where the protons were thought to be as the emission particles with energy $\sim 3\text{ MeV}$ ^{4, 6)}.

Of particular interest is the fact that the distribution feature shown in Fig 4 and 5 is the commonly seen between hydrogen and deuteride systems. It looks as though the protons with $\sim 3\text{ MeV}$ play the important role in the LENR in both systems. In other words, same basic nuclear reaction process would exist in the LENR of both systems.

The well known d-d reaction which produces protons with $\sim 3\text{ MeV}$ is



When this reaction takes place for hydrogen system, there must exist following unknown and generally unacceptable process. In the first stage of the reaction, a deuteron is produced from two protons during electrolysis at room temperature. Next, the d-d reaction, producing the proton with energy of 3 MeV , takes place in the region of the low energy. The first stage of reaction would be similar to that occurring in stars such as the sun except for extremely high energy reactions in stars. However, there remains a possibility that the small amount of deuterium included in the light water plays an important role in the LENR.

5. Conclusion

A simple experimental technique using thin Ni film cathode and track detector CR-39 for nuclear reaction in light water electrolysis is present. The experiments using the technique yield successfully new result on the LENR for $\text{Li}_2\text{SO}_4/\text{H}_2\text{O}$ electrolysis. Most of the electrolysis experiments showed remarkable increasing number of etch pits up to $26/\text{cm}^2$. The result suggests a LENR occurring on the thin Ni cathode during the 20 min electrolysis, as well as the LENR reported already in deuteride system. The detection method using SSD instead for CR-39 chip is expected to give more precise energy value of the emitting particles in the light water electrolysis.

Acknowledgment

The authors acknowledge the support of TEET (The Thermal and Electric Energy Technology Foundation).

References

- 1) H. Yamada et al., Proc. 5th Meeting of Japan CF Research Society, p. 69 (2003)
- 2) H. Yamada et al., Proc. 9th Int. Conf. Cold Fusion, p. 420 (2002)
- 3) H. Yamada et al., Proc. 10th Int. Conf. Cold Fusion, p. 455 (2003)
- 4) A. G. Lipson et al., Proc. 9th Int. Conf. Cold Fusion, p. 208 (2002)
- 5) A. G. Lipson et al., Proc. 9th Int. Conf. Cold Fusion, p. 218 (2002)
- 6) A. G. Lipson et al., Proc. 10th Int. Conf. Cold Fusion, p. 539 (2003)
- 7) A. G. Lipson et al., Proc. 11th Int. Conf. Cold Fusion, p. 324 (2004)
- 8) A. S. Roussetski et al., Proc. 10th Int. Conf. Cold Fusion, p. 559 (2003)
- 9) A. S. Roussetski et al., Proc. 11th Int. Conf. Cold Fusion, p. 274 (2004)
- 10) R. A. Oriani et al., Jpn. J. Appl. Phys., Vol. 41, p. 6180 (2002)
- 11) R. A. Oriani et al., Proc. 10th Int. Conf. Cold Fusion, p. 567 (2003)
- 12) R. A. Oriani et al., Proc. 10th Int. Conf. Cold Fusion, p. 577 (2003)
- 13) R. A. Oriani et al., Proc. 11th Int. Conf. Cold Fusion, p. 281 (2004)
- 14) R. A. Oriani et al., Proc. 11th Int. Conf. Cold Fusion, p. 295 (2004)

Role of PdO Surface-Coating of Pd Nano-Particle for D(H) Charging and Cluster Fusion

A.Takahashi^{2*}, A. Kitamura¹, Y. Sasaki¹, Y. Miyoshi¹, A. Taniike¹, R. Seto² and Y. Fujita²

¹ Kobe University, ² Technova Inc.

*akito@sutv.zaq.ne.jp

Abstract: The PdO-coated layer of Pd-nano-particle may arrange fractal nano-dips on its surface when D(H)-gas is charged and de-oxidation molecules (D₂O or H₂O) are released. Fractal sub-nano-dips may make local deep adsorption potentials, through which rapid penetration of D-atoms (ions) into deeper Pd-local lattice (Bloch potential) O-sites of nano-particle may be induced, to realize full or over-full D(H) loaded state ($x > 1.0$) of PdD_x in a short time of the Phase-I process. Formation of D-clusters, such as 4D/TSC may be enhanced at surface nano-dips, as well as by quasi-free D-motion under non-linear oscillation in collective mesoscopic potential well.

Keywords: Pd nano-particle, D-gas loading, PdO surface layer, sub-nano-dip, 4D cluster, rapid full loading, non-linear oscillation

1. Introduction

We of the Kobe Group have reported newer results on anomalous D(H) absorption and excess heat by nano-Pd/Metal-Oxide dispersed samples by separate reports in this JCF10 meeting^{1,2}.

Two new findings were reported there: 1) Forced oxidation of used Pd/ZrO₂ samples showed remarkable recovery effects on D(H)-loading ratios and heat release rates in the Phase-I interval of D(H)-charging experiments. 2) By time-resolved (time-dependent) measurements of D(H)-loading ratios, we have found the “new second phase” after the Phase-I. At the end of Phase-I, D(H)/Pd ratios became 1.1-1.2 with integrated specific heat-energy 0.83 to 2.0 eV/atom-Pd. At the end of new second phase (Phase-II) with slower change of loading ratios, additional weak heat levels were recorded. The third phase (Phase-III) was redefined for the time-period after D(H)/Pd ratios were saturated in Phase-II. We discuss on what kind of underlying physics is there, by proposing a phenomenological model which may relates to the TSC theory³⁻⁵.

Reduction process of PdO in samples under D(H) charging is first discussed briefly in this paper. Secondly and mainly, the role of PdO surface coating of Pd nano-particle is discussed using a phenomenological (speculative) model on what happens under D(H) charging to induce the D-cluster formation and 4D/TSC fusion.

We summarize discussions as;

1) The de-oxidation of PdO may be made mostly

during the baking processes between D(H)-loading runs.

- 2) The PdO-coated layer of Pd-nano-particle may arrange fractal nano-dips on its surface when D(H)-gas is charged and de-oxidization molecules (D₂O or H₂O) are released.
- 3) Fractal nano-dips may make local deep adsorption potentials, through which rapid penetration of D-atoms (ions) into deeper Pd-local lattice (Bloch potential) O-sites of nano-particle may be induced, to realize full or over-full D(H) loaded state ($x > 1.0$) of PdD_x in a short time of the Phase-I process.
- 4) Formation of D-clusters, such as predicted by the TSC theory³⁻⁵ on surface may be enhanced at sub-nano-dips.
- 5) D-motion in a “mesoscopic deep collective potential” of the nano-PdD_x system may be quasi-free to enhance transient D-cluster (4D/TSC³⁻⁵) formation probability around tetrahedral sites of local Bloch (periodical-lattice) potential inside a PdD nano-particle. This state can be modeled by the non-linear combination of two oscillations, i.e., one by the deep (about 1.5eV deep) well-type collective (global) potential and the other by the lattice-type (local) periodical three dimensional Bloch potential (about 0.22eV deep). This state may be simulated with a coupled motion of a long and a short pendulum, which show very enhanced-energy oscillation for a short pendulum⁶.

2. Formation and Reduction of PdO Surface Layer of Pd-Nano-Particles

Virgin samples of Pd/ZrO₂ (PZ in abbreviation) as provided from the maker (Santoku Co.) contain oxygen in the form of PdO/ZrO₂ with 100% PdO and ZrO₂.

Before the first D(H)-charging runs (by the twin system^{1,2,7}), we set up PZ samples in reaction chambers of the twin system, evacuate the chambers and bake samples at 200° C to remove “already absorbed” impurity gases. Since samples have been reserved in air for a few months, Pd-particles (PdO) would have absorbed a considerable amount of hydrogen in air (0.01% of air is H₂ gas). During a baking process, significant portion of PdO would have been de-oxidized by forming D₂O (H₂O) vapors to be evacuated. PZ

samples may be a composite of (PdO)_yPd_x/ZrO₂ with x + y = 1.0. We have then made the first D(H)-charging runs to observe D(H)/Pd loading ratios and heat-power evolution in Phase-I and Phase-II & III. Before the second D(H)-charging runs for used PZ samples, we have made evacuation and baking. In this second baking stage, we speculate that almost 100% reduction of PdO would have been done by “water-formation” reactions between out-going D(H) atoms and oxygen atoms in PZ sample under the elevated temperature (200° C). Such an experimental procedure as above mentioned is flow-charted in Fig.1.

We refer an essential results of Kitamura et al PLA 2009 paper⁸, for heat evolution under D(H)-gas charging to three kinds of Pd powder samples (PP, PB and PZ), as shown in Fig.2.

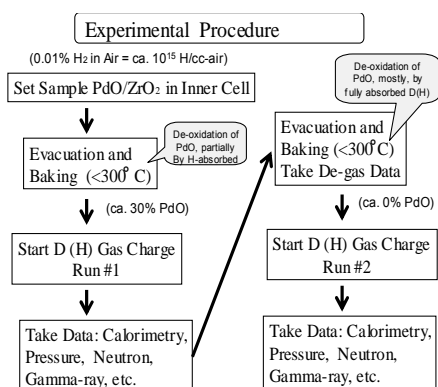


Fig.1: Experimental procedure of D(H)-gas charging to Pd/ZrO₂ powder samples and reduction of PdO

How can we explain the results of anomalously enhanced heat-power evolutions for PZ samples both for D- and H-charging, and why D-charging gave significantly larger heat in Phase-I and only gave positive heat-power level in Phase-II? What is a role of PdO component, since the second D(H)-charging runs with used samples (without PdO component) gave very reduced D(H)/Pd-loading ratios and heat? Experiments

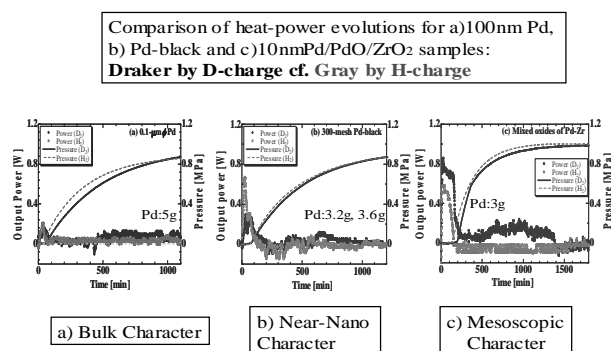


Fig.2: Comparison of typical heat evolution data for PP (0.1 micron diam. Pd powder), PB(300 mesh Pd-black powder) and PZ(10nm-Pd-nano-powder dispersed in ZrO₂ flakes)

with forced oxidation¹² (4-8% of total Pd amounts) to used PZ and PNZ (Pd/Ni/ZrO₂) samples showed remarkable recovery for D(H)/Pd ratios (up to 1.1-1.2) and heat levels (0.8 to 2.0 eV) in Phase-I. What is the mechanism for that? Are these phenomena related to the proposed mechanisms of Takahashi’s TSC formation models and D-cluster (4D, typically) fusion reactions?

3. A Phenomenological Model of D(H)-Adsorption/Absorption with PdO Layer

From our analysis of forced-oxidation experiments⁷, we have speculated that a portion, maybe around 30% ($y = 0.3$ or so)⁷, of PdO was remained at the

beginning of the first D(H)-charging runs. An image of atomic scale cross section of PdO/Pd nano-particle (5 nm diameter, for instance) is shown in Fig.3. We are going to propose a mechanism that oxygen of PdO layer will serve as a “seed” for inducing anomalous rapid full D(H)-loading in a first (virgin) D(H)-charging run.

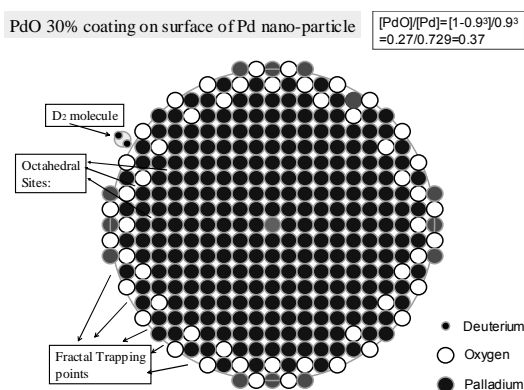


Fig.3: An atomic scale cross sectional image of PdO-layer coated (30%, $y=0.3$) Pd nano-particle; here we used relative sizes of ionic radii and D_2 molecule, and fractal surface structure is supposed to make a role enhancing deeper adsorption potential for D(H)-gas

A “sub-nano-hole” (SNH) will be born when D(H)-gas will be started to charge and formation of D_2O (H_2O)

will happen by incoming $\text{D}_2(\text{H}_2)$ gas molecule to combine (de-oxidize PdO) with oxygen. Formed D_2O (H_2O) molecule will go out to vacuum, and a SNH with chemical electron dangling bonds will be generated. As the trapping potential of SNH will be “very” deep (strong sticking force), incoming D_2 molecules will be doubly (or more) trapped there to form a transient TSC (transitory Bose condensate) with certain probability. Once a TSC ($t=0$) formed, very fast (in 1.4 fs) condensation to very small (in 10-20 fm diameter) charge neutral entity (TSC-min) which will cause 100% 4d-simultaneous fusion to produce two ^4He products with heat ($23.8\text{MeV}/^4\text{He}$)³⁻⁵. Image of such a process is illustrated in Figs.4-7. After such an event of D_2 trapping at SNHs, remained surface fractal nano-holes will trap more incoming D(H)-gas and enhance “rapid diffusion” into inner PdDx lattice points (namely O-sites of local PdD lattice).

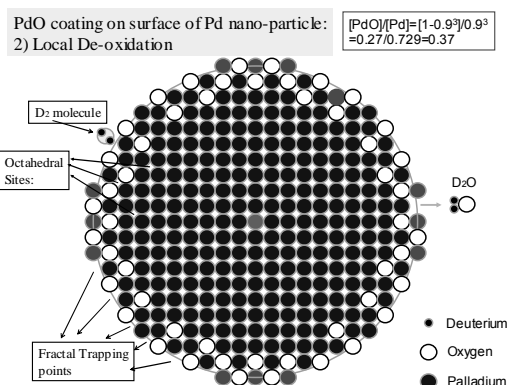


Fig.4: D_2O molecule going out

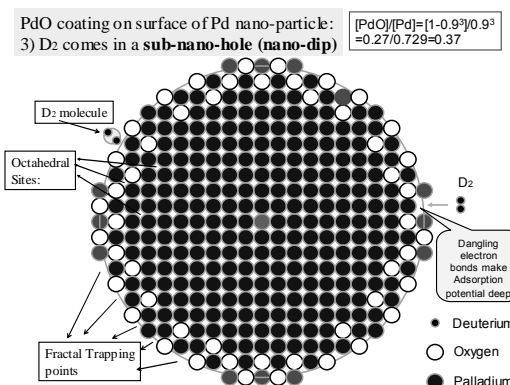


Fig.5: SNH traps D_2 incoming

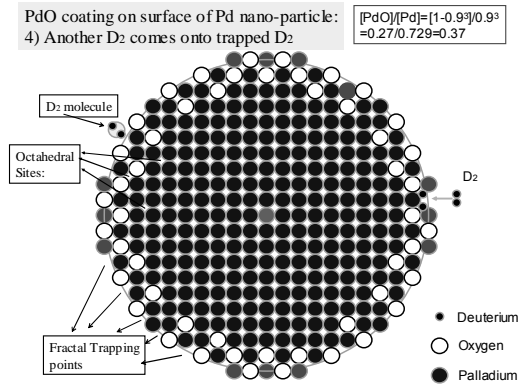


Fig.6: Eventual double D₂ trapping

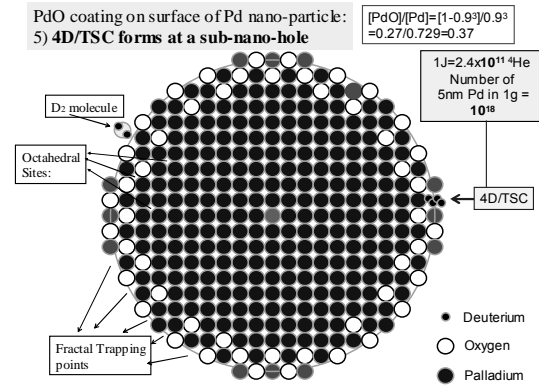


Fig.7: Eventual 4D/TSC fusion on surface

As shown in an insert (right top) of Fig.7, 1g of Pd nano-powder contains 5nm-diam. nano-particles of 10^{18} (on the order). Since 10^{11} 4d/TSC fusion events corresponds to one joule, one watt heat-level is maintained by TSC formation rate of one over 10 million Pd nano-particles per sec for PZ sample

containing one gram net Pd atoms. This condition looks feasible, in reference to observed heat-power evolution levels by Kitamura et al^{1,2,7}.

A typical data reported by Kitamura et al⁷ for Phase-I is expanded and shown in Fig.8.

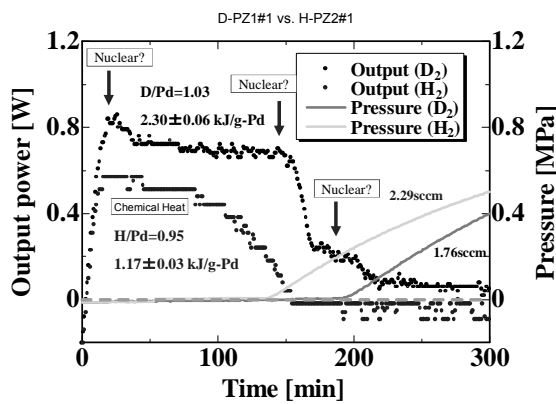


Fig.8 Expanded view of heat-power evolution data by Kitamura et al⁸ for PZ samples

We can consider that the heat-power evolution curve for H-charging is by chemical heat producing reactions, while the curve for D-charging may have component of some isotope effect, probably “nuclear heating” as shown with specific patterns (see arrows). Data by the twin system⁸ gave different end-points of Phase-I for the H-charging and D-charging, respectively, and D(H)/Pd loading ratios are slightly different. We can draw normalized curves by adjusting time-intervals of Phase-I and loading ratios, as shown in Fig.9.

From Fig.9, we can have impression that a beginning peak and a later bump of heat-power evolution in the D-charging run look like “nuclear heating”, while bumps around 200 min are due to pure chemical heat. We have observed and deduced similar normalized heat evolution curves three times for PZ virgin samples in 2008-2009. Hioki et al (Toyota Central Research Laboratory) have reported⁹ similar heat evolution curve having a very clear peak (sharp spike) in the beginning and a broad bump later for a PZ sample (from Santoku Co.). To assure that this is really due to nuclear (fusion) heat, we have of course to detect correlated ash (maybe alpha particles, other minor charged particles, secondary X-rays, EUV and visible lights) on line and/or off-line. This is our future task.

We can feel now vividly, by such normalized heat-power evolution runs taken by a twin system, that released heat by D-charging has a significant component of “some D-related fusion” reactions.

The mechanism of D(H)-absorption in Phase-I is independent of that in Phase-II (the new second phase²). The former is a rapid process of absorption with relatively large heat-power level, while the latter looks a slower process with relatively weak (about 1/10 of that in Phase-I) heat-power levels. We need to study possible

competition between adsorption, absorption and desorption in the new Phase-II.

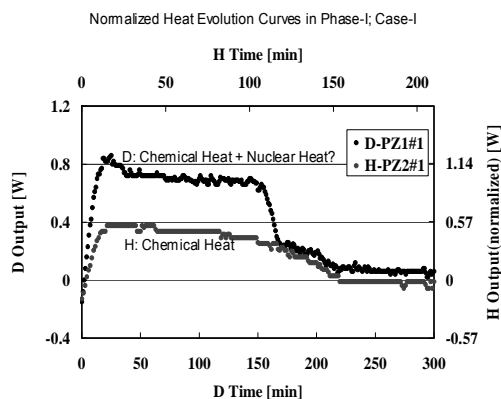


Fig.9: Normalized heat-power evolution curves in Phase-I for PZ samples⁸, comparing D-gas run and H-gas run

Time-dependent D(H)-absorption rate in Phase-I

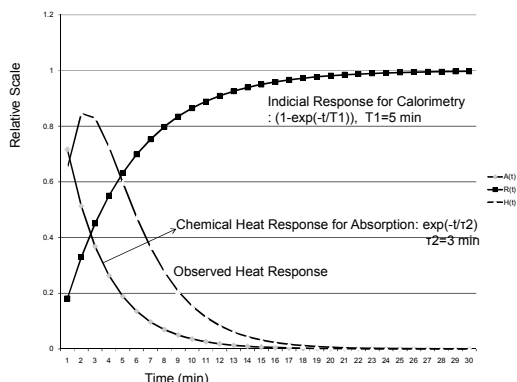


Fig.10: Observed heat response is broadened by indicial response of calorimetry

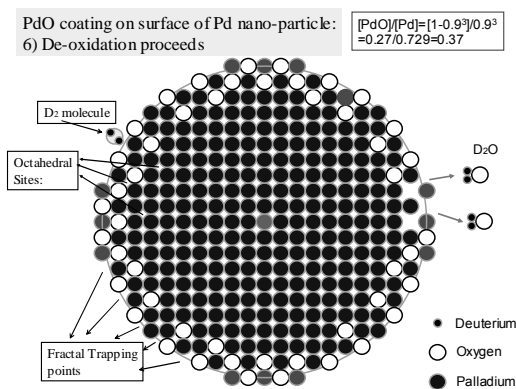


Fig.11: Extended sub-nano dips by D₂O formation

draw decay curves of almost same rates both for D- and H-charging². This fact is another background that the heat-power evolution for D-charging (Fig.9) looks like containing nuclear origin component. Our calorimetry system had a time resolution (time constant) of 5.2 min and observed heat evolution curve became a convolution with its indicial response and “supposed exponential” absorption rate, if heat release rate is constant as a function of loading ratio, as shown in Fig.10. Actually observed heat response by H-charging, namely “pure” chemical heat-power response, is shown in Fig.8, for example.

The trend of rising curve of heat-power evolution for H-run resembles to the simulation (Fig.10), but the falling curve is much steeper than the simulation. This fact suggests that the chemical heat release rate in Phase-I for H-run is non-linearly changing during the Phase-I interval.

Now we come back to follow the simulation after Fig.7 for D(H)-absorption into Pd nano-particle. Double D₂ trapping in a SNH does not always make a TSC, but does make reaction with near-by oxygen to form D₂O molecules and extended SNH as shown in Fig.11. Through the extended SNH, deuterons trapped diffuse to inner O-sites as shown in Fig.12.

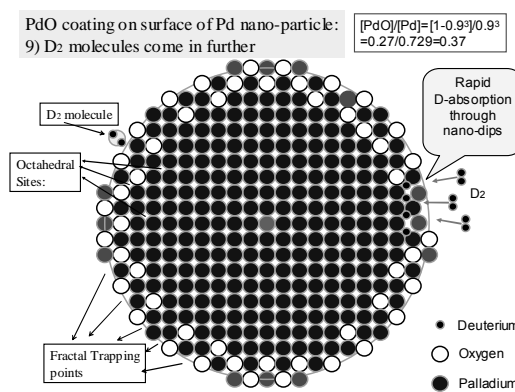


Fig.12: Incoming D₂ molecules are trapped one after another, by dangling bonds of SNH (sub-nano-holes/dips)

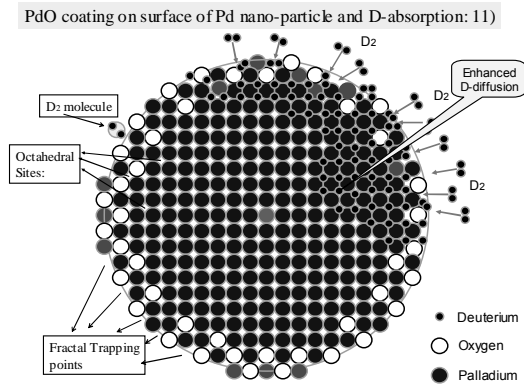


Fig.13: Trapped deuterons diffuse inside with enhanced speed by “D-pressure” from backside

In **Fig.13**, we draw an image of D-diffusion enhanced by pressure of incoming deuterons from backside through the extended SNH. Finally, at the end of Phase-I, Pd nano-particle is fully loaded (PdD, $x=1.0$), but we have additional trapped deuterons on surface (in SNHs)

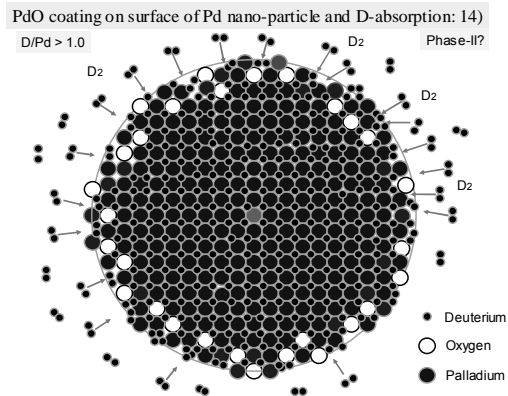


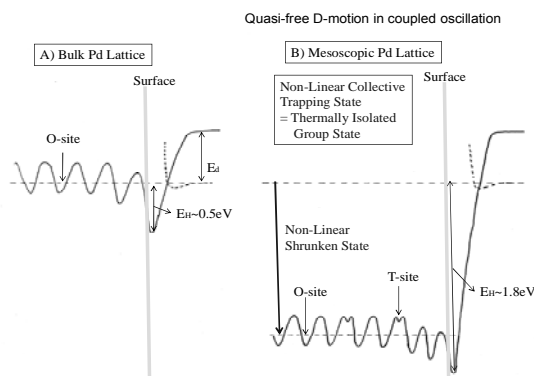
Fig.14: Feature at the end of Phase-I; full D(H)-loading in O-sites plus surface D_2 trapping makes $D(H)/Pd > 1.0$

and apparent x -value becomes more than unity, typically as we can roughly calculate from the drawing, $x=1.1-1.3$ which agrees well with observed Phase-I $D(H)/Pd$ ratios^{1,2,7}. This feature is drawn in **Fig.14**.

4. A Phenomenological Model in Phase-II

As shown in Fig.14, PdD local lattice may be formed inside a Pd nano-particle in Phase-II. We have in addition trapped deuterons (possibly making D-clusters) on surface SNHs. For a known characteristics of bulk Pd metal for D(H) absorption, we have potential forms as shown in **Fig.15** left figure for the surface adsorption and trapping (absorption) in inner lattice O-sites¹⁰.

The surface adsorption energy (depth of potential) is 0.5eV and lattice absorption energy is 0.2eV, as evaluated in a standard text book¹⁰. Therefore heat



release level for a bulk Pd sample is around 0.2eV, since number of trapped deuterons on surface is negligible. In contrast, observed specific absorption energy by PZ (and PNZ) samples are very large, namely around 2eV, about 10 fold of bulk value. To explain observed anomalous values of D(H) loading under rapid loading process and such high specific heat-energy level, we need to propose some new mechanism. We speculate and model that surface adsorption potential becomes very deep as 1.5-1.8eV for a nano-Pd particle and local periodical Bloch potential should be in “shrunk state” within a global potential well, as shown in right figure of **Fig.15**.

Fig.15: Collective (global) shrunken state potential of Pd nano-particle for D(H) trapping, right figure, compared with a bulk metal trapping potential, left figure. A quantum mechanical effect of mesoscopic system of nano-PdD x with surface PdO layer would make a deep global trapping (adsorption) potential well for incoming D(H)-molecules with local “shrunk” Bloch (periodical) potential of PdD x lattice.

Existence of PdO surface “barrier” and formed SNHs would make very deep D(H) adsorption potential on surface (1.5-1.8eV deep), which is categorized as an collective mesoscopic potential well (CMPW, or a global potential for a nano-particle). Inside a CMPW confinement, three-dimensional PdD lattice (Bloch) potential is formed as local fine structure in “shrunk state”. The CMPW potential induces a QM non-harmonic oscillation, and the local Bloch potential induces a QM harmonic oscillation (wave function becomes a Hermite function, of which ground state is Gaussian and highly excited state has a U-shape wave-function¹¹). Two QM oscillations combine non-linearly⁶ to make D-motion inside a nano-Pd particle highly free (quasi-free) under the three dimensional constraint of PdD Bloch structure. This quasi-free motion of deuterons by the local high excited states inside a mesoscopic nano-particle enhances very much probability of TSC (tetrahedral symmetric condensate³⁻⁵) formation as we give an image of QM wave superposition in **Fig.16**¹¹.

In **Fig.17**, we show a flow-chart drawing of useful potential forms in Coulombic (electro-magnetic) and nuclear strong interaction starting from a simple system of atom and two nucleons to more complex systems as D-cluster, mesoscopic nano-particle and bulk material. By defining useful potentials for interactions in every step, we can extend quantum-mechanical (QM) analyses by using many body Schroedinger equations (or dynamic equations as QM-Langevin equation³⁻⁵). Fusion reactions in microscopic random systems (gas and plasma) can be treated by using a simple Coulombic potential and a one pion exchange potential (OPEP)¹². For D-cluster systems, we can apply special trapping potential forms for Coulombic interactions based on Platonic symmetry (orthogonal coupling) between electron wave functions and deuteron wave functions³⁻⁵.

For multi-body strong interactions of 4D, 6D, 8D, etc cluster fusion reactions, we can use an empirical formula of PEF (pion exchange force) to scale S-factors or transition matrices for imaginary part of nuclear optical potentials³⁻⁵.

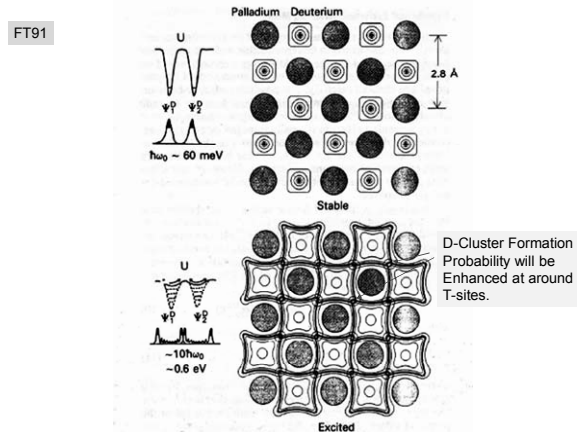


Fig.16: Quasi-free motion of deuterons by local high excited states inside a mesoscopic CMPW potential enhances TSC formation around T-sites of local PdD lattice of Pd nano-particle, copied from Ref-11

The specific nature of condensed matter is of constraint (ordering or self-organization) motion of particles with lattice regularity or surface fractals. A global shrunk state potential well for trapping D(H) atoms in deep hole will realize a non-linear oscillation mode⁶ coupled with harmonic oscillation in PdD lattice, which makes deuteron motion inside a nano-particle quasi-free under ordered constraint to induce enhanced cluster (TSC) formation probability. A bulk Bloch potential (periodical) is useful for established states of D(H) absorption. We speculate that D-cluster fusion is induced in the states of D-cluster and D-mesoscopic systems.

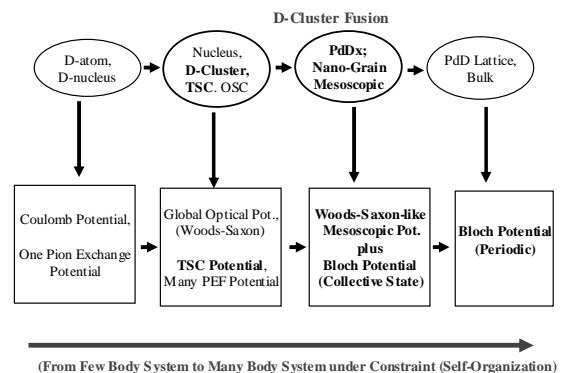


Fig.17: Speculation of useful potential forms to be applied for QM calculations to estimate fusion reaction rates from a simple system to many body, mesoscopic and bulk condensed matter systems

5. Concluding Remarks

- 1) With a PdO surface layer, sub-nano-holes (SNH) are formed in the beginning of D(H)-gas charging. This SNH would become a seed of “anomalous phenomena” in D(H)-loaded Pd nano-particle samples.
- 2) PdO layer also helps to make up a global deep mesoscopic trapping potential well which covers shrunken state of local PdD lattice Bloch potentials.
- 3) In SNHs, formation of 4D/TSC is largely enhanced in the Phase-I interval of D(H)-gas loading. 4D fusion thus

induced may be a main nuclear component of heat release in Phase-I.

- 4) Within a global mesoscopic potential with local Bloch potentials, quasi-free D-motion is induced by non-linearly coupled oscillations for the global QM state (long pendulum) and a local harmonic oscillator (short pendulum). The quasi-free motion under the constraint of three-dimensional local lattice structure greatly enhances TSC formation. Anomalous heat by D-charging in Phase-II may be by 4D/TSC fusion of this process.

References

- 1) Y. Sasaki, Y. Miyoshi, A. Taniike, A. Kitamura, A. Takahashi, R. Seto, Y. Fujita: Measurements of heat and radiation from Pd nano-powders during absorption of hydrogen isotopes, Proc. JCF10, 2010, to be published
- 2) Y. Miyoshi, Y. Sasaki, A. Taniike, A. Kitamura, A. Takahashi, R. Seto, Y. Fujita: Two absorption/adsorption processes of hydrogen isotopes observed for Pd nano-powders, Proc. JCF-10, 2010, to be published
- 3) A. Takahashi, N. Yabuuchi: “Study on 4D/TSC condensation motion by non-linear Langevin equation”, In *ACS Symposium Series 998; Low Energy Nuclear Reactions Source Book*; Marwan, J, Krivit, S. Eds.; American Chemical Society, Oxford University Press: Washington DC, 2008, pp 57-83
- 4) A. Takahashi, “The basics of deuteron cluster dynamics as shown by a Langevin equation”, in *LENR Source-Book 2*, edited by J. Marwan and S. Krivit, Washington DC, American Chemical Society, 2009, pp.193-217
- 5) A. Takahashi, *J. Condensed Matter Nuclear Science*, **2**, 33-44 (2009).
- 6) Brian Ahern: Private communication in 2009
- 7) Akira Kitamura, Akito Takahashi, Yu Sasaki, Yuki Miyoshi, Akira Taniike, Reiko Seto and Yushi Fujita: “Heat Evolution from Pd Nanopowders Exposed to High-Pressure Hydrogen Isotopes and Associated Radiation Measurements”, J. Marwan Ed., *LENR Information Sourcebook*, American Institute of Physics, to be published in 2010
- 8) A. Kitamura, T. Nohmi, Y. Sasaki, A. Taniike, A. Takahashi, R. Seto, Y. Fujita: *Physics Letters A*, **373** (2009) 3109-3112
- 9) T. Hioki, H. Azuma, T. Nishi, A. Itoh, S. Hibi, J. Gao, T. Motohiro, J. Kasagi: “Hydrogen/deuterium absorption capacity of Pd nanomaterials and its relation with heat generated upon loading of hydrogen isotope gases”, Proc. JCF10, 2010, to be published
- 10) Y. Fukai, K. Tanaka, H. Uchida: “Hydrogen and Metal”(in Japanese), ISBN4-7536-5608-x C3042, Material Series, Uchida Rokakuho Publ., Tokyo, 2002
- 11) A. Takahashi, T. Iida, F. Maekawa, H. Sugimoto, Y. Yoshida: *Fusion Technology*, **19** (1991) 380-390
- 12) T. Hamada, I. Johnston: *Nuclear Physics* **34** (1962)382

A power spectrum change by irregular periodicity of superlattice at tunnel resonance of CF

M. BAN: ban.masanobu@hikaku.metro.tokyo.jp

Tokyo Metropolitan Leather Technology Center, 3-13-14, Higashi Sumida, Sumida Tokyo 131-0042 Japan

H. NUMATA

Tokyo Institute of Technology, 2-12-1, O-okayama, Meguro Tokyo 152-8552 Japan

Abstract: Low energy nuclear reactions (LNER) and CF anomaly, such as nuclear transmutations are occurred with a direct current flowing or forced gas permeation experiment through heterostructure: Pd/Au and Pd/CaO multilayered Pd. We have been concerned with quantum transportation of charged particles, e.g. electron and deuteron, which governed by tunnel resonance of the hypothetical lattices. In this study, we calculated the electron transmission coefficients on varying the applied electric field. Numerical calculation of quantum transport has been performed using T matrices of the one-dimensional (1D) structures. On calculation we postulated the corresponding heterostructure as superlattices (alternating sequence of potential barriers and wells) under the constant electric field. Moreover, the deviation of the periodicity of the potential barriers and wells was introduced to simulate more realistic interface. Both the results with superlattice and a little disturbed lattices showed $1/f^2$ power spectra, which means that on the occasion of CF charged particles transfer through the interface accompanied with quantum resonance same as tunnel resonance of superlattices. On view point of matter wave similar quantum resonance might occur even in the gas permeation experiment.

Keyword: 1/f noise, transition probability, electron, tunnel effect, electron wave, cold fusion

1 Introduction

The generation of heat and/or emissions of neutron or charged particles by CF occurred with a direct electric current flowing.¹⁾ Nuclear transmutations were also observed by forced gas permeation experiment.²⁾ During deuterium gas permeation the transfer of deuteron steadily occurs through deuterated Pd/CaO heterostructure: front side in a deuterium atmosphere and back side in a vacuum, where conversion of nuclide is observed. However, up to now, the transportation of these charged particles within the layer has attracted little attention. There still has been equivocal how these charged particles transfer deuterated Pd having very high D/Pd ratio to Au through the interface region. Noticeably, the Pd/Au layer possesses many lattice defects and vacancies formed during the sample preparation process. To simulate such highly deuterated Pd and the interface region we introduced superlattices with the regular periodic potential and that a little disturbed, even though the structure of the above heterostructure: a real crystal structure might be far from an ideal one.

Storms et al.³⁾ suggested that the initiation of excess heat generation and nuclear transmutations needs a time sufficient to achieve high D/Pd ratio, which implies the orderly arrayed crystal build up in the Pd and interface region due to high energy deuteron permeation. Kim et al.⁴⁾ reported the experimental results will be explained theoretically in relation with high mobile quasi-free deuterons elucidated by Fukai et al. Recent studies by Ban were devoted for the theoretical approach to elucidate the existence of matter wave propagation within the lattices in a tunnel resonant state.^{5, 6, 7)} These studies

demonstrate that transportation of charged particles in the specified medium plays an significant role on emerging the anomalous phenomena of CF. Those phenomena of CF have been commonly caused by a flow of quanta. Then, we can postulate the motion of charged particles, i.e. electron and deuteron as a quanta which transmission is governed by tunnel resonance of superlattices. On calculation of transmission coefficients we referred Nakamura et al.'s report⁸⁾ that investigated quantum transport on superlattices in terms of the time evolution and power spectra.

In this study, the transmission behaviors of electron in superlattices are evaluated using a transfer matrix of a 1D structure. The results are well agreed with those reported by Nakamura et al. Next we introduce the deviation of the periodicity of the potential barriers and wells to study the nonstationary quantum transport of a little disturbed superlattice. By numerical calculation the existence of robust tunnel resonance predicts that quantum transport of these charged particles will continue stable situation even in these disturbed or oscillatory structures.

2 Calculation method and results

2.1 Description of model and derivation of transfer matrix

Although transport of electrons is strongly regulated by consecutive potential barriers and wells, e.g. in modulation doped GaAs-AlGaAs heterojunctions, the conductance jump by the breakdown of resonant tunneling conditions in the applied voltage was observed.⁹⁾ This is because the evolutions of the quantum transport prevail

over the corresponding medium resulting the full transmission.

Now suppose that such quantum transport of electron would substantially play a significant role on the CF experiments. For simplicity, we introduce the quantum transport of electron in a 1D superlattice where n periodic potential barriers and wells are distributed over the corresponding medium of the CF sample. We neglect a realistic multiband and multiscattering and so take into consideration Zener tunneling under the external applied voltage.

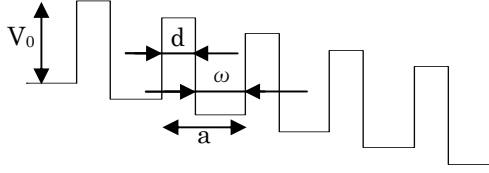


Fig.1 Schematic diagram of potential distribution of superlattice. V_0 and d denote height and thickness of barrier and ω is thickness of well. Superlattice constant a : $a = d + \omega$

Figure 1 shows the schematic diagram of a Kronig-Penny model of a simple superlattice where n periodic rectangular barriers and wells are depicted under the constant electric field \bar{F} .

In this study, we have carried out the calculation of 1D quantum transport at the constant electric field using the transfer matrix method. The Hamiltonian is given with the periodic potential $V(x)$ and constant electric field \bar{F} (see Fig.1)

$$H = \frac{-\hbar^2}{2m} \frac{d^2}{dx^2} + V(x) - \bar{F}x \quad (1)$$

The incident and reflected waves for $x < 0$ and the transmitted wave after n^{th} barrier are given

$$\Psi_0 = \exp(i k_0 x) + S_{11}(n) \exp(-i k_0 x) \text{ for } x < 0 \quad (2)$$

$$\Psi_n = S_{12}(n) \exp(i k_n x) \text{ after } n^{\text{th}} \text{ barrier} \quad (3)$$

where S_{12} and S_{11} are the transmitted and reflected wave amplitudes, respectively.

On the other hand, for the transfer of electron over the barrier and well, the wave function at the j^{th} barrier and well is given by

$$\Psi_j = A_j \exp(i k_j x) + B_j \exp(-i k_j x) \text{ at } j^{\text{th}} \text{ well}$$

$$= C_j \exp(i K_j x) + D_j \exp(-i K_j x) \text{ at } j^{\text{th}} \text{ barrier} \quad (4)$$

where $K_j = \sqrt{K_0^2 + F(j-1)}$, $k_j = \sqrt{k_0^2 + Fj}$, $F = 2m\bar{F}/\hbar^2$ and $K_0^2 = k_0^2 - 2mV_0/\hbar^2$. Also A_j and C_j are the transmitted wave amplitudes. B_j and D_j are the reflected wave amplitudes.

Considering the continuity and smoothness conditions the transfer matrix M_j between successive set of coefficients is given by

$$\begin{pmatrix} A_j \\ B_j \end{pmatrix} = M_j \begin{pmatrix} A_{j-1} \\ B_{j-1} \end{pmatrix} \quad (5)$$

where the transfer matrix M_j is given by

$$M_j = \begin{pmatrix} e^{-ik_j(j-1)a} & 0 \\ 0 & e^{ik_j(j-1)a} \end{pmatrix} \begin{pmatrix} \alpha_{1j} & \beta_{1j} \\ \beta_{1j} & \alpha_{1j} \end{pmatrix} \begin{pmatrix} e^{ik_j d} & 0 \\ 0 & e^{-ik_j d} \end{pmatrix} \begin{pmatrix} \alpha_{2j} & \beta_{2j} \\ \beta_{2j} & \alpha_{2j} \end{pmatrix} \begin{pmatrix} e^{ik_{j-1}((j-1)a-d)} & 0 \\ 0 & e^{-ik_{j-1}((j-1)a-d)} \end{pmatrix} \quad (6)$$

$$\begin{aligned} \text{with } \alpha_{1j} &= (k_j + \kappa_j)/(2k_j) \quad , \\ \alpha_{2j} &= (\kappa_j + k_{j-1})/(2\kappa_j) \quad , \\ \beta_{1j} &= (k_j - \kappa_j)/(2k_j) \quad , \\ \beta_{2j} &= (\kappa_j - k_{j-1})/(2\kappa_j). \end{aligned}$$

By iterating under the boundary condition $A_0 = 1$, $B_0 = S_{11}(n)$, $A_n = S_{12}$ and $B_n = 0$, one obtains

$$S_{12}(n) = \frac{\det Q_n}{(Q_n)_{22}}, \quad S_{11}(n) = -\frac{(Q_n)_{21}}{(Q_n)_{22}} \quad (7)$$

with $Q_n = \prod_{j=1}^n M_j$.

The transmission and reflection coefficients are given by

$$T_n = \frac{k_n}{k_0} |S_{12}(n)|^2 \quad (8)$$

$$R_n = |S_{11}(n)|^2. \quad (9)$$

The calculation of the transmission coefficients T_j as a function of the number of barriers j was carried out for different applied potentials $F = 0.001$, $k_0 = 10$, $V_0 = 1$, $a = 1$.

The values of T_j vs. the number of barriers exhibit a sequential oscillation around an averaged value between upper and lower plateau values. In Fig.2 the solid line shows the power spectra $P(f)$ in logarithmic scale for the time sequence $\{T_j\}$ defined by

$$P(f) = \left| N^{-1} \sum_{n=1}^N T_n e^{-2\pi i f n / N} \right|^2 \quad (10)$$

2.2 Calculation of the transmission coefficients using transfer matrices with regular width of the barrier a

The calculations of transfer matrices were conducted at a constant a of 1 using Mathematica.

Mathematica's calculation procedure

$$d = 0.1$$

$$a = 1$$

$$F = 0.001$$

$$k_0 = 10$$

For Mathematica functions the following equations are defined

$$\kappa_0 = \sqrt{k_0^2 - 2m_0 \cdot V_0 / \hbar^2}$$

$$k[j_] := \sqrt{k_0^2 + F \cdot j}$$

$$\kappa[j_] := \sqrt{\kappa_0^2 + F \cdot (j - 1)}$$

$$\alpha_1[j_] := (k[j] + \kappa[j]) / (2k[j])$$

$$\alpha_2[j_] := (k[j-1] + \kappa[j]) / (2k[j])$$

$$\beta_1[j_] := (k[j] - \kappa[j]) / (2k[j])$$

$$\beta_2[j_] := (\kappa[j] - k[j-1]) / (2k[j])$$

For the conversion coefficients of units and physical constants the following notations are used

$$m = 9.11 \cdot 10^{-31}$$

$$h = 6.626 \cdot 10^{-34}$$

$$\hbar = h / (2\pi)$$

$$m_e = 0.067$$

$$eV2J = 1.602 \cdot 10^{-19}$$

$$nm2m = 10^9$$

$$\hbar eV = \hbar / eV2J \cdot nm2m$$

$$m_0 = m / eV2J \cdot m_e$$

The power spectrum is calculated through the following Mathematica do loop at n=4096.

$$S_{12}[j] := \frac{\text{Det}[Qn]}{Qn[[2,2]]}, \quad S_{11}[j] := \frac{-Qn[[2,1]]}{Qn[[2,2]]}$$

$$\text{Sample} = 2^{12} = 4096$$

$$\text{Do}[Qj = Qj \cdot M[j],$$

$$Qn = Qj;$$

$$T[j] = \frac{k[j]}{k_0} \text{Abs}[S_{12}[j]]^2;$$

$$\text{data} = \text{Table}[S_{11}[j],$$

$$\{j, 1, \text{sample}\}]$$

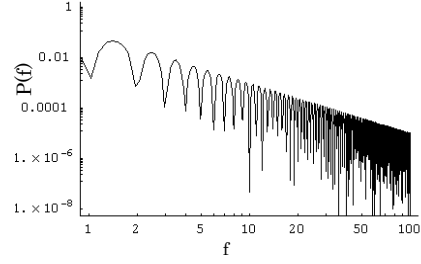


Fig. 2 Power spectrum P(f) of in logarithmic scales

As is seen in Fig.2, the envelop line of the power spectrum almost coincide a line with a slope of $1/f^2$. The peculiar spectrum of the

transmission coefficient resembles chaos, which was further discussed accompanied with non-autonomous system.⁹⁾ By comparison our results with that of Nakamura's we confirmed that the procedure of this study is fully consistent with that of Nakamura's calculation.

2.3 Result of transmission coefficients with disturbed width of the barrier a

In the case of GaAs heterojunctions Wannier-Stark resonances in Zener tunneling have much attention.⁹⁾ This allows us to conceive that the features of tunnel resonance states are deeply concerned with the structural disturbance in the corresponding interface. Incorporating the following Mathematica's do loop, we carried out the calculation for different superlattice which potential distribution is shown in Fig.3.

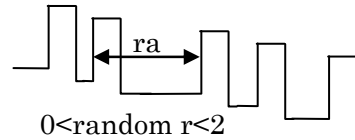


Fig. 3 Schematic diagram of potential distribution of disturbed superlattice with random r uneven of distance ra.

At first a part of eq.(6) is replaced in the next variables.

$$(j-1)a = \text{sekisankyori}$$

In Fig. 4 the power spectrum shows a distorted sequential fluctuation as a function of the frequency.

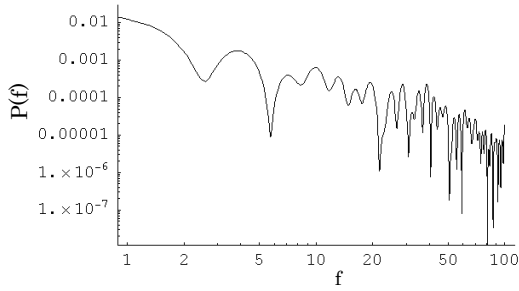


Fig. 4 Power spectrum $P(f)$ of in logarithmic scales, the envelop still seen almost coincide a line with a slope of $\frac{1}{f^2}$

Mathematica's calculation procedure

For the disturbed superlattice constant ra we denote the random numbers r , ranging from 0 to 2 as **ransuuhyou** and Mathematica's do loop was somewhat modified as

```

goukei = 0;
Do[goukei = ransuuhyou [[j]] +
  goukei, {j, 1, sample}];
tan syuku = goukei / sample;
bai = 1 / tan syuku
sekisankyori = 0
Do[r = ransuuhyou [[j]];
  sekisankyo ri = sekisankyo ri + a · r · bai;
  Qj = Qj · M [[j]];
  Qn = Qj;
  T[j] =  $\frac{k[j]}{k0}$  Abs[S12 [ ]]2;
  dataaS11[j] = S11 [ ];
, {j, 1, sample} ]

```

3 Discussion

In this study, the power spectra of the transmission of electron with the Kronig-Penny model in the constant electric field are calculated, which exhibits an envelope line with a slope of $\frac{1}{f^2}$ as a function of frequency. (Figs.2 and 4) On the other hand, Nakamura's results showed that the $\frac{1}{f^2}$ characteristics vs. frequency exhibited constancy on varying the barriers and the field strength. We have been, so far interested in the $\frac{1}{f^2}$ and $\frac{1}{f}$ characteristics on

quantum systems, such as $\frac{1}{f}$ tunneling current noise in STM.¹⁰⁾ The behavior shown by power spectrum is similar to the characteristics behavior of usual filter and radio tuner. In radio tuner, resonance occurs only at coherent waves. And whether such phenomenon occurs or not at quantum system was investigated by Ban.^{5,6,7)}

In order to consider the same logic as a cause of quantum resonance, this study especially confirmed the conditions of weakening quantum resonance. Figure 4 shows that even if the distance between a barrier and next one was changed irregularly, quantum resonance was little disturbed. Comparing Fig.4 with Fig.2 (the Kronig-Penny model), there still remained the $\frac{1}{f^2}$ characteristics. Thus, Quantum resonance continued strongly during which the distance between a barrier and next one was randomly changed from 0 to twice a .

In the Nakamura and Jauslin's calculations linear operation was conducted assuming the existence of a coherent wave.^{8,11)} Their calculation was based on unique frequency. On the spectrum calculation, we obtained many waves spread over wider frequency ranges, similar to their results.

By the way, $\frac{1}{f^2}$ characteristic is sure to exist in the band of a low frequency, and the character is quite the same as Figs. 2 and 4 in the signal of the impulse and the step though a lot of signals of the impulse and the step are observed by CF.

In CF, step or burst of neutron emission and heat generation has been observed. So, it's expected that, the potential barriers and wells get self-assembled in the system due to which transmission of electron occurs. If we seek for tunneling and transmission of quanta in CF, the transfer of electron through Pd/Au heterostructure might be realized as the medium subsequently to form superlattices.

In 1990s' physics development matter wave interference was substantiated by He, Na atom and fullerene beams¹²⁻¹³⁾, hence larger scale deuteron compared with electron is expected to exhibit quantum effect. As for macro quanta: deuteron the similar quantum transmission is expected as in the case of the electron transmission experiment through deuterated Pd/Au heterostructure. Thus larger molecule D₂ (actually deuteron) might permeate through Pd/CaO multilayered Pd film superlattices as quanta.

References

- ¹ E. Yamaguchi and H. Sugiura, Excess Heat and Nuclear Products from Pd/Au Heterostructures by the 'In-vacuo' Method, ICCF7, Vancouver, pp.420-424, 1998
- ² Y. Iwamura, M. Sakano and T. Itoh, Jpn. J. Appl. Phys. Vol.41 pp.4642, 2002
- ³ E. Storms, What Conditions Are Required To Initiate The Lenr Effect?, ICCF10, Cambridge, MA, 2003
- ⁴ Y. E. Kim, Theory of Bose-Einstein condensation mechanism for deuteron-induced nuclear reactions in micro/nano-scale metal grains and particles, Naturwissenschaften, Vol.96, 803-811, 2009
- ⁵ M. Ban, Composition of 1/f Amplitudes Electron Wave and a Work of One Dimension of Lattice, Proc.4th Meet. Japan CF Research Soc., p.90-94, 2002
- ⁶ M. Ban, Cold fusion associated with three kinds of matter wave resonance, Proc.6th Meet. Japan CF Research Soc., p.86-89, 2005
- ⁷ M. Ban, Tunnel Resonance of Electron Wave and Force of Fluctuation, ICCF12, pp.451-455, Yokohama, 2005
- ⁸ T. Haga, Y. Takane and K. Nakamura, $1/f^2$ Law in One-dimensional Quantum Transport: an Example of Weak Chaos in Quantum Systems, Chaos Solutions & Fractals, Vol. 5, pp. 1077-1083, 1995
- ⁹ K. Murayama, H. Nagasawa, S. Ozaki, M. Morifuji and C. Hamaguchi, Wannier-Stark resonance in Zener tunneling diodes with GaAs/AlAs superlattices, Superlattices and Microstructures, Vol.20, pp.493-498, 1996
- ¹⁰ S. Sugita, Y. Mera and K. Maeda, The Spatial Variation of 1/f Current Noise in Scanning Tunneling Microscopes, J. Vac. Sci. & Technol., B12, pp.2140-2143, 1994
- ¹¹ H.R. Jauslin, Chaotic properties in quantum scattering, Physica D, Vol.51, pp.200-204, 1991
- ¹² A. Markus, O. Nairz, J. Vos-Andreae, C. Keller, G. van der Zouw and A. Zeilinger, Wave-Particle Duality of C60 molecules, Nature, Vol. 401, pp. 680-682, 1999
- ¹³ O. Nairz, M. Amdt, and A. Zeilinger, Quantum interference experiments with large molecules, American Journal of Physics, Vol.71, pp.319-325, 2003

A theoretical study on the possible change of the phonon dispersion relation due to the nuclear reaction in solid II

Ken-ichi TSUCHIYA[†] and Satoshi FUJITA

Tokyo National College of Technology, 1220-2 Kunugida, Hachioji, Tokyo 193-0997

[†] E-mail: tsuchiya@tokyo-ct.ac.jp

Abstract: The phonon dispersion relation is one of the most important types of information concerning the properties of solids, because it is greatly affected by the lattice and electronic structure of solids. In this study, we have shown theoretical predictions about the effects of nuclear reactions in Pd crystals on the phonon dispersion relations. To begin with, one-dimensional palladium deuteride with nearest neighbor harmonic interactions has been considered. In this model, nuclear reactions are expressed as the structure changes of the one-dimensional lattice. This tends to increase the number of dispersion branches after the reaction. The model is very simple, but it can be applied to dispersion relations for the three-dimensional lattices.

Keywords: phonon dispersion relation, nuclear reaction in solids, palladium deuteride

1 Introduction

Phonon dispersion relations of metal hydrides and deuterides were studied in 1970's [1,2]. The motivation for that research was the increasing technical importance of metal-hydrogen systems in those days. From the point of view of the nuclear reactions in solids, they are still very interesting. So we have done measurements on the Raman spectra of Pd hydride and deuteride and reported them in JCF8 [3] and ICCF14 [4]. We have also reported the theoretical properties of phonon dispersion relations of Pd deuteride [5,6].

In this work we have developed these ideas and done some one-dimensional calculations for PdD lattice with nearest neighbor harmonic interactions. This problem is characterized by the dynamical matrix and the solutions of the eigenvalue problem can give the phonon states. The dynamical matrix is determined from the lattice structure and the interaction between the ions. It is summarized in our previous work [3,4]. In our model, calculation of dispersion relations by assuming the DD reactions with fusion product He

were done for the partially reacted case and the completely reacted case. If we see the same pattern in the phonon dispersion relation of Pd deuteride, it will be evidence of a nuclear reaction. These methods can be applied to the more complicated three-dimensional Pd deuteride lattice with some other nuclear reactions.

2 Results and discussions

Firstly, we consider the one-dimensional PdD lattice as a basic case, which is sketched in Fig.1. In this model, Pd and D exist on a straight line alternately. We only consider longitudinal vibrations along the line. The force constant between Pd and D is selected in order to be consistent with the experiments. The part surrounded by a rectangle means the primitive cell of the lattice.

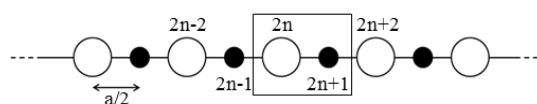


Fig.1 One-dimensional PdD lattice. White and Black circles mean Pd and D, respectively. The separation between Pd and nearest neighbor D is $a/2$. The part enclosed by the square is the primitive cell.

The phonon dispersion relation for this model is easily calculated by solving 2×2 eigenvalue problem. It has two solutions called optical and acoustic branch. The result is plotted in Fig.2.

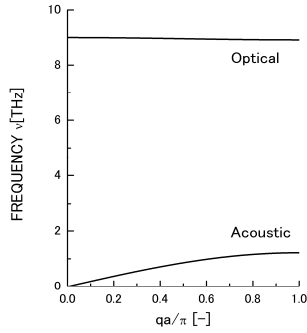


Fig.2 The phonon dispersion relation of one-dimensional PdD lattice. The wave number q is normalized by the size of the first Brillouin zone. Force constant β between Pd and D is selected as 5.2 N/m, which is consistent with Mohammad [7].

Secondly, we consider the following four cases shown in Figs. 3, 5, 7 and 9. They can be regarded as the lattices after the nuclear reactions starting from PdD shown in Fig.1. So, ${}^4\text{He}$ corresponds to the fusion product of a DD reaction. In spite of their extremely small cross sections, we adopt this reaction, because this is fundamental for analysis of nuclear reactions in solid. For all cases, force constant β between the neighboring Pd and D is determined to be consistent with the work of Mohammad [7]. The force constant α between Pd and Pd is selected as $\alpha/\beta=4.3$. The force constant γ between Pd and ${}^4\text{He}$ normalized by β is written in each figure.

2.1 Completely reacted model A

We consider the lattice model where all Ds in a one-dimensional PdD initiate DD reactions and completely become ${}^4\text{He}$, which is sketched in Fig. 3.

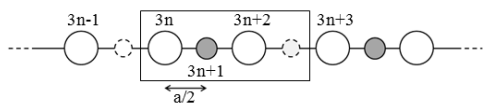


Fig.3 Sketch of completely reacted model A. Open circle with solid line means Pd and open circle with dashed line means D vacancy. Gray circle means He which is produced by DD reaction.

The vibration modes for this problem are characterized by 3×3 dynamical matrix. Therefore, it has three solutions. Solving the cubic equation by Newton's method, the phonon dispersion relations for this model with $\gamma/\beta=1$ and 2 were obtained. They are plotted in Fig. 4 (a) and (b). It is easy to see that the shape of the dispersion curve depends on the force constants while the number of the branches does not.

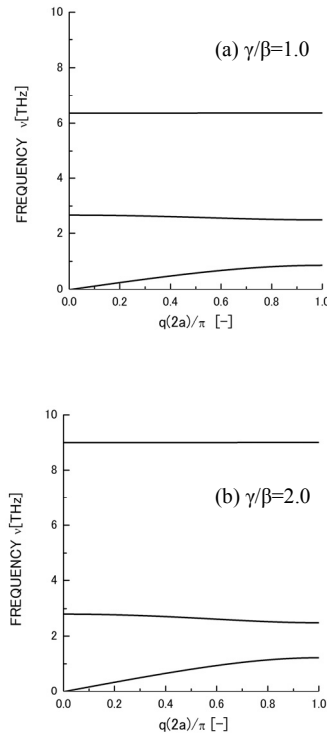


Fig.4 Phonon dispersion curves for completely reacted model A shown in Fig.3. The wave number q is normalized by the size of the first Brillouin zone.

2.2 Completely reacted model B

We consider another possible configuration for the completely reacted model sketched in Fig. 5. Comparing Figs. 3 and 5, their primitive cells are mutually different. Therefore, the phonon dispersion relation of this model is fundamentally different from the results in Fig. 4. The vibration modes for this problem are characterized by 6×6 dynamical matrix. Therefore, it has six solutions.

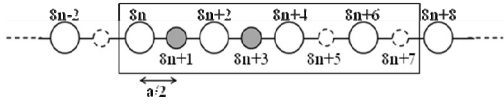


Fig. 5 Sketch of the completely reacted model B. Open circle with solid line means Pd and open circle with dashed line means D vacancy. Gray circle means He which is produced by DD reaction.

Phonon dispersion relations for this model with $\gamma/\beta = 1$ and 2 are plotted in Fig. 6 (a) and (b), respectively. The number of the branches is larger than that of the results for model A in Fig. 3.

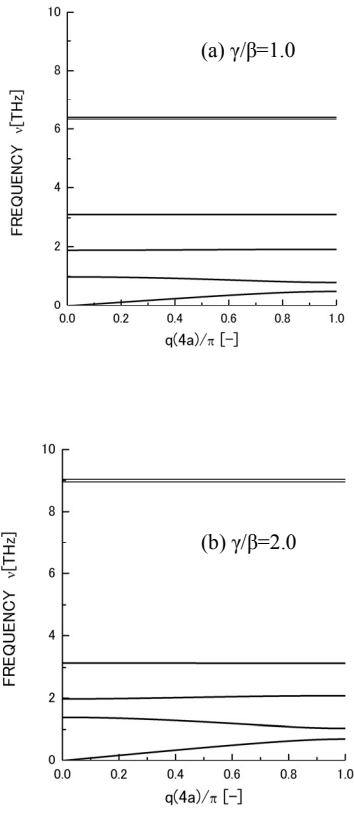


Fig. 6 Phonon dispersion curves for the completely reacted model B shown in Fig. 5. The wave number q is normalized by the size of the first Brillouin zone.

2.3 Partially reacted model A

Here, we consider the partially reacted case sketched in Fig. 7. This lattice contains unreacted D, which is expressed by black circle, because the reactions are partial. This is an example where two of the three D ions react and a He and a D vacancy are produced. The vibration modes for this problem are

characterized by 5×5 dynamical matrix. Therefore, it has five solutions.

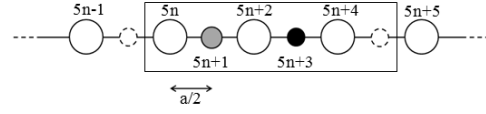


Fig. 7 Sketch of the partially reacted model A. Open circle with solid line means Pd and open circle with dashed line means D vacancy. Black circle means unreacted D. Gray circle means He which is produced by DD reaction.

Phonon dispersion relations for this model with $\gamma/\beta = 1$ and 2 are plotted in Fig. 8 (a) and (b), respectively.

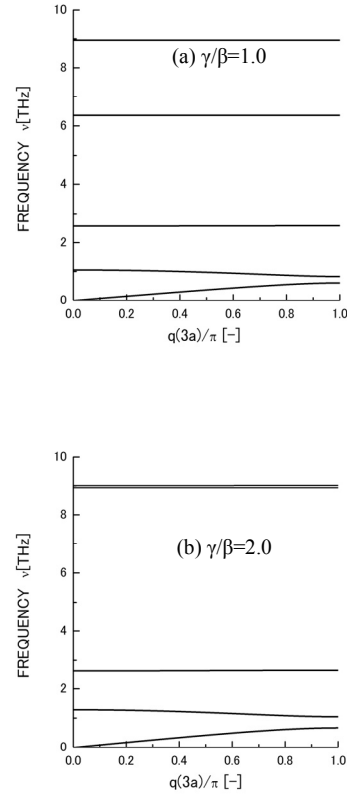


Fig. 8 Phonon dispersion curves for the partially reacted model A shown in Fig. 7. The wave number q is normalized by the size of the first Brillouin zone.

2.4 Partially reacted model B

Lastly, we consider another partially reacted model sketched in Fig. 9. This is an example where two of the four D ions react and a He and a D vacancy are produced. The vibration modes for this problem are characterized by 7×7 dynamical matrix. Therefore, it

has seven solutions.

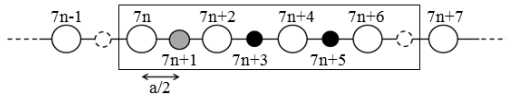


Fig. 9 Sketch of the partially reacted model B. Open circle with solid line means Pd and open circle with dashed line means D vacancy. Black circle means unreacted D. Gray circle means He which is produced by DD reaction.

Phonon dispersion relations for this model with $\gamma/\beta = 1$ and 2 are plotted in Fig. 10 (a) and (b), respectively.

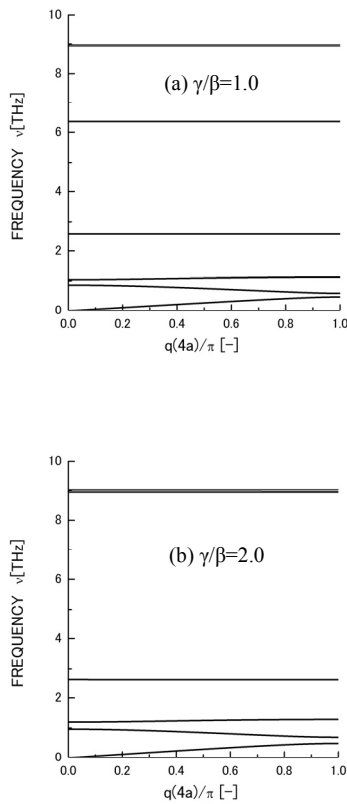


Fig.10 Phonon dispersion curves for the partially reacted model B shown in Fig. 9. The wave number q is normalized by the size of the first Brillouin zone.

In Figs. 6, 8 and 10, the highest and the second highest optical modes are slightly different from each other. They may be degenerate. Here we do not dwell on this problem, because they do not have any fundamental meaning in this problem. They may depend on the accuracy of the numerical calculations.

3 Conclusions

Assuming an interaction between ions in the lattice, we can calculate the phonon dispersion relation from the lattice structure. Conversely, we can draw the lattice structure from the experimental data of phonon dispersion relation. Furthermore, we can guess the interaction between ions from the distances between the branches. In this study, we showed possible change of phonon dispersion relation due to the nuclear reaction in solids by using one-dimensional lattice with nearest neighbor harmonic interactions. Therefore, if we see the same change of phonon dispersion relation, it can be analogized that the change happens as a result of the nuclear reaction in solid. The ground of this judgment is the number of branch, their type and the distances between branches. For example, nuclear reaction enlarges the primitive cell. This increases the number of the phonon dispersion branches.

In this study, we have tried the calculation within the one-dimensional approximation. As real reactions necessarily happen in the three-dimensional space, we plan to undertake three-dimensional calculations in future work. However, the one-dimensional study of the present work is thought to be the first step to show a new approach using phonon dispersion relations.

If we measure the phonon dispersion relation of palladium deuteride and find unknown extra dispersion branches, they may be evidences of nuclear reactions.

Acknowledgements

The authors wish to thank Professor Akito Takahashi of Osaka University and Professor Hiroshi Yamada of Iwate University for helpful discussions and encouragement. We also wish to thank Professor Noboru Akuzawa of TNCT for advice on the hydrogen storage techniques.

References

1. M.R. Chowdhury and D.K. Ross, Solid State Communication, **13**(1973)229
2. J.M. Rowe, J.J. Rush, H.G. Smith, M. Mostoller, and H.E. Flotow, Phys.Rev.Lett., **33**(1974)1297
3. K. Tsuchiya, S. Asano, M. Ozaki and S. Sasabe, Proceeding of JCF8, p1
4. K. Tsuchiya, A. Watanabe, M. Ozaki and S. Sasabe, Proceedings of ICCF14 (to be published)
5. K. Tsuchiya, Proceeding of JCF9, p80
6. K. Tsuchiya, S. Sasabe and M. Ozaki, Proceedings of ICCF15 (to be published)
7. K. Mohammed, M.M. Shukla, F. Milstein and J. L. Merz, Phys.Rev. B29 **6**(1984)3117

Simulation of Palladium Transmutation Products Using a Nuclear Lattice Model

Norman D. Cook
 Department of Informatics
 Kansai University
 Osaka, Japan

Abstract

The conventional independent-particle model (IPM) contains symmetries that are identical to the symmetries of a face-centered-cubic (fcc) lattice. That fact was pointed out by Wigner already in 1937! Using the lattice to simulate the fission of both Uranium and Palladium, the experimentally-known fission products are easily explained.

Introduction

In 1937, Eugene Wigner established the foundations of the independent-particle model (IPM) in a paper in *Physical Review* on the “symmetries of the nuclear Hamiltonian.” That work led directly to the quantum mechanical description of all *nucleon* states and all *nuclear* states, a description that has been used ever since in all modern versions of the microscopic shell model. Moreover, the establishment of the concepts of

the IPM led to three Nobel Prizes in 1961, which Wigner (50%) shared with the inventors of the shell model, Mayer (25%) and Jensen (25%). In the 1937 paper, Wigner noted explicitly that the nuclear Hamiltonian had the symmetries of a face-centered-cubic lattice (1937, p. 110). The quantal symmetries of the Schrodinger equation are in fact most easily understood in 2D patterns of nucleon states (Figure 1A), but the 2D layers, when stacked on top of one another form a unique 3D lattice (Figure 1B).

112 SYMMETRY OF NUCLEAR HAMILTONIAN

Fig. 1.

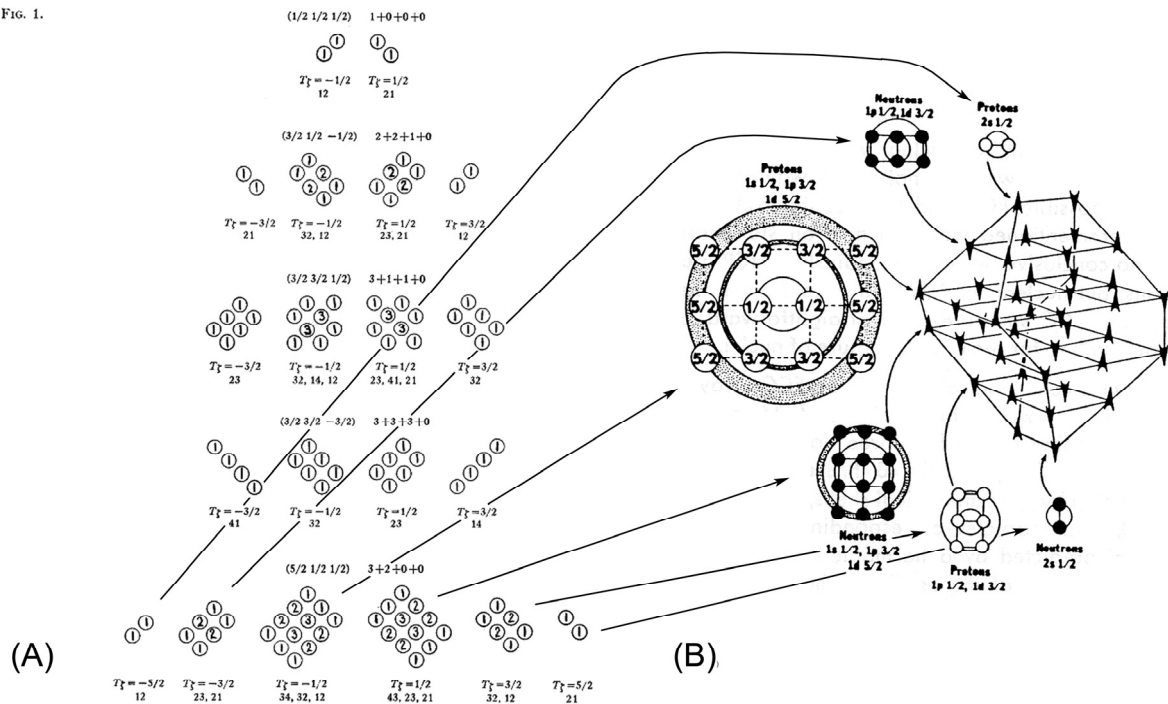


Figure 1: (A) Wigner’s 1937 depiction of the “layered” symmetries of the nuclear Hamiltonian for selected small nuclei, top to bottom: ${}^4\text{He}$, ${}^{16}\text{O}$, ${}^{28}\text{Si}$, ${}^{20}\text{Ne}$ and ${}^{40}\text{Ca}$. (b) The same symmetries in ${}^{40}\text{Ca}$, stacked into an fcc lattice, were published again in 1976 (Cook, 1976) and in many other works (e.g., Lezuo, 1974; Dallacasa, 1981; Cook & Dallacasa, 1987; DasGupta & Pan, 1996; Everling, 2006; Cook, 2006, 2010; etc.).

The fcc lattice has been developed into a comprehensive model of the nucleus and shown to contain: (i) geometrical shells and subshells at all of the n-shells and j-subshells of the IPM, (ii) a liquid-drop texture, implying nearest-neighbor nucleon-nucleon interactions (no fictitious “effective” central potential well), and (iii) tetrahedral subgroupings of nucleons identical to the cluster model.

Using the lattice model, we have previously shown that the oldest problem in nuclear theory – the explanation of the *asymmetry* of the fission fragments from Uranium and Plutonium – is easily resolved (Cook, 1999, 2006). Specifically, the fission of large nuclei is energetically most favored along oblique lattice planes with mass ratios of 3:2 (Figure 2). The liquid-drop model

incorrectly predicts symmetrical fragments (1:1) and the shell model incorrectly predicts the dominance of magic numbers 50 and 82 among fragments. Most textbooks *mistakenly* state that the shell model predicts fragment asymmetries, but the technical literature does not support that view (Brack et al., 1972; Vandebusch & Huizenga, 1973).

As illustrated in Figure 2, the approximate mass asymmetry (3:2) of the fragments from the actinides (Uranium, Plutonium and Californium) is obtained using the lattice model and, importantly, *without the use of any fission-related parameters*. This fact can be verified using the *Nuclear Visualization Software* (NVS), that is freely available for download at (Windows and Mac versions): <http://www.res.kutc.kansai-u.ac.jp/~cook>.

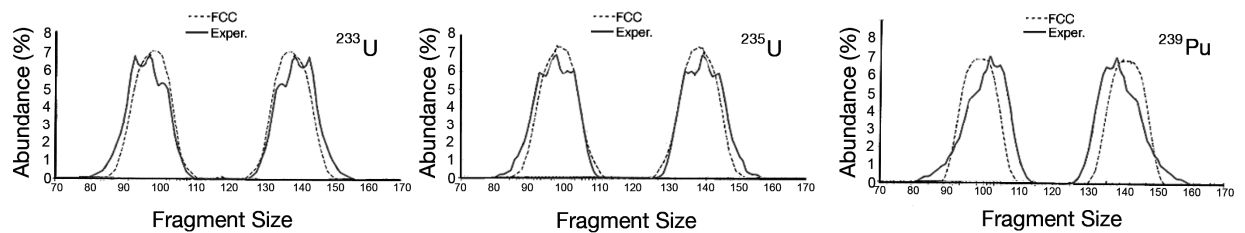


Figure 2: The parameter-less prediction of asymmetrical fragments in the thermal fission of the actinides using the lattice model (Cook, 1999, 2006, 2010). The experimental data are shown by the solid lines, the theoretical predictions are the dotted lines. (Note that there is *real* substructure in the experimental curve that survives the fission process; none of the peaks coincide with magic numbers).

Transmutation of Palladium

I have previously reported that the changes in isotopic percentages on the surface and in the depth of the Palladium cathode, as reported by Mizuno, are reproduced in a model-independent simulation (Cook, 2009). The agreement between the Mizuno data and the

simulation results clearly indicates the self-consistency of the experimental data and the strong likelihood that all of the Palladium isotopes are equally involved in transmutation. If a constant percentage of surface Pd isotopes are transmuted in LENR experiments, the next question is: what are they transmuted to?

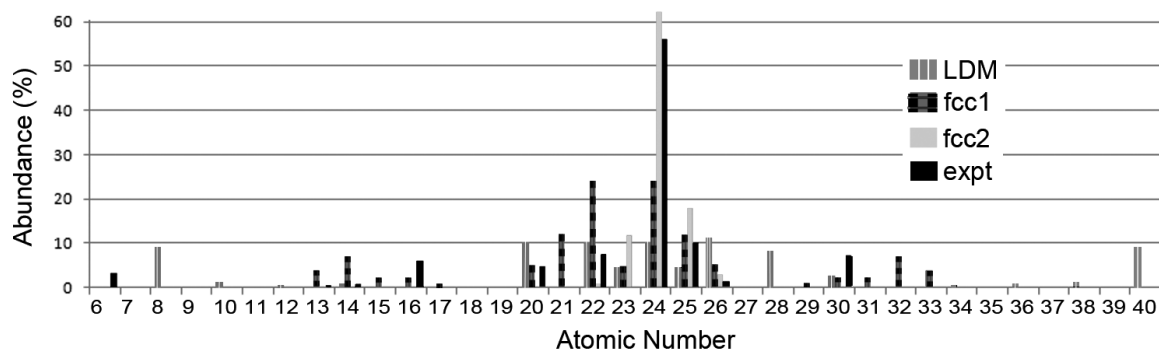


Figure 3: A comparison of Pd fission fragment data and three simulations. The experimental data from Mizuno (1996) (black bars) show the predominance of Chromium deposits on the Palladium cathode. A conventional liquid-drop model (LDM) calculation predicted a roughly symmetrical distribution around $Z=24$, but with no Chromium peak (Ohta & Takahashi, 2003) (white-stripe bars). The first fcc lattice simulation (fcc1) produced a symmetrical distribution around $Z=23$ with a slight over-abundance of Ti and Cr, prior to de-excitation of fragments. The second simulation (fcc2) using a narrower range of lattice randomizations produced a peak of Chromium, following de-excitation of fission fragments (light grey bars).

Palladium Fission Fragments

Simulation of the fission of Palladium was carried out on each of the six stable Pd isotopes using the lattice model. The nucleon build-up process is that known from the standard IPM and the lattice coordinates of each nucleon are given by the mathematical identity between the IPM and the fcc lattice. However, the lattice positions of equivalent nucleons (i.e., nucleons whose n - and j -value are the same, but the fcc lattice positions vary) we selected randomly, and influenced only by the maximization of nearest-neighbor interactions, while minimizing Coulomb repulsion. In other words, 46 protons and 56~64 neutrons were placed at fcc lattice sites, such that the final structure has (i) maximal nearest-neighbor binding, (ii) minimal Coulomb repulsion, and (iii) a total J -value (calculated from the sum of nucleon j -values) as experimentally known. Scission of the $Z=46$, $N=56\sim 64$ system was then simulated along 17 principal lattice planes cutting through or parallel to the origin of the coordinate system, and statistics collected (Figure 4).

For each scission plane, the total number of 2-nucleon “bonds” crossing the scission-plane was counted and the

total Coulomb repulsion between the fragments was calculated. Assuming an average nearest-neighbor binding energy of ~ 2.73 MeV (ignoring spin and isospin effects) (thus giving total binding energies of the Pd isotopes within 0.1% of experimental values) and subtracting the Coulomb effect between the fragments, the fission barriers for 17 fission events per isotope were calculated. The simulation was then repeated for different (but equivalent) occupancy of surface neutron sites. Finally the data on fission fragments per Pd isotope were collated. The entire procedure for simulating the fission of Palladium is similar to that already reported concerning the actinides (Cook, 1999), and can be easily reproduced using the same software (NVS) that demonstrates the asymmetrical fission of Uranium and Plutonium. Examples of fission planes for Pd^{104} are shown in Figure 4.

It is worth noting that the rigid crystal structures shown in Figure 4 are merely snapshots of a dynamic quantum lattice, in which meson exchanges change the isospin assignment of lattice sites, and all valence positions are repeatedly occupied and vacated, as the system settles into an energetically favored state.

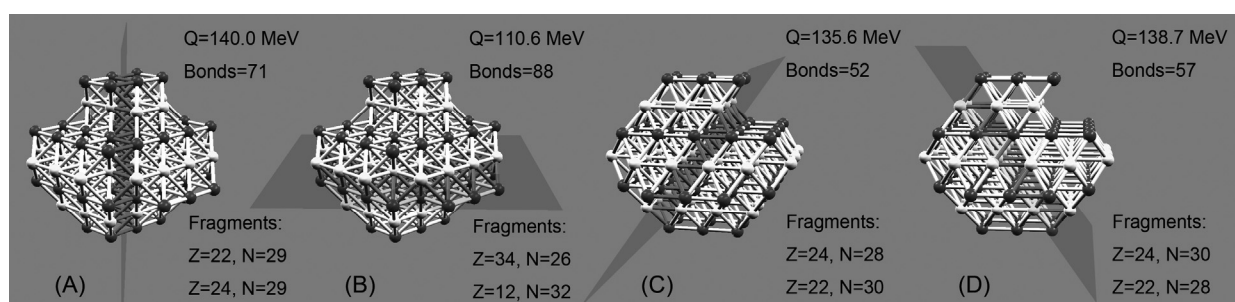


Figure 4: Examples of high fission-barrier (A, B) and low fission-barrier (C, D) lattice scission planes for Pd^{104} . Note that the fcc lattice structures represent individual nuclei (protons are light spheres, neutrons are dark spheres), unrelated to the fcc (atomic) structure of the Palladium cathode itself. Most of the low fission-barrier fragments are stable or rapidly decay to stability.

Results

By calculating the total binding energy across each scission plane minus the Coulomb repulsion between the protons in each fragment, the energy required to induce fission was found to be 1.57~11.73 MeV, depending on the specific isotope and lattice plane. The fragments produced by splitting the Pd isotope along the low-energy planes contained 48~60 nucleons and 22~24 protons. Specifically, the lowest energy fission products per isotope were: Pd^{102} (2.44 MeV) \rightarrow Cr^{48} & Ti^{54} ; Pd^{104} (2.25 MeV) \rightarrow Cr^{50} & Ti^{54} ; Pd^{105} (7.30 MeV) \rightarrow Cr^{50} & Ti^{55} ; Pd^{106} (1.95 MeV) \rightarrow Cr^{52} & Ti^{54} ; Pd^{108} (1.57 MeV) \rightarrow Cr^{52} & Ti^{56} ; and Pd^{110} (11.73 MeV) \rightarrow Cr^{54} & Ti^{56} . Most fragments are stable, with a predominance of Cr

and Ti, sometimes decaying to Mn, Fe, etc. In other words, the fission of Palladium was essentially symmetrical ($Z=22\sim 26$) with two daughter fragments of approximately the same mass. Generally, only a few scission planes per isotope had fission barriers below 10 MeV, but a higher fission barrier produces fragments with atomic number 14~32 and mass number 34~72. Qualitatively, the spectrum of deposits on Pd as reported by Mizuno (1998) was reproduced by the lattice model.

Conclusion

The asymmetrical fragmentation of U^{235} and all of the other actinides that undergo thermal fission is one of the oldest, unsolved problems in conventional nuclear

physics. Despite the success of the LDM in explaining the energetic basis of fission, extremely precise structural data are available and have remained, since 1938, unexplained using the conventional models of nuclear structure theory.

In the realm of research on LENR, a similar dilemma exists. Since 1989, heat generation that cannot be explained on a chemical basis and precise data on isotopic changes have been demonstrated experimentally many times, but structural mechanisms concerning transmutation of nuclear species have remained elusive.

Conventional nuclear structure theorists are understandably reluctant to postulate new physical mechanisms to account for the transmutation results in both thermal fission and LENR, but the isomorphism between the conventional IPM and the fcc lattice model suggests a way forward that is less revolutionary in terms of nuclear structure theory than it may at first appear to be. Both the mystery of asymmetric fission of Uranium and the mystery of the transmutation of Palladium have apparent solutions if the nucleus itself is regarded as a quantum lattice that reproduces the shell/subshell structure inherent to the independent-particle (~shell). Assuming a yet-uncertain energetic mechanism for inducing the fission of Pd nuclei, the substructure implicit to the fcc lattice representation of nuclear symmetries appears to explain transmutation results essentially without any modification to the conventional theory of nuclear structure.

I therefore encourage all nuclear theorists to examine the fcc lattice model – particularly in order to understand its implications with regard to low-energy “cold fusion” phenomena. The lattice model is of course conceptually very different from the gaseous-phase independent-particle model, but, as has already been shown by many of us, the symmetries of the antiferromagnetic fcc lattice with isospin layering (Canuto & Chitre, 1974) are identical to the symmetries of conventional nuclear theory. The lattice model, however, also has structural implications due to the lattice geometry.

References

- Brack, M., Strutinsky, V., et al. (1972) *Reviews of Modern Physics* 44, 320.
- Canuto, V., & Chitre, S.M. (1974) *International Astronomical and Astrophysical Union Symp.* 53, 133.
- Cook, N.D. (1976) *Atomkernenergie* 28, 195.
- Cook, N.D. (1999) *Proceedings of the St. Andrews Conference on Fission*, pp. 217-226.
- Cook, N.D. (2006/2010) *Models of the Atomic Nucleus: Unification through a lattice of nucleons*, Springer, Berlin.
- Cook, N.D. (2009) Simulation of transmutation products on Palladium cathodes. *JCF9*, Shizuoka, March 2009.
- Cook, N.D., & Dallacasa, V. (1987) *Physical Review C* 36, 1883-1891
- Dallacasa, V., *Atomkernenergie-Kerntechnik* 37, 143, 1981.
- DasGupta, S., & Pan, J., *Physical Review C* 53, 1319, 1996.
- Everling, F., *Journal of the Physical Society of Japan* 75, 124201, 2006; <http://everling-nuclear-lattice-model.com>
- Lezuo, K., *Atomkernenergie* 23, 285, 1974.
- Mizuno, T. (1998) *Nuclear Transmutation*, Infinite Energy Press, Concord, NH.
- Ohta, M. & Takahashi, A. Analysis of nuclear transmutation induced from metal plus multibody-fusion-products reaction. In, *Tenth International Conference on Cold Fusion*. Cambridge, MA: LENR-CANR.org, 2003.
- Vandenbosch, R. & Huizenga, J.R. (1973) *Nuclear Fission*, Academic, NY, p. 273.
- Wigner, E., *Physical Review* 51, 106, 1937.

Cellular automata numerical simulation of cascade vortices

Hiroo NUMATA¹ and Masanobu.BAN²

¹Tokyo Institute of Technology, 2-12-1, O-okayama, Meguro Tokyo 152-8552 Japan

E-mail: numata.h.aa@m.titech.ac.jp

²Tokyo Metropolitan Leather Technology Center, 3-13-14, Higashi Sumida, Sumida Tokyo 131-0042 Japan

Abstract: In our previous work, we have performed numerical simulation for the analysis of the vortex patterns on the postelectrolysis Pd rod and successfully obtained them within the rectangular domain using hydrodynamics for the incompressive fluid. In this work, we have improved the prototype calculation by using the following new concepts. Firstly, robust boundary condition was adopted. Secondly, cascade vortices were simulated by using combined vessels, where the fluid moved from one to the neighboring one. Finally, the vortex thread in 3D space was analyzed. As a result, the flow pattern from one vessel to neighboring one was obtained. This will contribute to know the physical properties of the hypothetical particles mass relating to the CF anomaly, e.g. high/low energy process, traces of local energy deposition and so on.

Keyword: Computational fluid dynamics, Lattice gas cellular automata, Pd, Nuclear reaction cycle model, vortex-thread

1 Introduction

During long-term electrolysis for well annealed thick Pd rod (9.0 mm ϕ) in 0.1M LiOD, vortex pattern was observed¹⁻²⁾. The morphology of the postelectrolysis electrodes revealed the two long faults without any cracks on the surface. The original work of the modified cellular automata (numerical simulation) method had been first applied by Numata et al. to the study of the cold fusion and related phenomena.³⁻⁶⁾ Our research goal is to give an atomistic understanding of the phenomenon that the vortex occurred on a Pd electrode surface after long-term electrolysis in 0.1 M LiOD. Firstly, this vortex pattern was successfully formed by FHP-III model of Lattice Gas Cellular Automata (LGCA or CA) numerical simulation of the motion of the hypothetical particles mass. Then it was proved that the hypothetical particles mass flows coincidentally through the electrode surface/electrolyte interface under the influence of heterogeneous induced magnetic field in the vicinity of the electrode surface area.³⁾ Secondly, Sommerfelt's radiation condition for the Outflow boundary condition was found to be most appropriate one in a 2D flow.⁶⁾

Instead of the Quantum mechanical realization of cold fusion process, the work has found the microscopic mechanism: how the hypothetical particles mass with significant kinetic energy moved and has left the vortices on the sample surface.³⁾ However, the flow patterns were still ambiguous in that work.

To improve this simulation model for the vortex pattern on the postelectrolysis electrode, this work is directed toward the advanced LGCA simulation model: the cascade of the vortices (vortex-thread).

2 Experimental

2.1 Improved CA Simulator for numerical simulation

As an integrated CA simulator, we have made LGCA programs running on the Linux platform. The other experimental procedures are similar to those described in previous papers.³⁻⁶⁾ PC details are; PC machine: Compac 8510W, CPU: Intel Core2 Duo, Clock: 2.4GHz, OS: CentOS5, Mem.:4GB, Compiler: Intel Compiler 11.1 and Graphics: Gnuplot.

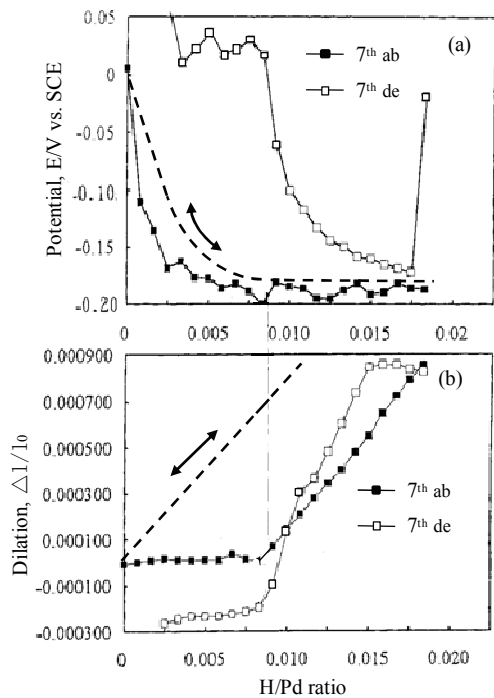
The CA simulation program: LGROTATE modified by parallelization was run under different number of PC core to evaluate the computational speed of the incompressive fluid analysis code. In this experimental series CA simulation environment should be kept at satisfactorily level, e.g. CPU clock, memory size, core number, compiler and so on.

3 Results and Discussion

3.1 Previous experimental result for N-cycle model

We have investigated the microscopic structural change of a Pd electrode during repeated hydrogen absorption/desorption by electrolysis. Especially the following question was addressed How does hydrogen absorption/desorption proceed accompanied with the lattice expansion/contraction and the specimen lead to discrimination of sub-surface layer and bulk?

The experiments of in situ potentiometric, resistance and dilatometric measurements were performed using a modified three-electrode cell described previously.⁷⁾ Figs. 1(a) and (b) show the electrode potential and dilation changes as a



Figs.1 (a) and (b) Comparison of potential: (a) with dilation: (b) as a function of H/Pd ratio at 40°C. In both figures filled and open squares denote absorption and desorption runs, respectively. Dotted lines in both Figs. denote the plots of potential and dilation assuming the Nernstian behavior and equilibrium absorption and desorption.

function of H/Pd ratio for the 7th absorption/desorption cycle. The electrode potential E for Pd is given by the Nernst equation

$$E = E^{\circ} - RT/F \ln(a_{H_{ad}}) - 0.248 \quad [V] \quad (1)$$

where $a_{H_{ad}}$ is the activity of adsorbed H and the other symbols have their usual meanings.

In Fig.1(a), the dotted line shows the Nernstian plot of α -single and $\alpha + \beta$ phases. In this case $a_{H_{ad}}$ in eq.(1) is replaced by $a_{H_{ab}}$ which means the activity of adsorbed H. Since the activity coefficient of $a_{H_{ab}}$ equals 1 within these dilute solutions, H/Pd ratio as the adsorbed H concentration is conveniently used here. In Fig.1(a), that is, after 7 absorption/desorption cycles the electrode potential tends to attain quickly that of $\alpha + \beta$ coexistence phases from the initial potential, showing a significant deviation from the Nernstian plot. This behavior inconsistent with an equilibrium process was explained by the evolution of sub-surface layer containing the formerly formed phases, and hence the coexistence region was attained at a relatively low H/Pd ratio. In previous study, the schematic model of Pd rod with discriminated sub-surface layer (denoted as surface volume in the figure) and remaining bulk, which is subjected to several absorption/desorption cycles, was proposed. It is shown in Fig.2. In this model, it is assumed that

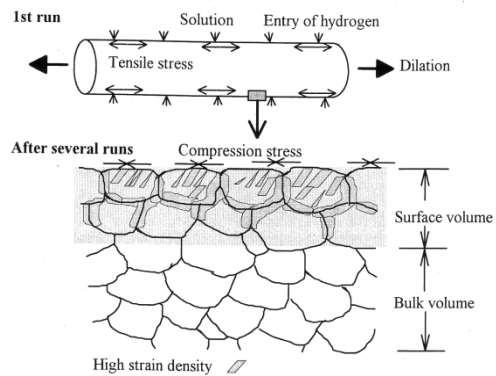


Fig.2 Schematic of discrimination of sub-surface and bulk volume and state of surface stress during hydrogen absorption and desorption cycles.

the sub-surface layer exist under the strong axial compression stress, which is preferentially subjected to heavy strain during the early stage of absorption/desorption cycle. During desorption subsequent to absorption, the potential change as a function of H/Pd ratio exhibits the $\alpha + \beta$ coexistence region at -0.17V, followed by the first recovery of the potential toward 0.025V. This corresponds to the fully desorbed phase.

On the other hand, as shown in Fig.1(b), the dilation change as a function of H/Pd ratio during absorption shows that an induction period whereupon the α single phase might exist. This non-equilibrium phenomenon was explained by introducing the transition of the order-disorder α phase and the progressive spreading of strain volume: α phase with H orderly distributed.⁷⁾

More comprehensive explanations of this in situ measurement have proven that (see Fig.2)

- Sub-surface layer does not respond to the dilation, which might be termed a “dashpot effect” parallel combined to harmonic oscillator in the dynamic motion system.
- Remaining bulk responds directly to the dilation subsequent to an induction period. Thus, the sub-surface layer is constrained by the bulk and develops compression stress.

In Fig.1 (a) and (b), during desorption the potential stays at -0.17V, during which the dilation terminates for a short period, and then a decrease of the dilation occurs accompanied with the transition of the potential from -0.17V to 0.025V. When the contraction finishes, the potential reaches to 0.025V of the fully desorbed phase. It is noted that during absorption non-equilibrium phenomenon at the dilation is attributable to the bulk accompanied with the strained sub-surface layer, while during desorption the incomplete sub-surface layer somewhat retards the dilation change and makes desorption proceed easily. The above discussion

sufficient energy where the motion of the flows are expressed as 'simulate flow' vectors normal to the electrode interface as shown in the right. Furthermore all the flows synchronize with the occurrence of the reaction. It is tentative understanding how such flows (composed of hypothetical particles mass) gain considerable amounts of energy. However, the fusion energy might be transferred to deuterons, and then the particles mass near the reaction sites becomes high pressure. Thus, the motion occurs explosively surrounding 360° of the reaction sites. In addition obstacles might be embedded beneath the surface due to structural inhomogeneity. The precipitates such as PdO, Li₂O and LiD, and /or vacancy cluster can correspond to actual structural homogeneity. These obstacles, which are modified as a flat plate set in the latter simulation domain (see Fig.7) play an important role in the formation of vortex. Thus, N-cycle model predicts that the flows occur coincidentally through the electrode/electrolyte interface (above shown in Fig.4 as the motion of reaction products and deuterium to neighboring vessels:② and/or surface of the electrode:①). However, the above is merely hypothesis, that is, the experimental observations have not yet been elucidated, and then numerical simulation of the fluid might be substantiate N-cycle model.

3.3 Numerical simulation for the motion of the hypothetical particles mass

Since N-cycle model predicted the hypothetical particles mass explosively spouted out from the deuterated Pd surface after long-term deuterium evolution, it is required to simulate the vortex pattern on the Pd surface by computer simulation. In Scavenger process of Fig.4 there appeared alternative two mechanisms of the hypothetical particles mass motions. Firstly, Fig.5① shows the locus of the occasional particle flow on the Pd surface named vortex. Previous report³⁾ mainly concerned with the morphological identification of the vortex (single vortex) comparing the experimental and 2D LGCA theoretical patterns. (see the upper of Fig.5) The more detailed interaction between the motion of the hypothetical particles mass and the interface magnetic field is skipped in this context.³⁾

Secondly, Fig.5② shows the continuous flow of hypothetical particles mass from a vessel to a neighboring one. It has been suspected that the particles mass also has the vortex pattern at the electrode surface. And, a reasonable inference leads conclude us that the vortex occurred occasionally, while the cascade vortices: vortex-thread moves underneath the electrode surface. This view might not be inconsistent with the irregularity of sub-surface layer under an annealing at 1100°C. In the lower of Fig.5 the evolution of consecutive vortex-thread underneath electrode surface is schematically drawn during long-term evolution of deuterium.

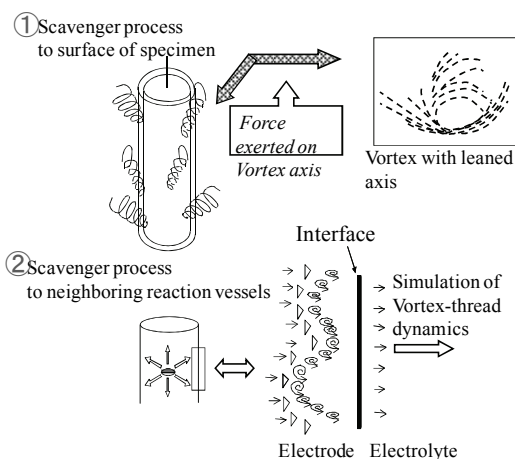


Fig.5 Schematics of vortex with leaned axis and vortex thread during Scavenger process: motion of hypothetical particles mass from vessel to surface and from a vessel to a neighboring one.

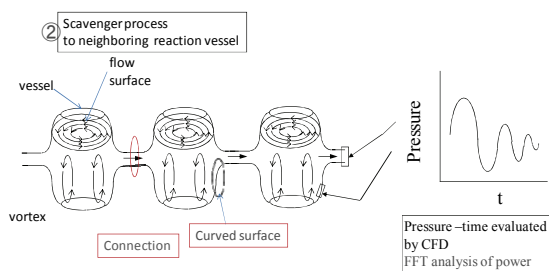


Fig.6 Cascade of n-vortices: vortex thread model for CFD. The inset shows time evolution of pressure evaluated by CFD.

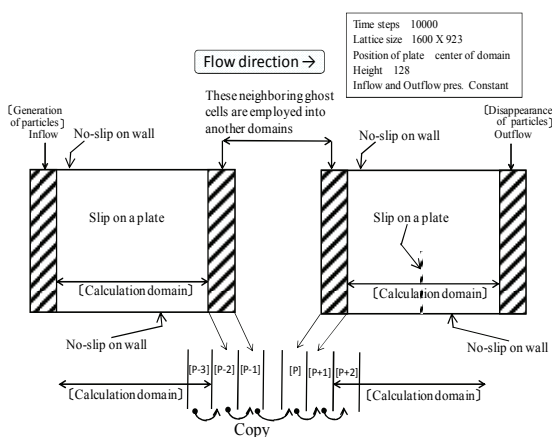
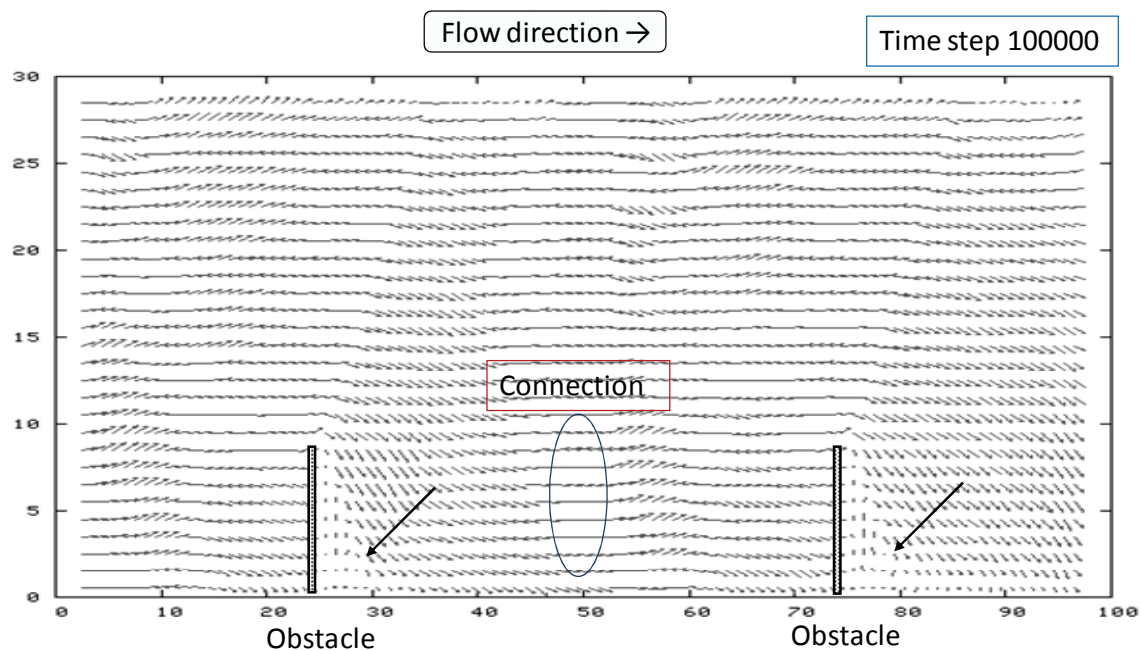


Fig.7 Cascade of vortices: vortex thread model.



Connected two vessels

Fig.8 LGCA simulation result of vortices evolved behind plates on 4640x1152 grids at Time step=100000.

For preliminary work at first, a vessel is defined to validate the cascade of vortex model, where artificial trigger¹²⁾ starts the turbulent flow of a vortex. In Fig.4 the possible two types of triggering: external and internal are shown together with the vessel exhibiting turbulence therein. For simulating the dynamics of the cascade of vortices (i.e. vortex-thread) the characteristics of the fluid has been analyzed using commercial 2D CFD. (Computational Fluid Dynamics, e.g. FLUENT) The single vortex in a vessel: prototype of cascade model revealed the turbulence and convection due to the centripetal and induced centrifugal forces involving the pressure (fluid velocity) variation with time. This simulation model of the single vessel with free surface can be extended to 2D cascade of n-vortices as shown in Fig.6.xxxxxxxxxx

Next our approach is addressed to the followings,

- More useful CA simulator for the cascade of vortices as a first approximation
- Physics of fluid, e.g. density, viscosity, velocity and superconductivity state around vortex-thread

Hereafter, the CA simulation of two connected vortices as the first step for n-cascade vortices is described again. As shown in Fig.7 a 2D incompressible fluid lattice gas cellular automata is constructed on a simulating space (two identical rectangular domains) where regular triangular lattices with unit link length are mapped and discredited on the whole. These configuration and the boundaries are essentially

identical to those reported previously except that the connection region is introduced into the model by two ghost cells. Two ghost cells of first rectangular domain are employed to second domain by copying. Inspecting the fluid flow vectors in the connection region, there obtained the fluid motion transferred during simulation time was prolonged.

Figure 8 shows a simulated fluid flow behind obstacles (flat plate) at Time step = 100000 by using FHP III model in two consecutive rectangular domains. The parameters used are shown in the upper of Fig.7. In Fig.8 an arrow shows an individual velocity vector, which length and direction correspond to an averaged velocity and direction, and so macro flow pattern is visually understandable. The vertical and horizontal axes are of hexagonal coordinate system. In the calculation, time step means accumulated time step. The stationary flow from left to right is given by the pressure difference of the Inflow and Outflow boundary regions. In this calculation Sommerfeld's radiation condition was applied.¹³⁾ As shown in Fig.8 the stationary flow creates two vortices (shown by arrows) behind flat plates. It is suggested that many connected vessels creating an individual vortex can be extended to 3D space to analyze the real phenomenon occurred on the postelectrolysis electrode.

4 Conclusion

In the cold fusion experiment, there observed vortex patterns on thick Pd electrode surface during long-term electrolysis in LiOD. To

understand the peculiar phenomenon we had proposed N-cycle model, which is composed of 4 sequential processes including CF reaction.

Prior to CF reaction, sub-surface layer and structural homogeneity (originated from impurity) are formed according to the sample preparation procedure. Since the vortices might be formed by CF reaction, this time LGCA numerical simulation was performed. By advanced CA simulation model: cascade of vortices flow pattern of the hypothetical particles mass visualized connected two vortices behind flat plate as obstacles. In addition the hitherto solved phenomenon and present issues were shortly reviewed.

Acknowledgement

This work is partially supported by Shogaku-kihukin of our institute provided by C.S.S. Co., Ltd.

References

- 1) H. Numata et al.: Proc. Conf. Science of Cold Fusion, Vol.33, pp.71, T.BRESSANI et al. eds., SIF, Bologna, Italy (1991)
- 2) R. Takagi et al.: Fusion Technol., **19** (1991)2135
- 3) H. Numata and M. Ban: Proc. ICCF12, Yokohama, pp.411-420 (2005)
- 4) H. Numata and M. Ban: Proc. JCF6, pp.32 (2005)
- 5) H. Numata and M. Ban: Proc. JCF8, pp.67 (2008)
- 6) H. Numata and M. Ban: Proc. JCF9, pp.74 (2009)
- 7) H. Numata and M. Ban: Proc. JCF7, pp.6 (2006)
- 8) H. Numata: in book "Cyber X" No.11, pp.37 (1999) Kougakusha.
- 9) A. Takahashi et al.: "Nuclear Reaction Study In Condensed Matter No.1", Chapter 4, pp.124, 1999 Kougakusha.
- 10) H. Numata and I. Ohno: Fusion Technol., **38** (2000)206
- 11) H. Numata and I. Ohno: ICCF6, Toya Japan, vol.1, pp.213(1997)
- 12) It is tentatively said that stepwise pressure wave is used here as trigger by the limitation of CA rule.
- 13) Yoshida et al.: Trans. JSME, **61-588, B**, 2887(1995)

Abraham-Lorentz-Dirac Equation in Quantum Mechanics: The Beginning of Weakened Coulomb Potential

Shigeru Sasabe (Tokyo Metropolitan University) s-sasabe@tmu.ac.jp

Masao Ozaki (Tokyo University of Agriculture) mlozaki@nodai.ac.jp

Abstract: A weakened Coulomb potential was suggested to overcome the Coulomb barrier between deuterons in palladium. The derivation of weakened Coulomb potential is based on the nonrelativistic limit of the Lorentz-Dirac equation, which is called the Abraham-Lorentz (AL) equation. Although the validity of the AL equation was proved by Italian researchers¹⁾ about half a century ago, it is not so familiar to most of physicists and their scheme was fairly complicated. Using Crisp's method, we have derived the AL equation from quantum mechanics by means of Ehrenfest's theorem in rather simple way. It is found that the dipole approximation is essential to obtain the AL equation.

Keywords: Abraham-Lorentz-Dirac Equation, Quantum Mechanics, Cold Fusion

1. Introduction

The Coulomb barrier between two deuterons is one of the most difficult problems to achieve the nuclear fusion in the solid. It is necessary to explain why deuterons is able to overcome Coulomb barrier in order to make a lot of physicists' consent. One of the present authors suggested a weakened Coulomb potential that was derived naturally as an effect of the self-field of the charged particle²⁾. The weakened Coulomb potential,

$$V(r) = \frac{e^2}{r} \left[1 - \exp\left(\frac{-r}{\sqrt{2}R_c}\right) \times \cos\left(\frac{r}{\sqrt{2}R_c}\right) \right], \quad (1)$$

involves some characteristic length R_c which is supposed to depend on electromagnetic property of the solid. The value of R_c is

$$R_c = 0.5 \times 10^{-15} \text{ cm} \quad (2)$$

for deuteron in vacuum, so that R_c is too small to give any effect for the nuclear reaction. Then, R_c in eq.(1) has no effect in vacuum, and we can neglect it in eq.(1). The weakened Coulomb potential accords with the original Coulomb potential in this case. The value of R_c may change into large one if the charged particles are immersed in some kind of solid. Making use of eq.(1), some estimation for larger value of R_c than eq.(2) shows that the tunneling probability of deuteron improves drastically for the Coulomb barrier³⁾. The derivation is based on the energy

balance of non-relativistic limit of the Lorentz-Dirac equation called Abraham-Lorentz equation. Therefore, it is a significant problem for the validity of the weakened Coulomb potential whether the Abraham-Lorentz equation consists with the quantum theory.

2. Derivation of Abraham-Lorentz Equation⁴⁾

We derive the Abraham-Lorentz equation using Neoclassical theory (NCT). NCT is a semiclassical theory which assumes an unquantized radiation field interacting with an electron obeying the law of quantum mechanics,

$$i\hbar \frac{\partial \psi}{\partial t} = H\psi \quad (3)$$

with the Hamiltonian

$$H = \frac{1}{2m_0} \left(\mathbf{p} - \frac{e}{c} \mathbf{A} \right)^2 + e\phi + U, \quad (4)$$

where m_0 is a bare mass of the electron, In the Coulomb gauge, the vector and scalar potentials are expressed in terms of the retarded vector potential and the instantaneous scalar potentials, respectively.

$$\mathbf{A}(\mathbf{r}, t) = \mathbf{A}_s(\mathbf{r}, t) = \frac{1}{c} \int d^3\mathbf{r}' \frac{\mathbf{J}_t(\mathbf{r}', t - (R/c))}{R}, \quad (5)$$

$$\phi(\mathbf{r}, t) = \phi_s(\mathbf{r}, t) = \int d^3\mathbf{r}' \frac{\rho(\mathbf{r}', t)}{R}, \quad (6)$$

where $R = |\mathbf{r} - \mathbf{r}'|$, \mathbf{J}_t is a transverse part of the current density, \mathbf{J} , and the suffix 's' designates self-fields. Here, free fields, solutions of

the homogeneous field equation, are discarded, because we concentrate on the reaction on the particle of its own radiation field. The source current density \mathbf{J} and the charge density ρ in the integral of eqs.(5) and (6) may be measurable quantities because they are directly connected with the measurable electric field \mathbf{E} and magnetic field \mathbf{B} through the Maxwell equation. NCT provides

$$\rho(\mathbf{r}, t) = e\psi^*(\mathbf{r}, t)\psi(\mathbf{r}, t), \quad (7)$$

$$\mathbf{J}(\mathbf{r}, t) = Re \left[\frac{e}{m_0} \psi^* \left(\mathbf{p} - \frac{e}{c} \mathbf{A} \right) \psi \right]. \quad (8)$$

In NCT, ρ and \mathbf{J} given by eqs.(7) and (8) are assumed to be an actual charge density and an actual current density as source terms in the field equations. The self-field solution \mathbf{A}_s originated from the source current density can be expanded in powers of $1/c^5$, because the charged particle is highly localized.

$$\mathbf{A}_s(\mathbf{r}, t) = \frac{1}{c} \int d^3\mathbf{r}' \frac{\mathbf{J}_t(\mathbf{r}', t)}{R} - \frac{2e}{3c^2} \frac{d\langle \mathbf{v} \rangle}{dt}, \quad (9)$$

where, we neglected the terms of order of $1/c^3$ and higher, and used an expectation value of the velocity operator,

$$\mathbf{v} = \frac{1}{m_0} \left(\mathbf{p} - \frac{e}{c} \mathbf{A} \right) \quad (10)$$

and a relation,

$$\begin{aligned} \int d^3\mathbf{r} \mathbf{J}(\mathbf{r}, t) &= e \int d^3\mathbf{r} \psi^*(\mathbf{r}, t) \mathbf{v} \psi(\mathbf{r}, t) \\ &= e \langle \mathbf{v} \rangle \end{aligned} \quad (11)$$

The self-field solution ϕ_s is also expressed by

$$\phi_s(\mathbf{r}, t) = e \int d^3\mathbf{r}' \frac{|\psi(\mathbf{r}', t)|^2}{R}. \quad (12)$$

The Heisenberg equation of an electron with the Hamiltonian (2) gives the equation of motion,

$$m_0 \frac{d\mathbf{v}}{dt} = e \left(-\nabla\phi - \frac{1}{c} \frac{\partial \mathbf{A}}{\partial t} \right) - \nabla U. \quad (13)$$

The magnetic force has been neglected in eq.(13) because it is lower order of $1/c$ than the electric force in general. The expectation value of the above equation is

$$\begin{aligned} m_0 \frac{d\langle \mathbf{v} \rangle}{dt} &= -e \langle \nabla\phi_s \rangle - \frac{e}{c} \frac{\partial \langle \mathbf{A}_s \rangle}{\partial t} \\ &\quad + \langle \mathbf{F}_{ext} \rangle \end{aligned} \quad (14)$$

where, $\mathbf{F}_{ext} = -\nabla U$, and provided that we consider only the self-field of the electron besides external potential $U(\mathbf{r})$. We will reduce eq. (13) to

the nonrelativistic Lorentz-Dirac equation. Using eq. (9), we divide the vector potential part of eq. (13) to two terms,

$$\begin{aligned} m_0 \frac{d\langle \mathbf{v} \rangle}{dt} &= -e \langle \nabla\phi_s \rangle \\ &\quad + \mathbf{F}_J + \frac{2e^2}{3c^3} \frac{d^2 \langle \mathbf{v} \rangle}{dt^2} \\ &\quad + \langle \mathbf{F}_{ext} \rangle. \end{aligned} \quad (15)$$

The first term $-e \langle \nabla\phi_s \rangle$ of eq. (15) is the force coming from the self-Coulomb potential,

$$\begin{aligned} -e \langle \nabla\phi_s \rangle &= e^2 \iint d^3\mathbf{r} d^3\mathbf{r}' |\psi(\mathbf{r}, t)|^2 \\ &\quad \times \frac{(\mathbf{r} - \mathbf{r}')}{|\mathbf{r} - \mathbf{r}'|^3} |\psi(\mathbf{r}', t)|^2. \end{aligned} \quad (16)$$

Clearly, the exchange of \mathbf{r} for \mathbf{r}' reverses the sign of the above equation, so that $-e \langle \nabla\phi_s \rangle = 0$. The force \mathbf{F}_J coming from the first term of eq.(9) can be divided into two parts,

$$\mathbf{F}_J = \mathbf{F}_{Ja} + \mathbf{F}_{Jb}, \quad (17)$$

using a relation

$$\mathbf{J}_t = \mathbf{J} - \mathbf{J}_\ell, \quad (18)$$

where \mathbf{J}_ℓ is the longitudinal part of \mathbf{J} . The expression of \mathbf{F}_{Jb} is then given by

$$\begin{aligned} \mathbf{F}_{Jb} &= \frac{e}{c^2} \iint d^3\mathbf{r} d^3\mathbf{r}' \frac{|\psi(\mathbf{r}', t)|^2}{R} \frac{\partial \mathbf{J}_\ell(\mathbf{r}, t)}{\partial t} \\ &= \frac{e}{2\pi^2 c^2} \int \frac{d^3\mathbf{k}}{k^2} \int d^3\mathbf{r}' |\psi(\mathbf{r}', t)|^2 e^{-i\mathbf{k} \cdot \mathbf{r}'} \\ &\quad \times \frac{d}{dt} \int d^3\mathbf{r} e^{i\mathbf{k} \cdot \mathbf{r}} \mathbf{J}_\ell(\mathbf{r}, t), \end{aligned} \quad (19)$$

where the identity

$$\frac{1}{R} = \frac{1}{2\pi^2} \int \frac{d^3\mathbf{k}}{k^2} \exp[i\mathbf{k} \cdot (\mathbf{r} - \mathbf{r}')] \quad (20)$$

has been used. Further, we notice the identity for \mathbf{J}_ℓ ,

$$\begin{aligned} \mathbf{J}_\ell &= \frac{1}{(2\pi)^3} \int d^3\mathbf{k} \frac{\mathbf{k}}{k} \left[\frac{\mathbf{k} \cdot \mathbf{J}(\mathbf{k}) \exp(i\mathbf{k} \cdot \mathbf{r})}{k} \right] \\ &= -\frac{1}{4\pi} \int d^3\mathbf{r}' \nabla \cdot \left\{ \nabla \cdot \left[\frac{\mathbf{J}(\mathbf{r}', t)}{|\mathbf{r} - \mathbf{r}'|} \right] \right\}, \end{aligned} \quad (21)$$

to obtain

$$\begin{aligned} \mathbf{F}_{Jb} &= -\frac{e}{8\pi^3 c^2} \int \frac{d^3\mathbf{k}}{k^2} \langle e^{-i\mathbf{k} \cdot \mathbf{r}} \rangle \\ &\quad \times \int d^3\mathbf{r} e^{i\mathbf{k} \cdot \mathbf{r}} \int d^3\mathbf{r}' \\ &\quad \nabla \cdot \left\{ \nabla \cdot \left[\frac{\partial_t \mathbf{J}(\mathbf{r}', t)}{R} \right] \right\}, \end{aligned} \quad (22)$$

where ∂_t denotes the differentiation by time. The i th-component of the function integrated by \mathbf{r}' in the above equation can be divided into three parts as follows.

$$\begin{aligned} & \nabla_i \left\{ \nabla \cdot \left[\frac{\partial_t \mathbf{J}(\mathbf{r}', t)}{R} \right] \right\} \\ &= \frac{3(x_i - x'_i)^2}{R^5} \partial_t J_i(\mathbf{r}', t) \\ & \quad - \frac{\partial_t J_i(\mathbf{r}', t)}{R^3} \\ & \quad + \sum_{(j \neq i)} \frac{3(x_i - x'_i)(x_j - x'_j)}{R^5} \partial_t J_j(\mathbf{r}', t). \end{aligned} \quad (23)$$

We can set

$$(x - x')^2 = (y - y')^2 = (z - z')^2 = \frac{R^2}{3} \quad (24)$$

in eq.(23), since the integration of eq.(22) does not depend on how to choose the direction of axis of the coordinates. The first term and the second term in eq.(23) then cancel each other. Only the last term remains. If we change the variable \mathbf{r} into $\tilde{\mathbf{r}}$ as $\mathbf{r} - \mathbf{r}' = \tilde{\mathbf{r}}$, the i th-component of \mathbf{F}_{Jb} can be rewritten as

$$\begin{aligned} (\mathbf{F}_{Jb})_i &= -\frac{3e^2}{8\pi^3 c^2} \int \frac{d^3 \mathbf{k}}{k^2} \langle e^{-i\mathbf{k} \cdot \mathbf{r}} \rangle \\ & \quad \times \int d^3 \tilde{\mathbf{r}} e^{i\mathbf{k} \cdot \tilde{\mathbf{r}}} \sum_{j \neq i} \frac{\tilde{x}_i \tilde{x}_j}{|\tilde{\mathbf{r}}|^5} \\ & \quad \times \frac{d}{dt} \langle \exp(i\mathbf{k} \cdot \mathbf{r}) v_j \rangle. \end{aligned} \quad (25)$$

Similarly, \mathbf{F}_{Ja} is obtained as follows,

$$\begin{aligned} \mathbf{F}_{Ja} &= -\frac{e}{c^2} \iint d^3 \mathbf{r} d^3 \mathbf{r}' \frac{|\psi(\mathbf{r}', t)|^2}{R} \frac{\partial \mathbf{J}(\mathbf{r}, t)}{\partial t} \\ &= -\frac{e^2}{2\pi^2 c^2} \int \frac{d^3 \mathbf{k}}{k^2} \langle e^{-i\mathbf{k} \cdot \mathbf{r}} \rangle \\ & \quad \times \frac{d}{dt} \langle e^{i\mathbf{k} \cdot \mathbf{r}} \mathbf{v} \rangle. \end{aligned} \quad (26)$$

In NCT, the charge of an electron is not located at a point, but is extended to a volume determined by a charge density of eq.(7). The dimensions of the volume is not smaller than the Compton wavelength for Dirac electron⁶⁾. We can introduce a cut off k_{max} , and assume that

$$0 < k < k_{max} = \frac{m_0 c}{\hbar}, \quad (27)$$

where $\hbar k$ is the momentum of the photon which act on the extended charge of the electron. Under this assumption, we can reasonably use the

dipole approximation⁷⁾: $\exp(\pm i\mathbf{k}\mathbf{r}) \cong 1$. The dipole approximation leads \mathbf{F}_{Jb} to

$$\begin{aligned} & (\mathbf{F}_{Jb})_i \\ &= -\frac{3e^2}{8\pi^3 c^2} \int \frac{d^3 \mathbf{k}}{k^2} \int d^3 \tilde{\mathbf{r}} \sum_{j \neq i} \frac{\tilde{x}_i \tilde{x}_j}{|\tilde{\mathbf{r}}|^5} \frac{d \langle v_j \rangle}{dt} \\ & \cong 0 \end{aligned} \quad (28)$$

since the integration is antisymmetric with respect to \tilde{x}_i . From eq.(26), \mathbf{F}_{Ja} becomes

$$\mathbf{F}_{Ja} = -\delta m \frac{d \langle \mathbf{v} \rangle}{dt} \quad (29)$$

with

$$\delta m = \frac{e^2}{2\pi^2 c^2} \int_0^{k_{max}} dk \iint \sin \theta d\theta d\varphi = \frac{2}{\pi} \alpha m_0, \quad (30)$$

where $\alpha = e^2/\hbar c$ is the fine-structure constant. We finally obtain

$$m \frac{d \langle \mathbf{v} \rangle}{dt} = \langle \mathbf{F}_{ext} \rangle + \frac{2e^2}{3c^3} \frac{d^2 \langle \mathbf{v} \rangle}{dt^2}, \quad (31)$$

where $m = m_0 + \delta m$ is renormalized mass. Equation (31) completely agrees to nonrelativistic L-D equation called Abraham-Lorentz equation.

3. CONCLUSION

A weakened Coulomb potential was suggested to overcome the Coulomb barrier between deuterons in palladium. The derivation of weakened Coulomb potential is based on the Abraham-Lorentz equation. We have derived the Abraham-Lorentz equation from the normal Hamiltonian with the resort to Crisp's method in neoclassical theory.

References

- 1) G. Morpurgo: Nuovo Cimento 9(1952)808; A. Loinger: *ibid.*, 2(1955)511; G. M. Prospero and A. Scotti: Nucl. Phys. 13(1959)140.
- 2) S. Sasabe: J. Phys. Soc. Jpn. 61(1992)812.
- 3) Private communication.
- 4) M. Ozaki and S. Sasabe: Phys. Rev. A80, (2009)024102.
- 5) M. D. Crisp: Phys. Rev. A42(1990)3703.
- 6) L. L. Foldy and S. A. Wouthuysen: Phys. Rev. 78(1950)29.
- 7) A. O. Barut *et al.*: Phys. Rev. A45(1992)7740; G. W. Ford *et al.*: Phys. Rev. Lett. 55(1985)2273.

Computer Simulation of States of Hydrogen in Metals of Face Centered Cubic Lattice

Hidemi Miura

1-27-6 Tsurugaoka, Izumi-ku, Sendai. 981-3109, Japan

In order to examine which kind of conditions cause two or more hydrogen in metals to gather, we simulated the motion of hydrogen using a classical molecular dynamics on a personal computer, furthermore we calculated the corresponding total energy with hydrogen using a quantum molecular dynamics on another one. We observed the tendency for movement of hydrogen atoms to be increased when temperature rose, but to be suppressed when the content of hydrogen atoms increased. It means that H atoms must interact with each other near O sites. We observed the total energy of state where hydrogen atom located on O site was lower than where hydrogen atom located on T site, and they were reversed by the deformation of lattice structures. It means that H atoms located on O sites would be able to transfer to T sites.

1. Introduction

Nuclear reactions such as nuclear fusion and nuclear transmutation have been reported in many experiments of deuterium (D) with condensed matter, especially palladium (Pd) metal.

Although many hydrogen or deuterium (H/D) atoms dissolve in some metals and alloys rather than Pd, they can do exceptionally in transition metals at the conditions such as normal temperature and normal pressure.

On the other hand, Pd has face-centered-cubic (FCC) lattice structure at the normal temperature and normal pressure. Then we considered that for nuclear fusion or nuclear transmutation to occur in the condensed matter, dissolution of D and the FCC lattice structure played an important role. Then we investigated the motion of D atoms and its state within FCC lattice metal.

Since nuclear reactions occur in the condensed matter such as FCC lattice metals, it is required for two or more D atoms to gather and condense in the narrow domain of the host metal¹⁻³. Then, in order to examine which kind of conditions cause nuclear reaction, we simulated the motion of H atoms substituting hydrogen for deuterium by a classical molecular dynamics method on a personal computer, and we calculated the total energy of corresponding states by a quantum (the first principles) molecular dynamics method on another one.

About the processes after D atoms gather, there are already some proposals in which D atoms will overcome Coulomb repulsion and condense, and then they will cause nuclear reactions^{4,5}.

2. Simulation of motion of H in FCC lattice metals by a classical molecular dynamics method

In order to investigate the whole motion of H in FCC lattice metals, we carried out the computer simulation based on a classical molecular dynamics method.

Nickel (Ni) was used as the object element because the Morse potential of Ni was comparatively well known for this simulation, and the periodic boundary condition was applied to the calculation cell (108 Ni atoms) of 3x3x3 units from restrictions of computational complexity and calculation time. The simulation was performed for bulk as the object form, changing temperature, the concentration of H atoms, etc. as follows.

Temperature: 0K, 100K, 200K, 300K, 400K, 500K

Concentration of H: 0%, 30%, 50%, 80%, 100%

Vacancy: exist, not exist

Impurity atom: (Li-atom) exist, not exist

Calculation time: 2ns (0.1ps/step×20,000,000step)

When the calculation cell of 2x2x2 units was used, computational complexity and calculation time became small, but the behavior of the simulation system became unstable under the influence of the periodic boundary condition when vacancy was put in the calculation cell and the molecular dynamics simulation was carried out. Then this calculation cell of 2x2x2 units was not used. The reason of setting 2ns as the calculation time was for stabilizing the simulation system over sufficient time.

In order to grasp the motion of H atoms inside the Ni lattice, Root Mean Square Distance (vibration is included) was investigated in some cases where a vacancy and/or an impurity atom (Li-atom) exist or not exist changing the temperature and the concentration of H atoms. As a result, the following things were understood.

- (a) The temperature becomes higher the movement of H atoms becomes larger.
- (b) The content of H atoms becomes larger the restraint of movement of H atoms becomes stronger.
- (c) Even if there is a vacancy or an impurity atom the movement of H does not change a lot.

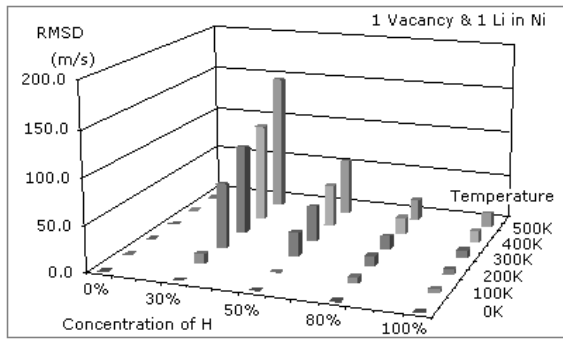


Fig. 1 Root Mean Square Distance of H in Ni

Figure 1 shows the Root Mean Square Distance (vibration is included) of H atoms as the movement of H atom in Ni metal in the case of existence of a vacancy and an impurity atom (Li-atom) changing the temperature and the concentration of H atoms. Restrain of the movement of H atoms is in agreement with the empirical rules in many metal-hydrogen systems, and it means that H atoms must interact with each other near O sites.

We will investigate where the interactions between H atoms cause when they move from O sites to T sites, how long they stop on T sites, and how strong the vacancy and impurity atom influence to their movement, etc.

3. Calculation of the total energies of FCC lattice metals by the quantum electronic state calculation

In order to investigate the state of H in FCC lattice metals in detail, we carried out the quantum (the first principle) electronic state calculation using plane waves for the basis function and using norm preservation type pseudopotentials. Ni, Pd, Pt etc. of FCC lattice metals were used as the object element and the periodic boundary condition was applied to the calculation cell (four atoms) of 1x1x1 units from restrictions of computational complexity and calculation time.

3.1 The total energy of the state where H is located on O site, T site, etc.

The quantum electronic state calculation was performed for bulk metal, locating H atom on (a) O site, (b) T site, (c) P point which is the center of the boundary plane of equilateral triangle between them and (d) L point which is the center of distance between two O sites.

Figure 2 shows the conventional calculation cell of Pd where H atom is located on O site.

Figure 3 shows (A) the total energies of the states with H atom on O site, T site, P point or L point in some FCC lattice metals, which indicate the difference from the standard energy of the state where H is not located, and it shows (B)

the total energy difference between the states with H on O site and T site, respectively.

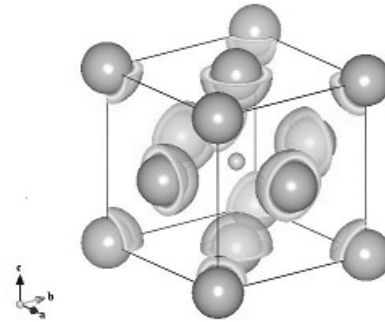


Fig. 2 Schematic of Calculation Cell of Pd with H on O site

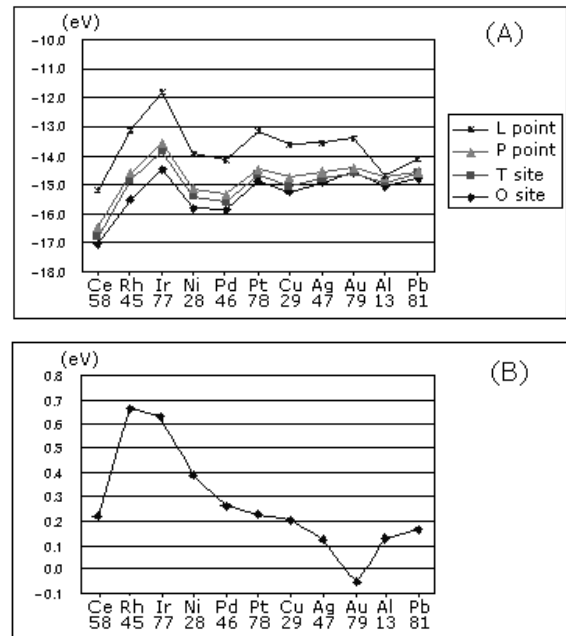


Fig. 3 Total Energy (A) of some FCC Lattice Metals and (B) Differences between O site and T site with H

About the almost all FCC lattice metals, the total energies are larger in the order of the states where H atom is located on L point, P point, T site and O site, respectively. But, in the case of Gold (Au), the total energy of state with H atom on O site is larger than that with H atom on T site.

The total energies of the states with H atom on O site, T site or P point of Ni and Pd are lower than those of the other FCC metals except Cerium (Ce). And the total energy differences between the states with H atom on O site and T site of Ni and Pd are in the middle of range of all FCC metals.

3.2 Change of the total energies by deformation of Lattice

The lattice constant of body-centered-cubic (BCC) lattice such as iron (Fe) are short, and the potential barriers between interstitial sites are low. Then, it is known that the tunnel transfer processes become main, when the energy level of sites adjoining each other become consistent by the lattice deformation of host metal due to thermal vibration.

On the other hand, the lattice constant of FCC lattice such as Pd are long, and the top of the potential barriers between interstitial sites are high. Then, the tunnel transfer processes are estimated to be the same order of the overcoming of the barrier between the sites adjoining each other, which occur when H atom receive the energy by thermal vibration of the lattice of metal.

Then, we wonder how the movements of H become large, if the lattice deformation which is larger than that of heat vibration, takes place in FCC lattice metals. In order to investigate above mechanism, the quantum electric state calculation was performed under the deformation of lattices. Here, the coordinates of four vertices of tetrahedron surrounding T site and the position of H atom located on O site, T site or P point were arranged into the reduced lattice coordinate: $\Delta a/a$, where the latter was divided eleven with 0.0025 separation.

- Atom 1: from (0.0000, 0.0000, 0.0000) to (-0.0250, -0.0250, -0.0250)
- Atom 2: from (0.5000, 0.5000, 0.0000) to (0.5250, 0.5250, -0.0250)
- Atom 3: from (0.5000, 0.0000, 0.5000) to (0.5250, -0.0250, 0.5250)
- Atom 4: from (0.0000, 0.5000, 0.0500) to (-0.0250, 0.5250, 0.5250)
- O site: from (0.5000, 0.5000, 0.5000) to (0.5250, 0.5250, 0.5250)
- T site: from (0.2500, 0.2500, 0.2500) to (0.2500, 0.2500, 0.2500) (not changed)
- P point: from (0.3333, 0.3333, 0.3333) to (0.3283, 0.3283, 0.3283)

Figure 4 shows the change of total energies corresponding to the deformation $\Delta a/a$ of lattice of Ni, Pd and Pt respectively, where H atom is located on O site, T site or P point.

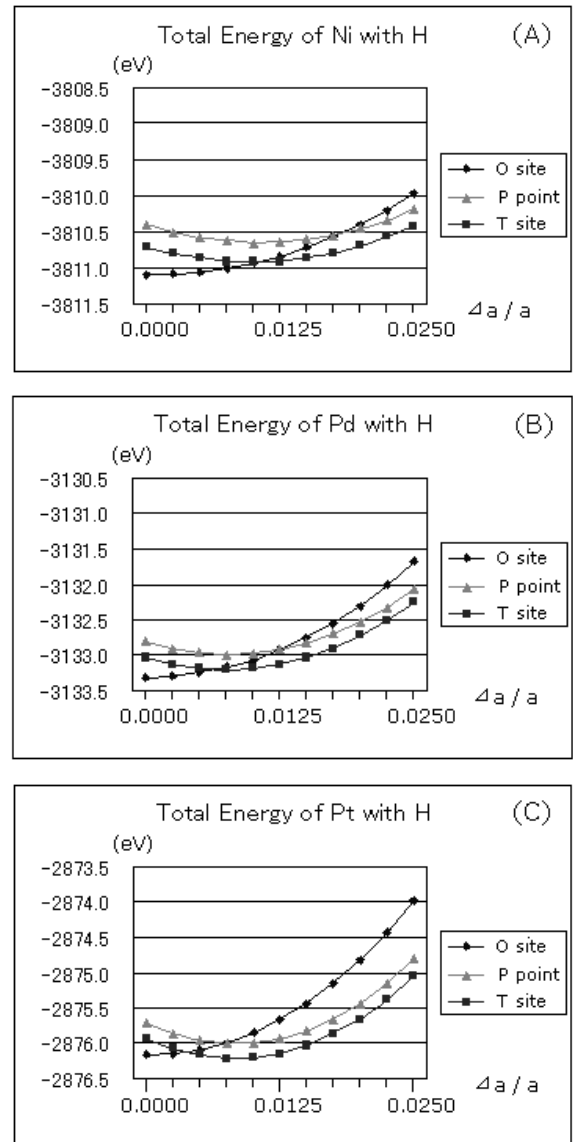


Fig. 4 Change of Total Energies Corresponding to Lattice deformation of (A) Ni, (B) Pd and (C) Pt

The calculation results about the change of total energies are as follows.

- (a) When there is no deformation of the lattice, the total energy of state with H atom on O site is lower than with H atom on T site.
- (b) The total energy of state with H atom on O site and with H atom on T site are reversed at the lattice deformation of about 1.0/100 lattice constant in the case of Ni, about 0.7/100 lattice constant in the case of Pd and about 0.3/100 lattice constant in the case of Pt, respectively.
- (c) The total energy of state with H atom on P point is almost always higher than with H atom on T site, and changes almost in parallel with it.

From the above calculations, the total energies of the states with these H atoms on O site or T site will be able to

become consistent, and then H atoms located on O sites will transfer to T site, when the vertices of tetrahedron move to outside with from 0.3/100 to 1.0/100 of the lattice constant.

However, when these deformations mentioned in above (b) occur, the energies of the states with H atoms on O sites should rise about from 0.1 to 0.2 eV as shown in Fig. 4, so that such deformations would not occur easily by only the thermal vibration because the thermal energy of normal temperature (300K) is times lower several than these energies.

Then, we will investigate the mechanism in which H atoms gather to the same place of T site when an impurity atom hops out from the site surrounded by the vertices of deformed tetrahedron in the calculation cell of 2x2x2 units (32 atoms; or more), for example.

4. Summary

By the classical molecular dynamics method with the bulk of Ni, we observed the tendency that the content of H atoms becomes larger the restraint of movement of H atoms becomes stronger.

By the quantum molecular dynamics method with the bulk of Ni, Pd and Pt (and others), we observed the total energy of states with H atoms on O site or T site were reversed by deformation of lattice structure, and then H atoms located on O sites would transfer to T sites.

We will simulate in larger calculation cell and investigate details more.

Acknowledgement

The authors would like to express their thanks to developers of the computer programs for using them as follows.

- (a) The classical molecular dynamics method and visualizing the results:

RYUDO and RYUKI: Ryuji Miura of Department of Engineering at Tohoku University

- (b) The first principles electronic state calculation using pseudopotentials and plane wave basis, and visualizing the results:

ABINIT: ABINIT group

VESTA: Koichi Monma and Fujio Izumi of National Institute for Materials Science

- (c) The first principles molecular orbital method and visualizing the results:

DV-X α : Hirohiko Adachi of Department of Engineering at Kyoto University and another

VESTA: Koichi Monma and Fujio Izumi of National Institute for Materials Science

References

- 1) H. Miura, Study on Formation of Tetrahedral or Octahedral Symmetric Condensation by Hopping of Alkali or Alkaline-earth Metal Ion, Proc. of 12th International Conference on Cold Fusion, p. 536 (2005).
- 2) H. Miura, Formation of Tetrahedral, Octahedral or Hexahedral Symmetric Condensation by Hopping of Alkali or Alkaline-earth Metal Ion, Proc. of 7th Meeting of Japan CF Research Society, p. 79 (2006).
- 3) H. Miura, Speculation on the Relation between Condensation of Hydrogen or Deuterium in Metal by Formation of Vacancy-Hydrogen Cluster or Vacancy-Deuterium Cluster, Proc. of 9th Meeting of Japan CF Research Society, p. 65 (2009).
- 4) A. Takahashi, Deuteron cluster fusion and related nuclear reaction in metal-deuterium/hydrogen systems, Recent Res. Devel. Phys. 6, 1-28 (2005).
- 5) A. Takahashi, Chronicle of Condensed Cluster Fusion Models, Proc. of 8th Meeting of Japan CF Research Society, p. 51 (2007).